AN EXPERIMENTAL AND ANALYTICAL INVESTIGATION OF HYPERSONIC INLET BOUNDARY LAYERS

J. F. Stroud
L. D. Miller

FOREWORD

This report was prepared by the Lockheed-California Company, Burbank, California, under USAF Contract No. AF 33(657)-8833. The contract was awarded to Lockheed 25 May 1962. It was initiated under Project No. 1366, "Aerodynamics and Flight Mechanics," Task No. 136605, "Induction System Research." The work was administered under the direction of the Air Force Flight Dynamics Laboratory, Research and Technology Division, Air Force Systems Command, Wright-Patterson Air Force Base, Ohio, Mr. R. L. Balent, Project Engineer.

The work covered by this report was conducted from June 1962 to November 1964. The manuscript was released by the authors in November 1964 for publication as an RTD Technical Report.

The work was accomplished under the direction of Mr. J. F. Stroud, Propulsion Department Manager of Lockheed. Mr. L. D. Miller also of the Propulsion Department was the Project Engineer.

The authors wish to express their appreciation to Mr. J. C. Sivells, Manager, and Mr. H. T. Wood, Assistant Manager, of the Hypersonic Branch, von Karman Facility, AEDC (ARO, Inc.) for their cooperation in the wind tunnel program. Additional acknowledgements are due to the AEDC project engineers for their efforts in conducting the wind tunnel tests. These include Mr. L. D. Kayser, Mr. R. Rhudy and Mr. F. K. Hube.

Appendix IV of this report is published as Volume II and is identified as AFFDL-TR-65-123 Vol II.

The Contractor's report number is LR 18803.

This technical report has been reviewed and is approved.

Alfred C. Draper

A. C. DRAPER
Assistant for Research and Technology
Flight Mechanics Division
Air Force Flight Dynamics Laboratory

ABSTRACT

Detailed boundary layer surveys have been made on four axisymmetric compression surface models simulating typical hypersonic inlet compression surfaces at free stream Mach numbers ranging from 4 to 8. The four models were designed to provide isentropic compression at design Mach numbers of 5, 6, 8 and 10. The Mach 8 design model had provisions for wall cooling. Quantitative heat transfer measurements were made on the Mach 8 model at free stream Mach numbers of 5, 6, and 8. The tests were conducted in the Arnold Engineering Development Center (AEDC) 50-inch diameter Mach 8 Tunnel B and 40-inch supersonic Tunnel A, both of the von Karman Facility. Typical free stream Reynolds numbers for these tests were 6.56×10^6 at Mach 4 and 3.8×10^6 at Mach 8, with the Reynolds numbers based on the maximum diameter of the Mach 8 model. The tests of the boundary layer models at various free stream Mach numbers and Reynolds numbers provided a large amount of turbulent boundary layer data on compression surfaces typical of hypersonic inlets.

Two existing turbulent boundary layer theories were modified to account for the various phenomena found to be of importance in hypersonic boundary layers. Theoretical results from these methods have been correlated with the experimental data.

A significant observation of the present program is the powerful favorable effect of centrifugal force phenomena on boundary layer development in continuous adverse pressure gradients. It was found that these effects become more pronounced with increasing Mach number and reductions in free stream Reynolds number.

TABLE OF CONTENTS

ILLUSTRATIONS

ILLUSTRATIONS (cont'd)

SYMBOLS

C_f	local skin friction
C_F	average skin friction
c_p	specific heat at constant pressure
h	static enthalpy
h_t	total enthalpy
H_e	form factor, δ_e^*/θ_e
H_w	form factor, δ_w^*/θ_w
H^*	total enthalpy parameter, $h_t - h_{t_w}$
k	thermal conductivity
M	Mach number
M_e	local Mach number
P	pressure
Pr	Prandtl number, $\mu C_p/k$
Pr_t	turbulent Prandtl number, $\epsilon C_p/k$
q	heat transfer rate
r_o	body radius in cylindrical polar coordinates
R	radius of curvature along x
St	Stanton number
T	absolute temperature
Re	Reynolds number, $\rho_e u_e x/\mu_e$; Re/, Reynolds number per foot
u	velocity component along x
u_1	inviscid velocity component along x
v	velocity component along y
x	distance along surface of body
y	distance normal to body surface
α	angle between local surface and body centerline

γ ratio of specific heats

δ boundary layer thickness

δ_e^* displacement thickness - $\int_0^{\delta} (1 - \frac{\rho u}{\rho_e u_e})\, dy$

δ_w^* displacement thickness - $\int_0^{\delta} (\frac{\rho_l u_l}{\rho_{l_w} u_{l_w}} - \frac{\rho u}{\rho_{l_w} u_{l_w}})\, dy$

ϵ turbulent viscosity

θ_e momentum thickness - $\int_0^{\delta} \frac{\rho u}{\rho_e u_e} (1 - \frac{u}{u_e})\, dy$

θ_w momentum thickness - $\int_0^{\delta} \frac{\rho u}{\rho_{l_w} u_{l_w}} (\frac{u_l}{u_{l_w}} - \frac{u}{u_{l_w}})\, dy$

μ viscosity

ν kinematic viscosity

ρ density

τ shear stress $\bar{\mu} \frac{du}{dy} - \overline{(\rho \nu)' u'}$

ϕ energy thickness - $\int_0^{\delta} (1 - \frac{H^*}{H_e^*}) \frac{\rho u}{\rho_e u_e}\, dy$

Subscripts

aw adiabatic wall

e conditions at the edge of boundary layer

∞ , o free stream

t stagnation conditions

w conditions based on wall values

l inviscid flow

Superscripts

'	Fluctuating quantity or quantity based on reference temperature

INTRODUCTION

The performance of hypersonic inlets is influenced substantially by the boundary layer that develops on the compression surfaces. This boundary layer represents a large portion of the inlet flow and can interact significantly with the inviscid flow field. Development of the boundary layer is very complex as a result of the inlet environment which includes strong adverse pressure gradients, heat transfer, centrifugal force phenomena, and real gas effects. Each of these factors affects performance to a varying degree depending upon flight Mach number and inlet configuration.

Knowledge of the boundary layer is necessary (1) to enable appropriate design compromises involving pressure recovery, drag, and weight to be made, and (2) to permit appropriate contour corrections to be incorporated for displacement effects in any given inlet design. Accordingly, the rational design of hypersonic airbreathing systems requires understanding of the physical phenomena as well as analytical methods for predicting the boundary layer in the environment of hypersonic inlets. The combined experimental and analytical program described herein was initiated with the objective of achieving this knowledge of the boundary layer insofar as practical within the limitations of time and resources available.

Previous research programs on supersonic and hypersonic inlet boundary layers are reported in References 1 and 2. Those efforts were concerned with boundary layer development on two dimensional circular arcs and isentropic compression surfaces at free stream Mach numbers of 3.0 and 6.0. The investigation described herein provides new boundary layer data for axially symmetric isentropic compression surfaces, with and without heat transfer, for the Mach number range of 4 to 8. The purpose of the present report is to describe the experimental and analytical efforts accomplished under Contract Number AF 33(657)-8833 having the goals discussed above.

EXPERIMENTAL PROGRAM

The experimental program accomplished under this effort included the testing of four (4) axisymmetric open nosed models which incorporated differ amounts of reverse Prandtl-Meyer turning at the aft end of the model. Three of these models were uncooled while one was cooled. The models were tested at Mach numbers of 4, 5, 6 and 8 at various Reynolds numbers. Different lengths of boundary layer generating cylinders were employed upstream of the reverse Prandtl-Meyer surfaces to obtain the effects of initial boundary layer thicknesses. In addition, various boundary layer trips were examined. Instrumentation was sufficient to determine surface pressures, surface temperatures, boundary layer static and pitot pressures and total temperature at any desired station along the model and heat transfer rate on the Mach 8 heat transfer model. All tests were conducted in either the AEDC Tunnel A or Tunnel B. The test of each of the models was accomplished in a straightforward manner. After tunnel installation, instrumentation checkouts were made. Tests were then conducted at various Mach numbers and Reynolds numbers using different boundary layer generating cylinder lengths and tripping devices in order to obtain a fully developed turbulent boundary layer at the start of the isentropic compression surfaces.

In addition to the wind tunnel tests, a bench test was conducted to establish the validity of the heat transfer measurement procedure on the Mach 8 cooled model. A discussion of this test is given in Appendix III.

The following paragraphs discuss in detail the models, instrumentation and wind tunnels employed in the experimental program.

Description of Models

Four primary wind tunnel models were designed and fabricated under this program. The models were designed such that each provided a different rate of compression and therefore a different adverse pressure gradient. This was most simply accomplished by the use of a different design Mach number focused isentropic compression surface on each model. Each model surface was designed for maximum compressive turning as limited by the shock structure at its design Mach number. Models were fabricated which incorporated focused compression surfaces at design Mach numbers of 5, 6, 8, and 10. The Mach 5, 6, and 10 models were uncooled whereas the Mach 8 model incorporated provisions for cooling.

The uncooled Mach 5, 6, and 10 models are shown schematically in Figure 1, and the heat transfer Mach 8 model is shown in Figure 2. The external coordinates for each of the four models are given in Figure 3. As noted the models contain conical flares on the aft end. These flares were designed to prevent the expansion at the end of the models from feeding upstream and influencing the boundary layer at the aft stations. The compression surfaces are preceded by boundary layer generating cylinders which include tripping devices for forcing transition. Hollow generating cylinders instead of pointed closed spikes were used to minimize the initial shock losses. Generating cylinder lengths of 9 and 17 inches were designed for the uncooled models and 12.36 and 24.73 inches for the heat transfer model. The generating cylinders were preceded by an inlet section which contains the boundary layer trips.

The inlets for the uncooled and cooled models, both with vortex generators, are shown in Figures 4 and 5, respectively. Both the generating cylinders and compression surfaces were designed to permit air to flow through the entire model without choking. All models were fabricated from stainless steel 17-4 PH.

In order to obtain heat transfer data and determine its effect on boundary layer characteristics for a typical compression surface, the Mach 8 design model had provisions for wall cooling as shown in Figure 2. A considerable effort was expended in the design of this model to insure that the internal cooling would be sufficient to achieve the desired isothermal wall temperature of 30° F. The two basic coolants initially studied were water and gaseous nitrogen. It was decided to employ a gaseous coolant, since the use of water would require a relatively complex heat exchanger in order to obtain the low wall temperature. Also, the water would require additives to prevent freezing and a closed circuit system. Gaseous nitrogen or air, on the other hand, did not require a return system since they could be exhausted into the tunnel. It was finally decided to utilize air as the gaseous coolant, rather than nitrogen, because it would be easier to control and was available at a much higher supply pressure (600 psi as compared with the nitrogen supply pressure of 75 psi using a pump). It was found that air could be cooled by means of a liquid nitrogen heat exchanger to temperatures comparable with the liquid nitrogen. A schematic of the system selected is shown in Figure 6. The cooling of the air was accomplished by passing pressurized air in coils through a tank of liquid nitrogen which cooled the air down to approximately the liquid nitrogen temperature of -290° F. The cooled air was then mixed with the high pressure supply air at higher temperatures and passed through the coolant passages of the model. Following the selection of a cooling medium, one problem which remained was to establish a means of achieving isothermal wall conditions. Due to the large difference in heat transfer between the forward and aft portions of the model, two independent cooling passages were utilized (Figure 2). This allowed the coolant mass flows and mixture temperatures to be varied independently in each channel, thus providing the flexibility required to maintain an isothermal wall under a variety of free stream conditions. The cooling passages were designed to obtain an outer model wall temperature of 490° R. in the AEDC tunnel B at Mach 8 and 800 psi stagnation pressure. This was accomplished by calculating the heat flux using van Driest's flat plate theory (Reference 3) and the local flow properties in the model's compression field. Then, using this heat flux, the model coolant passages were divided into small elements and the conservation equations for each element were solved simultaneously to obtain the thickness of the coolant passage.

The cooled model was designed to be larger than the uncooled models in order to provide space for the cooling passages and at the same time provide a wall thickness sufficiently large to obtain steady state heat transfer measurements. The outer wall of the cooled model was gold plated to minimize radiation from the model to the tunnel walls, since an adiabatic model wall temperature was desired and the theories did not include radiation heat transfer. The adiabatic wall temperature in Tunnel B was approximately 1200 ° R. and the cooled tunnel wall temperature was approximately 520° R. The uncooled models tested in Tunnel A were not gold plated since the Tunnel A wall was uncooled.

A photograph of the Mach 5 design compression surface with the 17-inch generating cylinder attached is shown installed in AEDC Tunnel A in Figure 7.

The boundary layer survey probes and mechanism box are also shown in this photograph. The mechanism enabled the boundary layers to be surveyed normal to the surface at various stations along the model. This was accomplished by the drive mechanism mounted in the probe mechanism box. This mechanism box, developed at AEDC, contains a drive mechanism with the capability of translating the probe 4.3 inches parallel to the probe arm. The probe arm can also be pitched downstream through an angle of 35 degrees. Two low speed d-c motors were used to drive the mechanism. Since the mechanism box contained motors, transducers, and potentiometers, it was protected from the tunnel temperature by a water jacket. Water lines and passages were also routed throughout the system to insure adequate cooling of the entire mechanism. The probe mechanism box was mounted on a shaft which provided 50 inches of longitudinal movement. In Tunnel B, this shaft traversed through the roll from the sector. In Tunnel A, the hydraulic unit was also downstream from the sector, but the shaft centerline was 8.25 inches above the tunnel centerline.

Instrumentation

Instrumentation was provided to measure surface temperature and pressure in addition to pitot pressure, static pressure, and total temperature at various distances normal to the surface in the boundary layer. The surface instrumentation is shown in Figures 8, 9, and 10 for the uncooled models and in Figure 11 for the heat transfer model. The surface instrumentation was more closely spaced near the aft of the models where large gradients exist. The surface static pressures were measured with orifices ranging from 0.030 to 0.040 inch in diameter. The surface thermocouples were chromel-alumel on all of the uncooled models.

A photograph of the boundary layer survey system is shown in Figure 12. Details of the survey system and probes are shown in Figures 13 and 14. The three probes, pitot, total temperature and static pressure, were mounted on a support attached to a mechanism which provided normal translation as well as angular rotation in the vertical plane (see Figure 7). This enabled measurements to be made at numerous points throughout the boundary layer with the probes essentially aligned with the model surface. The pitot tip height was 0.010 inch, including 0.001 inch lips. The static probe diameter was 0.030 inch with four 0.006 inch orifices, each located 45° from the top and bottom meridian planes. These orifices were located 10 diameters aft of the 20° total angle cone shoulder. The total temperature probe was 0.040 inch in diameter and was gold plated to minimize radiation losses. A calibration curve for the temperature probe, obtained in Tunnel A, is given in Figure 15 along with a schematic of the temperature probe tip.

The measurement of pitot pressure and total temperature in the boundary layer was relatively straightforward. It was recognized, however, that static pressure measurements in the boundary layer represented a potentially difficult problem due to the large stream angles, of up to 12 degrees, which were associated with the wall curvature of the models. Two approaches to this problem were therefore investigated prior to testing the models: (1) several static probe configurations were tested over a range of Mach numbers and stream angles in uniform flow to determine the effect of angle of attack and (2) a two pronged rake, having the static probes oriented at two different angles, with respect to the model wall, was constructed and tested on the Mach 10 model. Unpublished

results of the first of these approaches indicated that a static probe having the configuration shown in Figure 14 was relatively insensitive to angle of attack in a uniform flow. These results, however, were obtained at lower Mach numbers and higher Reynolds numbers than those of the present program. It was, accordingly, necessary to determine the characteristics of this probe at test conditions representative of the present investigation. The results of the tests of this probe under these conditions indicated that the static probe design of Figure 14 was relatively insensitive to stream angle for values of up to 10 degrees, as shown in Figure 16. The second approach described above was employed as a check by obtaining measurements with the two pronged static probe (Figure 17) set at two degrees and four degrees relative to the model wall. Resulting measurements are shown in Figure 18 for various streamwise stations along the Mach 10 model and are compared with the static probe, set at zero degrees relative to the wall, which is an integral part of the standard three pronged rake comprised of total pressure, total temperature, and static pressure probes. In addition, the static pressure measurements obtained with these probes are compared with derived static pressure at the edge of the boundary layer. Reasonable agreement between the various measured values and the derived values is indicated. The derived static pressures were obtained by utilizing the measured pitot pressure and the known local total pressure, outside the boundary layer, in conjunction with the Rayleigh pitot equation. In view of the general agreement between the static probe, set at three different angles, and the relatively insensitive characteristics of the basic probe with angle of attack (Figure 14), the static pressure probe set at zero degrees relative to the model wall and comprising part of the three pronged rake (Figure 13), was used throughout the majority of the tests.

Inasmuch as the measured static pressures agreed with the pitot derived static pressures at the edge of the boundary layer for the majority of the data and unexplained deviations existed in part of the data, a procedure for calculating static pressure profiles was devised and applied in reducing all data in order to provide consistent and accurate results. This procedure consisted of utilizing the known boundary conditions at the wall and edge of the boundary layer in conjunction with the measured static pressure gradients between the wall and the edge. The boundary condition at the wall, in terms of the value of the static pressure and the slope of the static pressure, is known from 1) the measured value of pressure at the wall (as determined from flush wall orifices) and 2) the slope of the static profile which is zero at the wall as determined from the normal component of the momentum equation. The boundary condition at the edge of the boundary layer is known from the static pressure derived from pitot measurements at the edge of the layer. The shape of the static pressure curve between the wall and the edge of the boundary layer is determined by the measured gradients of static pressure versus distance from the wall.

In addition to measuring surface temperatures and pressures on the heat transfer model, heat transfer measurements across the model wall were necessary. Three basic methods were explored; namely, 1) measurement of the temperature drop across the cooled wall, 2) a transient technique, and 3) measurement of the change in coolant temperature along the coolant passage. Measurement of the change in coolant temperature along the cooling passages was discarded due to the difficulty in measuring a bulk coolant temperature in a small passage. The transient technique was discarded because of the tendency of the model wall to depart from isothermal while the model was heating up. The method employed, therefore, was to measure the temperature

drop across the model wall. The heat transfer to the model wall was calculated from Fourier's law using the known wall conductivity and thickness. The temperature drop across the relatively thin model wall was obtained from a differential thermocouple developed to measure small temperature differencs, as constrasted to measuring absolute temperature on both sides of the wall and subtracting one from the other to obtain the difference. Heat transfer bench tests discussed in Appendix III proved this to be an accurate method of measuring heat transfer. A schematic of a typical differential thermocouple installed in the heat transfer model is shown in Figure 19. The differential thermocouples consist of constantan wires attached to the inner and outer sides of a stainless steel plug (same material as basic model wall). The constantan wires act as one leg of the thermocouple and the stainless steel plug acts as the other leg. In addition, absolute temperatures on each side of the plug were measured by copper-constantan and stainless steel-constantan thermocouples. Stainless steel-constantan thermocouples were used after several of the small copper wires were broken. The plugs were used to provide accessibility both during initial model fabrication and in the event replacement was required due to damage.

An electrical circuit between the model and pitot probe was hooked up with a light to establish when the pitot probe touched the model surface. Based on the repeatability of the potentiometer reading when the pitot probe touched the model surface, the maximum error in the probe positions normal to the model surface was estimated to equal $\pm$ 0.002 inch. The static pressure and total temperature probes were set in a horizontal plane with the pitot probe to within $\pm$ .005 inch with the aid of a telescopic microscope. The models were marked at the various survey stations by ink or fine scribe marks. The probe was set at these streamwise stations within $\pm$ .020 inch.

The pressure readings were estimated to be known to within $\pm$ 2 percent except for the low static pressures near the free stream static pressures. At the low pressures the accuracy is approximately $\pm$ 10 percent. The absolute wall temperatures were estimated to be known to + 5 degrees F, and differential temperatures to $\pm$ 0.2 degrees F.

Wind Tunnels

Tests were conducted in the AEDC 50-inch diameter Mach 8 Tunnel B and the 40-inch supersonic Tunnel A, both of the von Karman Facility. The Tunnel B is a continuous flow type with an axisymmetric nozzle designed for Mach 8. The nozzle is water cooled to maintain a tunnel wall temperature of approximately 60 degrees F. The test section is 50 inches in diameter. This tunnel has reservoir stagnation pressures from 60 to 800 psia available and operates at a reservoir stagnation temperature of approximately 1350 degrees R.

Tunnel A is also a continuous flow type with a two-dimensional variable nozzle. The test section is 40 x 40 inches square, and Mach numbers of 4, 5, and 6 were tested corresponding to total temperatures of approximately 580 degrees R, 640 degrees R, and 720 degrees R, respectively.

These facilities are described in more detail in Reference 4.

The axisymmetric models were mounted in a uniform Mach number field to approximately $\pm$ 0.3 percent in both Tunnels A and B. A complete summary of the conditions tested in both tunnels is given in Table I.

EXPERIMENTAL DATA

The following paragraphs discuss various representative experimental data obtained in the wind tunnel test program. A complete tabulation of all experimental data obtained is given in Volume II.

Transition Tests

Because of the natural tendency of hypersonic boundary layers to remain laminar, tripping devices were required to force transition on the boundary layer generating cylinder forward of the model compression surface. Several boundary layer tripping devices were tested on the 17-inch boundary layer generating cylinder at Mach 8 in Tunnel B. These devices included wires protruding normal to the surface, air injection normal to the surface through perforations, and vortex generators. Figure 20 shows these devices. The air injection normal to the surface was found to change the model temperature considerably and was therefore discarded. Representative velocity profiles taken at the downstream end of the 17-inch generating cylinder with the wire trips and vortex generators located on the upstream end are shown in Figure 20. It is noted that the vortex generators result in a thinner boundary layer and a higher energy velocity profile than the conventional wire trips. This is a logical result in light of the fact that the vortex generators provide vortices similar to those observed in natural transition. Vortex generators of the type shown in Figure 20 were used throughout the program because of the favorable results obtained.

Uncooled Models

This section describes respresentative data obtained on the Mach 5, 6, and 10 uncooled models in the AEDC Tunnel A at free stream Mach numbers of 4, 5, and 6. Representative local Mach number and wall static pressure distributions in the streamwise direction are shown in Figure 21 for the Mach 5 model. The local Mach number M_e is defined as the Mach number at $y = \delta$. The Mach number decreases significantly toward the downstream end of the model due to the supersonic compressive turning which results in the large adverse pressure gradients shown. The monotonic nature of the static pressure curves indicates that boundary layer separation did not occur.

Typical velocity and static pressure profiles in the boundary layer are shown in Figure 22 for several streamwise stations along the Mach 5 model at a free stream Mach number of 5. Whereas strong adverse pressure gradients generally result in distorted low energy velocity profiles, it is seen from Figure 22 that the velocity profiles become less distorted as the flow enters these gradients. This is believed to be a result of powerful centrifugal restoring forces which are a manifestation of the substantial wall curvature in the streamwise direction. These centrifugal force effects are clearly evident in the static pressure profiles (Figure 22). The effects become more pronounced as the wall curvature increases near the aft of the model compression surface.

It is conventional to define the boundary layer thickness as the distance normal to the wall where the velocity is 99 percent of the local velocity u_e. Although this definition is adequate in uniform flow fields, it can not be applied to non-uniform flow fields where the velocity outside the boundary layer is varying with distance normal to the wall. Also, the high energy boundary layers associated with the present test make the calculation of boundary layer thickness using the velocity profile difficult. It was therefore necessary to define a boundary layer thickness that was consistent both in the uniform flow fields and in the non-uniform flow fields and yet yield reasonable accuracy. Since the compression surfaces are isentropic, the total pressure outside the boundary layer is uniform, whereas, in the boundary layer the total pressure varies significantly. It was thus decided to define the boundary layer thickness δ as the distance normal to the wall where the total pressure is 95 percent of the local total pressure outside the boundary layer. This definition corresponds approximately to the conventional definition above for a 1/7 power law velocity profile.

Representative distributions of boundary layer thickness, δ, displacement thickness, δ^*_w, and form factor, H_w, along the Mach 5, 6, and 10 design models are shown in Figures 23, 24, and 25, respectively. The definitions of δ^*_w and H_w differ from the more conventional definitions of δ^* and H in that they are referenced to a computed inviscid wall value of ρu rather than a value computed at the edge. A discussion of this definition is given in the section on boundary layer theory. Two Reynolds numbers for each Mach number were tested in most cases. (See Table I for a complete listing of the conditions tested.) The free stream Mach number of 4 resulted in the largest Reynolds number variations (a factor of about 7.5). For this reason, both Reynolds numbers are shown in Figures 23 and 25 for the Mach 4 data. From these results it is seen that, in general, Reynolds number does not have a powerful effect on the boundary layer characteristics. The form factor and displacement thickness decrease significantly as the boundary layer proceeds downstream in the adverse pressure gradients of the compression surface. This is due to a decrease in local Mach number with distance along compression surface and higher energy profiles associated with centrifugal force effects. Although the boundary layer thins out significantly near the aft of the model, the boundary layer thickness would still represent a large percentage of the throat height in an inlet and therefore must be considered in inlet design.

The effects of free stream Mach number on the boundary layer characteristics in continuous adverse pressure gradients are illustrated for the Mach 5 model at free stream Mach numbers of 4 and 6 in Figure 26 at comparable Reynolds numbers. The Reynolds numbers, based on the generating cylinder length at free stream Mach numbers of 4 and 6 are 9.03×10^6 and 7.36×10^6, respectively. The form factor and displacement thickness at the beginning of the compression surface are much higher for the Mach 6 case relative to Mach 4. Also, the rate of compression is considerably more rapid for the Mach 6 condition as indicated by the local Mach number distribution comparison in the upper part of Figure 26. It might logically be expected that this higher rate of compression in the Mach 6 case would lead to more boundary layer distortion, i.e., higher value of form factor at the end of the compression surface. Analysis of the data, however, indicates that the anticipated increased distortion due to the higher rate of compression at Mach 6 is offset by the stronger centrifugal force effects at the higher Mach number This results in the final values of shape parameter and displacement thickness being almost identical at the downstream end of the surface for free stream Mach numbers of 4 and 6. The stronger pressure gradients normal to the wall for

the Mach 6 case, relative to the Mach 4 case, as shown in Figure 26, confirm, in conjunction with the boundary layer equations, that centrifugal force effects are responsible for the result described above. The higher the static pressure gradient normal to the wall, the stronger the favorable centrifugal force effect.

The effects of Reynolds number at the beginning of the compression surface on the boundary layer characteristics are shown in Figure 27 for the Mach 5 model at a free stream Mach number of 4. The initial Reynolds number, based on the boundary layer generating cylinder length, is 0.64 million in one case and 9.03 million in the other. The form factor and displacement thickness are higher for the low Reynolds number case in the zero pressure gradient just ahead of the compression surface as would be expected from flat plate data. However, as the flow proceeds along the compression surface, the form factor begins decreasing at a more rapid rate for the low Reynolds number case. At the aft of the model, the form factor is smaller for the low Reynolds number in relation to the high Reynolds number case. This result is again attributable to the more powerful favorable centrifugal force effects in the low Reynolds number case. This is shown in Figure 27, where the pressure gradients normal to the wall are substantially stronger for the low Reynolds number condition.

It is clear from the above observations that centrifugal force effects play an extremely important role in the development of boundary layers on compression surfaces having substantial wall curvature in the streamwise direction. These effects are favorable and become stronger with increasing Mach number and reductions in Reynolds number over the range of variables investigated.

The Mach 10 model was tested in the AEDC Tunnel B at the conditions shown in Table I. The experimental data obtained are given in tabular form in Volume II. This stainless steel model contained a polished finish prior to testing in the tunnel but after several hours of testing, the surface turned a light brown, thereby changing the radiation heat transfer. A discussion of this effect follows.

As a result of the AEDC Tunnel B wall being cooled to approximately 520 degrees Rankine, radiation heat transfer between the uncooled model outer wall and tunnel wall occurred. Since there is no radiation heat transfer from the model inner wall, it is at a higher temperature than the outer wall. The model inner wall refers to the inside of the generating cylinder and compression surface, and the model outer wall refers to the outside of the generating cylinder and compression surface, see Figure 1. Consequently, conductive heat transfer occurs from the inner to the outer wall of the model. This conductive heat flux results in a net cooling of the inner model wall boundary layer and a net heating of the outer model boundary layer. This radiation heat transfer may be estimated on the generating cylinder. The heat flux is written

$$q_r = \frac{\sigma(T_{MW}^4 - T_{TW}^4)}{\frac{1}{\epsilon_{MW}} + \frac{A_{MW}}{A_{TW}}\left(\frac{1}{\epsilon_{TW}} - 1\right)}$$

where the following are assumed:

q_r Radiation heat flux

T_{MW}	Model wall temperature 1150° R.
T_{TW}	Tunnel wall temperature 520° R.
A_{MW}/A_{TW}	Ratio of generation cylinder wall area to tunnel wall area 1/625
ϵ_{MW}	Emissivity of model wall .6
ϵ_{TW}	Emissivity of tunnel wall .8
σ	Stefan - Boltzmann constant .1713 x 10^{-8} Btu/($Ft^2 hr °R^4$)

Then, substituting these values in the above equation , gives:

$$q_r = 1722 \frac{Btu}{hr\ FT^2}$$

Thus, heat flux of approximately 1722 Btu/hr ft^2 radiates from the generating cylinder to the tunnel wall. Although this heat flux is not very large, it is felt that it is sufficient to cause the boundary layer data on the generating cylinder and Mach 10 model to deviate from adiabatic conditions. Unfortunately, this phenomenon was discovered only after the uncooled Mach 10 model was tested in Tunnel B.

Heat Transfer Mach 8 Model

The heat transfer Mach 8 model was tested at free stream Mach numbers of 5 and 6 in Tunnel A, and at Mach 8 in Tunnel B. The Mach 8 compression surface was preceded by a 24.73-inch generating cylinder with both front and rear vortex generator trips in Tunnel B and the compression surface was preceded by a 12.36-inch generating cylinder with front vortex generator trips in Tunnel A. A photograph of the heat transfer model installed in Tunnel B is shown in Figure 28.

Representative Mach number and wall static pressure distributions in the streamwise direction are shown in Figure 29 for free stream Mach numbers of 5, 6, and 8. Again, the strong adverse pressure gradients near the aft of the model are evident. The outer model wall temperatures and corresponding heat fluxes for the various cooling rates at a free stream Mach number of 8 and stagnation pressure of 800 psi are shown in Figure 30. The hot wall condition corresponds to zero cooling flow to the model. These data were obtained using the differential thermocouples. The temperature drop across the model wall, measured by the differential thermocouples, is compared with the temperature drop calculated from the absolute thermocouples in Volume II. Note the heat flux increases very rapidly near the aft of the model due to the large pressures and low Mach numbers. The heat flux for the hot wall (or zero coolant flow to the model) is also shown in Figure 30. It is noted that approximately adiabatic conditions were obtained on the model. This result was achieved by gold plating the model surface in order to minimize radiation heat transfer between the relatively hot model wall and cooled tunnel wall.

Typical velocity profiles for various streamwise stations along the Mach 8 model at a free stream Mach number of 8 are shown in Figure 31 for the 490 degrees Rankine wall temperatures. Total temperature profiles at various streamwise stations along this model at Mach 8 are also given in Figure 31. Note the total temperature within portions of the boundary layer are still larger than free stream total temperature, even with wall cooling.

The model wall temperatures for various cooling rates at free stream Mach numbers of 5 and 6 are shown in Figure 32 and the corresponding heat flux distributions are shown in Figure 33. Again, approximately adiabatic conditions were obtained on the model. Representative velocity and total temperature profiles along the Mach 8 model at free stream Mach numbers of 5 and 6 are given in Figures 34 and 35.

The distribution of Stanton number, St, along the heat transfer Mach 8 model, at free stream Mach numbers of 5, 6, and 8, is given in Figure 36.

The above profiles have been integrated to obtain the boundary layer integral parameters. Representative boundary layer thickness, δ, displacement thickness, δ^*_w, and form factors, H_w, along the cooled heat transfer model at free stream Mach numbers of 5, 6, and 8 are given in Figures 37, 38 and 39, respectively. Again, the form factor and displacement thickness decrease significantly toward the aft of the model in the high adverse pressure gradient field. As would be expected from theory, the thicknesses and the form factor generally improve with increased wall cooling.

A useful parameter to measure the amount of heat transfer to the wall is the parameter $(T_{aw}-T_w)/T_e$. This parameter has been computed for the heat transfer tests, and the results at the high tunnel stagnation pressures are shown in Figure 40. The reference Reynolds number based on the momentum thickness Re'_θ has also been computed for the heat transfer tests, and the results are shown in Figure 41. The momentum thickness used in this Reynolds number is the conventional momentum thickness θ_e. It is noted that the local Reynolds number increases very rapidly near the aft of the model in the strong pressure gradients. This is due to the high pressures and low Mach numbers in this region.

BOUNDARY LAYER THEORIES

Integral Parameters

Prior to discussing the theories examined under this program for comparison with the data, a discussion is given of the definitions of δ^*_w and H_w, as presented in the section on experimental data.

Historically, the boundary layer integral parameters have been defined as:

Displacement Thickness:

$$\delta^*_e = \int_0^\delta \left(1 - \frac{\rho u}{\rho_e u_e}\right) dy \qquad (1)$$

Momentum Thickness

$$\theta_e = \int_0^\delta \left(1 - \frac{u}{u_e}\right) \frac{\rho u}{\rho_e u_e} dy \quad \text{and} \qquad (2)$$

Form Factor:

$$H_e = \delta^*_e/\theta_e \qquad (3)$$

where e refers to the conditions at the edge of the boundary layer.

The thickness parameters defined in this manner are a measure of the mass and momentum deficit in the boundary layer when the conditions outside the boundary layer are uniform. However, in this test the conditions outside the boundary layer contain large gradients and therefore do not provide a convenient set of reference conditions. It is therefore appropriate to redefine these integral parameters in terms of mass deficits based upon the difference between the theoretical inviscid flow, which can be calculated, and the actual flow in the region occupied by the boundary layer.

Or

$$\rho_e u_e \delta^* = \int_0^\delta \rho_1 u_1 dy - \int_0^\delta \rho u dy \qquad (4)$$

where subscript 1 refers to the local inviscid conditions.

Equation (4) may be written

$$\delta^* = \int_0^\delta \left(1 - \frac{\rho u}{\rho_e u_e}\right) dy - \int_0^\delta \left(1 - \frac{\rho_1 u_1}{\rho_e u_e}\right) dy$$

$$= \delta^*_e - \delta^*_1 \qquad (5)$$

where

$$\delta^*_1 = \int_0^\delta \left(1 - \frac{\rho_1 u_1}{\rho_e u_e}\right) dy$$

Similarly, the momentum deficit due to the boundary layer can be defined in terms of the difference between the inviscid and actual momentum of the mass flow in the boundary layer.

$$\rho_e u_e^2 \theta = \int_0^\delta \rho u u_1 \, dy - \int_0^\delta \rho u u \, dy \qquad (6)$$

Rewriting equation (6)

$$\theta = \int_0^\delta \frac{\rho u}{\rho_e u_e} \left(1 - \frac{u}{u_e}\right) dy - \int_0^\delta \frac{\rho u}{\rho_e u_e} \left(1 - \frac{u_1}{u_e}\right) dy$$

$$= \theta_e - \theta_1 \qquad (7)$$

where

$$\theta_1 = \int_0^\delta \frac{\rho u}{\rho_e u_e} \left(1 - \frac{u_1}{u_e}\right) dy$$

The energy deficit due to the boundary layer can be defined as

$$\rho_e u_e \Phi {h_t}_e = \int_0^\delta \rho u {h_t}_1 \, dy - \int_0^\delta \rho u h_t \, dy \quad \text{or} \quad (8)$$

$$\Phi = \int_0^\delta \frac{\rho u}{\rho_e u_e} \left(\frac{{h_t}_1}{{h_t}_e} - \frac{h_t}{{h_t}_e}\right) dy$$

In the foregoing analysis, the conventional thickness parameters δ^*_e and θ_e and general integral parameters δ^* and θ were all defined in terms of reference conditions at the edge of the boundary layer. As a result of using these reference conditions, simple relationships were found between the general parameters δ^* and θ and the conventional parameters δ^*_e and θ_e as seen in Equations (5) and (7). However, the reference conditions may more appropriately be taken as the inviscid properties at the wall since these conditions are more accurately known, see Reference 2. This results in new integral parameters δ^*_w and θ_w which are obtained by replacing the reference mass flow $\rho_e u_e$ and momentum $\rho_e u_e^2$ in equations (5) and (6) by $(\rho_1 u_1)_w$ and $(\rho_1 u_1^2)_w$ respectively. This results in the following relations.

$$\delta^*_w = \frac{\rho_e u_e}{(\rho_1 u_1)_w} \delta^* \qquad \text{and} \qquad (9)$$

$$\theta_w = \frac{\rho_e u_e^2}{(\rho_1 u_1^2)_w} \theta$$

A new form factor may be defined

$$H_w = \delta^*_w / \theta_w \qquad (10)$$

In the present program the inviscid values have been determined from the total pressure just outside the boundary layer and the measured static pressure through the boundary layer. The values of ρ_{1w} and u_{1w} are the corresponding values of ρ_1 and u_1 obtained at the wall.

For the axisymmetric boundary layers with a boundary layer thickness of the order of the body radius the term dy in these integrals may be replaced by the term

$$(1 + y/r_o \cos \alpha)\ dy,$$

see Reference 5, where r_o = local surface radius

α = angle between local surface and model centerline.

This has been done for all of the integral parameters shown in the previous section.

General Discussion

Many researchers have developed theories for turbulent boundary layers with streamwise pressure gradients. Important contributions have been made by von Doenhoff, Tetervin, Schubauer, Rubert, Sandborn, Clauser, Truckenbrodt, and Rotta, (see References 6 through 13) for incompressible flow and Coles and Englert, Reshotko, Cohen, and Crocco, (see References 14 through 18) for compressible flow. The majority of these theories employ the von Karman momentum equation and an auxiliary equation involving a boundary layer profile parameter to complete the solution. The auxiliary equation has been completely empirical in some cases and semi-empirical in others. Most of the compressible theories cited above extend the incompressible solutions to compressible flows through the Stewartson transformation (Reference 19.) In addition to the above, a lag length procedure has been suggested by McLafferty (Reference 20) where a distance is required before substantial mixing of the high energy external flow with the low energy boundary layer flow occurs, following initiation of an adverse pressure gradient.

Without question turbulent stresses play an important role in compressible turbulent boundary layers. These stresses are extremely complicated due to density, viscosity, and temperature fluctuations. It is dubious whether a transformation, like the Stewartson transformation, can accurately transform the turbulent stresses from the compressible boundary layer (see

Reference 18.) It is therefore desirable to avoid using such a transformation, if possible. Two such approaches follow. These theories are termed the (1) Discontinuity/Analogy and (2) Classical Methods. The Discontinuity/Analogy method, described in Reference 21, has been extended to account for heat transfer to the wall and centrifugal force effects. The method is described below.

Discontinuity/Analogy Method

The net distortion of the boundary layer in a continuous adverse pressure gradient is envisioned as resulting from a combination of two simultaneous component actions at any streamwise station in the flow; one tending to distort the boundary layer and the other tending to restore it to a more uniform velocity profile. These two component actions are referred to as the distortion component and the restoring component, respectively. The method is illustrated qualitatively in Figure 42. In a continuous supersonic compression, the Mach number distribution is approximated by a series of steps, Figure 42. The discontinuities in Mach number give rise to discontinuities in form factor representing the distortion component. The constant Mach number elements between the discontinuities give rise to a relaxation in form factor representing the restoring component.

The mass entering the element shown in Figure 42 is equal to the mass leaving,

$$m_{BL_1} = m_{BL_2} \tag{1}$$

The average pressure, acting on the outer edge of the boundary layer, as shown in Figure 42, is

$$P_{e_m} = \frac{P_{e_1} + P_{e_2}}{2} \tag{2}$$

The mass flow may be related to the displacement thickness by

$$m_{BL} = \rho_e u_e (\delta - \delta^*) \tag{3}$$

Using equation (1), the boundary layer thickness ratio becomes

$$\delta_2/\delta_1 = \frac{(\rho_e u_e)_1}{(\rho_e u_e)_2} \left[\frac{1 - (\delta^*/\delta)_1}{1 - (\delta^*/\delta)_2} \right] \tag{4}$$

and from the conservation of momentum across the discontinuity

$$\bar{P}_1 - \frac{P_{e_1}+P_{e_2}}{2}\,(1-\delta_2/\delta_1) - \bar{P}_2\,\delta_2/\delta_1 = \frac{1}{\delta_1}\int_0^{\delta_2}\left[\rho u^2 dy\right]_2 - \frac{1}{\delta_1}\int_0^{\delta_1}\left[\rho u^2 dy\right]_1 \quad (5)$$

Noting

$$\int_0^{\delta}\rho u^2 dy = \rho_e u_e^2\left[\delta - \delta^* - \theta\right] \quad (6)$$

equation (5) may be written

$$\frac{\delta^*_2}{\theta_2} = \frac{-\frac{\delta^*_2}{\delta_1}\,\frac{(\rho_e u_e^2)_2}{P_{e_1}}}{\left[\frac{(\rho_e u_e^2)_1}{P_{e_1}}\left(1-\frac{\delta^*_1}{\delta_1}-\frac{\theta_1}{\delta_1}\right) - \frac{(\rho_e u_e^2)_2}{P_{e_1}}\left(\frac{\delta_2}{\delta_1}-\frac{\delta^*_2}{\delta_1}\right) + \frac{\bar{P}_1}{P_{e_1}} - \left(\frac{P_{e_1}+P_{e_2}}{2P_{e_1}}\right)\left(1-\frac{\delta_2}{\delta_1}\right) - \left[\frac{\bar{P}_2}{P_{e_1}}\right]\left[\frac{\delta_2}{\delta_1}\right]\right]} \quad (7)$$

where $\bar{P} = \frac{1}{\delta}\int_0^{\delta} P\,dy$

It is to be noted that the derivation thus far is very general in that no restrictions on Mach number, temperature or velocity profiles, or type of compression (isentropic or shock) have been made. Furthermore, pressure gradients normal to the wall, both upstream and downstream of the discontinuity, are approximately accounted for in the analysis by virtue of application of average static pressures through the boundary layer. Equations (4) and (7) may therefore be used for the case of hypersonic boundary layers with heat transfer to the wall. Also, it is believed that the above theory can be applied to the shock-boundary layer interaction problem; however, this is not treated here.

Assuming a power law velocity profile, a modified Crocco temperature distribution, and the equation of state, equations (4) and (7) may be solved by iteration for the properties at the end of the discontinuity. The restoring component is then computed using the boundary layer properties at the beginning of the element. An effective Reynolds number R_e' is found from the correlation equation of Sivells and Payne, Reference 22,

$$2m_i + 1 = \frac{1}{1 - 1.47\left[\dfrac{\log R'_{e_i} - 2.3686}{(\log R'_{e_i} - 1.5)^3}\right]^{1/2}} \qquad (8)$$

The effective distance x_{eff_i} is found from the relation

$$x_{eff_i} = \left[\frac{R'_e \, \nu'/\nu_e}{R'_{e/}}\right]_i , \quad R'_{e/} = u_e/\nu_e \qquad (9)$$

and the effective distance at the end of the component is

$$x_{eff_{i+1}} = x_{eff_i} + \Delta x_{i-i+1} \qquad (10)$$

where x_{i-i+1} is the physical length of the restoring element. The final Reynolds number of the element is found

$$R'_{eff_{i+1}} = (R'_{e/})_i \, (\nu_e/\nu')\, x_{eff\ i+1} \qquad (11)$$

The power law exponent at the end of the component m_{i+1} is found from equation (8) using $R'_{eff_{i+1}}$. Then the integral parameters may be found, again assuming a modified Crocco temperature distribution, and the procedure is repeated. From a study of the experimental data obtained in this program, it is concluded that the longitudinal radius of curvature is at least an order of magnitude greater than the boundary layer thickness. However, it is easily seen from the experimental data (Figure 22) that the pressure gradients normal to the wall are significant and must be included in a complete theoretical analysis. When pressure gradients normal to the wall are included in the above method, the boundary layer thicknesses along the body must be known. For the correlations of the theory with experimental data given in the present report the experimental boundary layer thicknesses were used. However, an iterative procedure is outlined in Appendix I where the boundary layer thicknesses along the body are not required.

Since pressure gradients normal to the wall are not ordinarily available, an approximate method for estimating these static pressure profiles using a characteristics solution is given in Appendix II.

Classical Method

A classical method which treats a turbulent compressible boundary layer with pressure gradient and heat transfer, and enables heat transfer, skin friction, boundary layer thickness, displacement thickness, and momentum thickness to be computed given the proper initial and boundary conditions, is discussed in the following paragraphs. It is convenient to treat a turbulent boundary layer by the integral method, since under certain assumptions the turbulent shear stresses may be eliminated. The procedure permits the conventional boundary layer equations of motion across the boundary layer to be integrated obtaining the integral differential equations (Reference 23.) These integral equations are solved numerically along the body. The differential equations are written (see Reference 17.)

Momentum Equation

$$\frac{d\theta}{dx} = - \left[(H + 2) \frac{1}{u_e} \frac{du_e}{dx} + \frac{1}{\rho_e} \frac{d\rho_e}{dx} + \frac{1}{r} \frac{dr}{dx} \right] \theta + \frac{C_f}{2} \qquad (12)$$

Energy Equation

$$\frac{d\Phi}{dx} = - \left[\frac{1}{u_e} \frac{du_e}{dx} + \frac{1}{\rho_e} \frac{d\rho_e}{dx} + \frac{1}{r} \frac{dr}{dx} \right] \Phi - \frac{q_w}{\rho_e u_e H_e^*} \qquad (13)$$

with the integral parameters

$$\theta = \delta \int_0^1 \left(1 - \frac{u}{u_e}\right) \frac{\rho u}{\rho_e u_e} d\left(\frac{y}{\delta}\right) \qquad (14)$$

$$\Phi = \delta \int_0^1 \left(1 - \frac{H^*}{H_e^*}\right) \frac{\rho u}{\rho_e u_e} d\left(\frac{y}{\delta}\right) \qquad (15)$$

$$H = \frac{\int_0^1 \left(1 - \frac{\rho u}{\rho_e u_e}\right) d\left(\frac{y}{\delta}\right)}{\theta/\delta} \qquad (16)$$

It is assumed that the mean Prandtl number and turbulent Prandtl number are unity. It is noted that this system of equations does not require explicit knowledge of turbulent shear stresses. The effect of these stresses are included in the skin friction and heat transfer correlations that are required for a solution.

A quadratic relation between total enthalpy h_t and velocity u is assumed (see Reference 17)

$$h_t = a + bu + cu^2 \qquad (17)$$

Equation (17) may be written

$$\frac{H^*}{H_e^*} = \frac{(1 - cu_e^2)}{H_e^*} \frac{u}{u_e} + \frac{cu_e^2}{H_e^*} \left(\frac{u}{u_e}\right)^2 \qquad (18)$$

The static enthalpy is then known

$$\frac{h}{h_e} = \frac{h_w}{h_e} + \left[1 - \frac{cu_e^2}{H_e^*}\right] \frac{H_e^*}{h_e} \frac{u}{u_e} + \left(\frac{cu_e^2}{H_e^*} - \frac{u_e^2}{2H_e^*}\right) \frac{H_e^*}{h_e} \left(\frac{u}{u_e}\right)^2 \qquad (19)$$

The density profile then becomes

$$\frac{\rho}{\rho_e} = \frac{h_e}{h} \frac{P}{P_e} \qquad (20)$$

where the gas is assumed to be calorically perfect. The static pressure profile is known from either experimental data or estimated from the method of characteristics. An approximate method for estimating the static pressure distribution through the boundary layer using a characteristics solution is given in Appendix II.

The power law velocity profile

$$\frac{u}{u_e} = \left(\frac{y}{\delta}\right)^m \qquad (21)$$

is used. As seen from the experimental data, Figure 22, the velocity power law assumption is reasonable. The power law exponent is assumed to obey the relation.

$$m = 1/2 \left\{ \frac{1}{1 - 1.47 \left[\frac{\log R_e' - 2.3686}{(\log R_e' - 1.5)^3}\right]^{1/2}} - 1 \right\} \qquad (22)$$

An alternate relation in terms of Reynolds number based on momentum thickness R_{e_e}' is

$$m = 1/2 \left\{ \frac{1}{1 - 1.47 \left[\frac{1.21 \log R_{e_e}' - .3996}{(1.21 \log R_{e_e}' + .469)^3}\right]^{1/2}} - 1 \right\}$$

Since turbulent theory has not been developed to the extent of relating shear stress directly to velocity profiles without empiricism, empirical correlations are necessary for skin friction predictions in turbulent boundary layers. The T' skin friction method, Reference 24, with the incompressible skin friction of Reference 22 is used. The local skin friction then becomes

$$C_f = \frac{.088\ (\log R_e' - 2.3686)\ \rho'/\rho_e}{(\log R_e' - 1.5)^3} \qquad (23)$$

The average skin friction C_F becomes

$$C_F = \frac{.088\ \rho'/\rho_e}{(\log_{10} R_e' - 1.5)^2}$$

The modified Reynolds analogy

$$\frac{q_w}{\rho_e u_e H_e^*} = \frac{cu_e^2/H_e^* - 1}{2} C_f P_r^{-2/3} \qquad (24)$$

is used. The prime values are based on the reference enthalpy

$$h'/h_e = 1 + .035 M_e^2 + .45 (h_w/h_e - 1)$$

Given the local flow properties ρ_e and u_e, and the body radius r along the body, equations 12 - 16 with the profiles, equations 18 - 22, and correlations, equations 23 and 24, form a complete system of equations which may be solved simultaneously for the boundary layer integral parameters along the body.

The two above theories have been compared using the Mach 5 compression surface at a free stream Mach number of 4 in terms of form factor and displacement thickness and the results are presented in Figure 43 (a). The agreement between the two theories is very good.

An interesting application of the Discontinuity/Analogy theory is the determination of the effect of centrifugal force phenomena on the boundary layer form factor. This was accomplished by calculating boundary layer characteristics with and without pressure gradients normal to the compression surface. The centrifugal force effects are accounted for by incorporating the experimental static pressure profiles in the integral parameters. Results are shown for the Mach 5 design model at a free stream Mach number of 6 in Figure 43 (b). Centrifugal force phenomena clearly have large favorable effects on boundary layer development.

CORRELATION OF THEORY AND EXPERIMENT

A correlation between the Discontinuity/Analogy theory and experimental data has been made. Representative results of form factor H_e and displacement thickness δ_e^* for the Mach 5 model at free stream Mach numbers of 4, 5, and 6, are shown in Figures 44 and 45 respectively. The effect of the step size on the form factor H_e was investigated for a free stream Mach number of 5, and the results are shown in Figure 44. It is seen that reducing the number of increments along the body from 40 to 8 has no significant effect on the form factor distribution. Since the Discontinuity/Analogy computer program does not include the capability of computing the general integral parameters discussed in the Experimental Data section, the conventional integral parameters, Equations (1) and (2), are used in these correlations. However, the pressure gradients normal to the wall are accounted for in the correlations by including the static pressure profiles in the density profiles, see the Volume II, step 13. The agreement between theory and experimental data is considered reasonable. However, both form factor H_e and displacement thickness δ^*_e could not be matched initially. This is due, basically, to the inability of the theory in its present state of development to match both the experimental velocity and temperature profiles at station zero. As an example, consider the total temperature profile on the Mach 5 model at free stream Mach number of 6. The velocity profile at station -.5 may be approximated by a power law profile with an exponent m of 1/9. The theoretical total temperature profile, predicted from Crocco's equation, is compared with the measured total temperature profile in Figure 46. It is noted that the temperature profiles are not in agreement. This, of course, results in a discrepancy between the theoretical and experimental integral parameters. This discrepancy indicates that further effort is required in the development of the theory. It is seen that the trends of the theory and experimental data are similar. Once a total temperature profile that agrees well with the experimental data has been developed, the integral parameters, displacement thickness and form factor can be matched initially. Then it is felt that better agreement between the theory and experimental data will be achieved.

Due to the above difficulty, two theoretical curves have been computed and are shown in each of Figures 44 and 45. One matches the initial form factor H_e and the other matches the initial displacement thickness δ^*_e. The difference between these two curves represents the effect on form factor of the difference between measured and theoretical temperature profiles.

Finally, the theoretical results are compared with typical experimental data taken on the heat transfer Mach 8 model at free stream Mach numbers 5, 6, and 8 and various wall temperatures in Figures 47 - 52. Here again, two theoretical curves are shown. One curve matches the initial form factor and the other curve matches the initial displacement thickness as shown in the figures. In the lower graphs on Figures 47 - 52, the theoretical displacement thickness is compared with the experimental data. It is felt that the correlations between the theory and experimental data are reasonable considering the difficulty in matching the total temperature profiles.

CONCLUSIONS

As a result of the combined experimental and analytical hypersonic boundary layer investigation reported herein the following conclusions are reached. These findings are pertinent to continuous compression surfaces typical of hypersonic inlets operating in the Mach 4 to 8 regime.

1. Heat transfer through a relatively thin cooled model wall, having a small temperature drop, can be measured accurately by means of an appropriately designed differential thermocouple.

2. Several boundary layer tripping devices were tested, including: (1) wires protruding normal to the surface, (2) air injection, and (3) vortex generators. Vortex generators provided the thinnest and least distorted boundary layer of any of the devices tested.

3. Strong pressure gradients normal to the compression surfaces were measured on all of the models tested. These gradients are a result of compression surface curvature in the streamwise direction and are, accordingly, a centrifugal force type phenomenon. This phenomenon produces significant favorable effects on boundary layer profile and thickness. These effects become more pronounced with increased Mach number and reductions in Reynolds number.

4. Cooling the compression surfaces resulted in thinning the boundary layer and corresponding improvement in velocity profiles. The heat flux increased significantly in the downstream region of the compression surfaces where large streamwise flow decelerations occurred.

5. Two existing boundary layer theories, termed (1) Discontinuity/Analogy Method and (2) Classical Method, were examined and found to be in agreement for a typical compression surface. Theoretical results were also found to be in general agreement with experimental data. An improved assumption for the temperature profile through the boundary layer would, however, result in a better correlation between theory and experiment.

RECOMMENDATIONS

The following research activities are recommended for advancing hypersonic inlet technology:

1. Analytical efforts should be initiated to provide an improved theoretical representation of the boundary layer temperature profile. This would result in improved correlation of theory and experiment.

2. A combined experimental and theoretical research program directed toward providing analytical means of predicting shock wave-boundary layer interaction in hypersonic inlets should be initiated.

3. Following completion of the foregoing efforts, a research program which utilizes these boundary layer theories for analyzing a family of hypersonic inlets should be initiated. Several of the more promising configurations would be selected for wind tunnel testing. These models would include representative wall cooling and boundary layer bleed. Real gas effects would be investigated to the extent possible with existing facilities. Finally, the results of these tests, in terms of boundary layer characteristics as well as throat and engine face pressure recoveries, would be correlated with theoretical results.

REFERENCES

1. McLafferty, G. R. and Barber, R. E., "Turbulent Boundary Layer Characteristics in a Supersonic Stream Having Adverse Pressure Gradients," UAC Research Laboratories Report R-1285-11, Sept., 1959.

2. Kepler, C. E. and O'Brien, R. L., "Supersonic Turbulent Boundary Layer Growth Over Cooled Walls in Adverse Pressure Gradients,"ASD Technical Report No. 62-87, Oct. 1962.

3. van Driest, E. R., "Turbulent Boundary Layer in Compressible Fluids," J. Aeronaut. Sci., 18, 145-160, 1951.

4. Test Facilities Handbook, (5th Edition). von Karman Gas Dynamics Facility Vol. 4, Arnold Engineering Development Center, July, 1963.

5. Howarth, L., "Modern Developments in Fluid Dynamics,High Speed Flow," Oxford Press, 1956, p. 293.

6. von Doenhoff, A. E. and Tetervin, N., "Determination of General Relations for the Behavior of Turbulent Boundary Layers," NACA Report 772, 1943.

7. Tetervin, N. and Lin, C. C., "A General Integral Form of the Boundary Layer Equation for Incompressible Flow with an Application to the Calculation of the Separation Point of Turbulent Boundary Layers," NACA Report 1046, 1951.

8. Schubauer, G. B. and Klebanoff, P.S., "Investigation of Separation of the Turbulent Boundary Layer,"NACA Report 1030, 1951.

9. Rubert, K. F. and Persh, J., "A Procedure for Calculating the Development of the Turbulent Boundary Layers under the Influence of Adverse Pressure Gradients," NACA TN 2478, 1951.

10. Sandborn, V. A. and Slogar, R. J., "Study of the Momentum Distribution of Turbulent Boundary Layers in Adverse Pressure Gradients," NACA TN 3264,1955.

11. Clauser, F. H., "Turbulent Boundary Layers in Adverse Pressure Gradients," J. Aeronaut. Sci., 21, 91-108, 1954.

12. Truckenbrodt, E., "A Method of Quadrature for Calculation of the Laminar and Turbulent Boundary Layer in Case of Plane and Rotationally Symmetrical Flow," NACA TM 1379, 1955.

13. Rotta, J., "On the Theory of the Turbulent Boundary Layer,"NACA TM 1344, 1953.

14. Coles, D. E., "The Turbulent Boundary Layer in a Compressible Fluid," Rand Corp. Report R-403-PR, 1962.

15. Englert, G. W., "Estimation of Compressible Boundary-Layer Growth over Insulated Surfaces with Pressure Gradient," NACA TN 4022, 1957.

16. Reshotko, E. and Tucker, M., "Approximate Calculation of the Compressible Turbulent Boundary Layer with Heat Transfer and Arbitrary Pressure Gradient," NACA TN 4154, 1957.

17. Cohen, N. B., "A Method for Computing Turbulent Heat Transfer in the Presence of a Streamwise Pressure Gradient for Bodies in High-Speed Flow," NASA Memo 1-2-59L, 1959.

18. Crocco, L., "Transformations of the Compressible Turbulent Boundary Layer with Heat Exchange," AIAA Jour., 1, 2723-2731, 1963.

19. Stewartson, K., "Correlated Incompressible and Compressible Boundary Layer," Proc. Roy. Soc. (London) 200A, 84-100, 1949.

20. McLafferty, G. H. and Barber, R. E., "The Effect of Adverse Pressure Gradients on the Characteristics of Turbulent Boundary Layers in Supersonic Streams," J. Aerospace Sci., 29, 1-11, 1962.

21. Stroud, J. F. and Coleman, D. M., "Hypersonic Inlet Boundary Layer Prediction," ARS Jour., 32, No. 5, May, 1962.

22. Sivells, J. C. and Payne, R. G., "A Method of Calculating Turbulent Boundary-Layer Growth at Hypersonic Mach Numbers," AEDC TR-59-3, 1959.

23. Cohen, N. B., "Relations Between Heat, Mass, and Momentum Transfer in Laminar and Turbulent Boundary Layers," RAD-2-TR-57-33, AVCO Res. and Advanced Dev., Sept., 1957.

24. Sommer, S. C. and Short, B. J. "Free-Flight Measurements of the Turbulent-Boundary-Layer Skin Friction in the Presence of Severe Aerodynamic Heating at Mach Numbers from 2.8 to 7.0," NACA TN 3391, 1955.

TABLE I

SUMMARY OF BOUNDARY LAYER TESTS
IN AEDC TUNNELS A & B

AEDC Tunnel	Mo	P_{t_o} psi	T_{t_o} °R	T_w °R	Model Design	Generating Cylinder Length in Inches	Trips	Re/ℓ_∞ $\times 10^{-6}$
A	4	75	580	-	5	17	Vortex Gen. Front	6.37
"	"	10	"	-	"	"	"	.85
"	5	150	640	-	"	"	"	6.9
"	"	40	"	-	"	"	"	1.84
"	6	200	720	-	"	"	"	5.2
"	"	100	"	-	"	"	"	2.6
A	4	75	580	-	5	9	"	6.37
"	"	10	"	-	"	"	"	.85
"	6	200	720	-	"	"	"	5.2
"	"	100	"	-	"	"	"	2.6
A	4	75	580	-	6	17	"	6.37
"	6	200	720	-	"	"	"	5.2
"	"	100	"	-	"	"	"	2.6
A	5	150	640	400	8	12.36	"	6.9
"	"	40	"	"	"	"	"	1.84
"	"	150	"	480	"	"	"	6.9
"	"	40	"	"	"	"	"	1.84
"	"	150	"	Uncool	"	"	"	6.9
"	"	40	"	"	"	"	"	1.84
A	6	200	720	400	8	12.36	"	5.2
"	"	100	"	"	"	"	"	2.6
"	"	200	"	506	"	"	"	5.2
"	"	100	"	"	"	"	"	2.6
"	"	200	"	Uncool	"	"	"	5.2
"	"	100	"	"	"	"	"	2.6
A	4	75	580	-	10	17	"	6.37
"	"	10	"	-	"	"	"	.85
"	5	150	"	-	"	"	"	6.9
"	"	40	"	-	"	"	"	1.84
"	6	200	"	-	"	"	"	5.2
"	"	100	"	-	"	"	"	2.6

TABLE (cont'd)

SUMMARY OF BOUNDARY LAYER TESTS
IN AEDC TUNNELS A & B

AEDC Tunnel	Mo	P_{t_o} psi	T_{t_o} °R	T_w °R	Model Design	Generating Cylinder Length in Inches	Trips	$Re/_1]_\infty$ -6 x10
B	8	800	1,350	490	8	24.73	Vortex Gens. Front-Rear	3.68
"	"	335	1,320	"	"	"	"	1.61
"	"	800	1,350	530	"	"	"	3.68
"	"	335	1,320	"	"	"	"	1.61
"	"	800	1,350	830	"	"	"	3.68
"	"	335	1,320	"	"	"	"	1.61
"	"	800	1,350	Uncool	"	"	"	3.68
"	"	335	1,320	"	"	"	"	1.61
B	8	800	1,350	Uncool	10	17	Vortex Gen. Front	3.68
"	"	"	"	"	"	"	Vortex Gen. Front-Rear	3.68
"	"	"	"	"	"	9	Vortex Gen. Front	3.68
"	"	500	1,335	"	"	17	"	2.40

APPENDIX I

A GENERAL DISCONTINUITY/ANALOGY PROCEDURE WITH PRESSURE GRADIENT NORMAL TO THE WALL

A general Discontinuity/Analogy procedure is described in this section to treat a turbulent boundary layer with pressure gradient normal to the wall. The procedure is similar to the method described in the report, but the boundary layer thicknesses δ along the body are not required.

At the initial station x_1 the boundary layer thickness δ_1, displacement thickness δ^*_1, and form factor H_1 are to be given as well as a bivariant table of P (x,y) and the values of total temperature T_{t_o}, wall temperature T_w, total pressure Pt_o, and local Mach number M_e (x).

The following boundary layer profiles are used:

Velocity Profile:

$$\frac{u}{u_e} = \left(\frac{y}{\delta}\right)^m \tag{1}$$

Density Profile:

$$\frac{\rho}{\rho_e} = \frac{T_e}{T} \cdot \frac{P}{P_e} \tag{2}$$

Temperature Profile:

$$\frac{T}{T_e} = \frac{h_w}{h_e} + \left[1 - \frac{C\,U_e^2}{H_e^*}\right] \frac{H_e^*}{h_e} \frac{u}{u_e} + \left[\frac{C\,U_e^2}{H_e^*} - \frac{U_e^2}{2\,H_e^*}\right] \frac{H_e^*}{h_e} \left(\frac{u}{u_e}\right)^2 \tag{3}$$

Inital guesses for m_1 and $C\,U_e^2/H_e^*\Big]_1$ are made and the integral parameters

$$\delta^* = \int_o^\delta \left(1 - \frac{\rho\, u}{\rho_e\, u_e}\right) dy \tag{4}$$

$$\theta = \int_o^\delta \frac{\rho\, u}{\rho_e\, u_e} \left(1 - \frac{u}{u_e}\right) dy \tag{5}$$

$$H = \delta^*/\theta \tag{6}$$

are computed. Then the initial values of m and $C\,U_e^2/H_e^*$ are found, through an optimization program, such that the given initial values of δ_1, δ_1^*, and H_1 are satisfied. The initial energy thickness ϕ_1 is computed.

$$\phi_i = \int_0^{\delta} \frac{\rho u}{\rho_e U_e} \left(1 - \frac{H^*}{H_e^*}\right) dy \tag{7}$$

The effective Reynolds numbers Re_{eff_i} and $Re_{eff_{i+1}}$ and distances x_{eff_i} and $x_{eff_{i+1}}$ and power law exponent m_{i+1} are found as previously. The skin friction is computed again using Sivells and Payne correlation, Reference 22,

$$C_{f_{i-i+1}} = \frac{.088\,(\log \bar{R}_e' - 2.3686)\,\rho'/\rho_e}{(\log \bar{R}_e' - 1.5)^3} \tag{8}$$

where

$$\bar{R}_e' = \frac{R_{e_i}' + R_{e_{i+1}}'}{2}$$

Now from the momentum and energy equations:

$$\theta_{i+1} = \theta_i + \frac{1}{2} C_{f_{i-i+1}} \Delta X_{i-i+1} \tag{9}$$

$$\phi_{i+1} = \phi_i + \frac{1}{2} C_{f_{i-i+1}} \left\{1 - \frac{1}{2}\left[\left(\frac{C\,U_e^2}{H_e^*}\right)_i + \left(\frac{C\,U_e^2}{H_e^*}\right)_{i+1}\right]\right\} \frac{\Delta x_{i-i+1}}{Pr^{2/3}} \tag{10}$$

The parameters δ_{i+1} and $C\,U_e^2/H_e^*\big|_{i+1}$ are perturbed, through an optimization program, such that θ_{i+1} and ϕ_{i+1}, computed from the integral equations (5) and (7), agree with θ_{i+1} and ϕ_{i+1} computed from the differential equations. Then the values δ_{i+1} and $C\,U_e^2/H_e^*\big|_{i+1}$ are known.

For the discontinuity component the values m_{i+1}, δ_{i+1}, $C\,U_e^2/H_e^*\big|_{i+1}$, θ_{i+1}, and ϕ_{i+1} are known at x_{i+1} just upstream of the discontinuity. Again

using an optimization program with three variables, the parameters downstream of the discontinuity, m_{i+2}, δ_{i+2}, and $C\, U_e^2/H_e^*\big]_{i+2}$ are perturbed such that the following three equations are satisfied.

Energy Equation Across Discontinuity:

$$\left| \frac{(\rho_e U_e \phi)_{i+1} - (\rho_e U_e \phi)_{i+2}}{(\rho_e U_e \phi)_{i+1}} \right| \leq .001 \qquad (11)$$

Momentum Equation Across Discontinuity:

$$\left| \frac{\delta^*/\theta\big]_{i+2} - \left\{ \begin{array}{l} 2\, \dfrac{\delta_{i+2}}{\delta_{i+1}} \cdot \dfrac{q_{e_{i+2}}}{P_{e_{i+1}}} \left(\dfrac{\delta^*}{\delta}\right)_{i+2} \\ \hline 2\, \dfrac{\delta_{i+2}}{\delta_{i+1}} \dfrac{q_{e_{i+2}}}{P_{e_{i+1}}} \left[1 - \left(\dfrac{\delta^*}{\delta}\right)_{i+2} \right] \\ -2\, \dfrac{q_{e_{i+1}}}{P_{e_{i+1}}} \left[1 - \left(\dfrac{\delta^*}{\delta}\right)_{i+1} - \left(\dfrac{\theta}{\delta}\right)_{i+1} \right] \\ + \dfrac{1}{2} \left[1 - \dfrac{\delta_{i+2}}{\delta_{i+1}} \right] \left[1 + \dfrac{P_{e_{i+2}}}{P_{e_{i+1}}} \right] \\ - \dfrac{\overline{P}_{i+1}}{P_{e_{i+1}}} + \dfrac{\overline{P}_{i+2}}{P_{e_{i+1}}} \dfrac{\delta_{i+2}}{\delta_{i+1}} \end{array} \right\}}{\delta^*/\theta\big]_{i+2}} \right| \leq .001 \qquad (12)$$

Continuity Equation Across Discontinuity:

$$\left| \frac{\delta_{i+2} - \dfrac{(\rho_e U_e)_{i+1}}{(\rho_e U_e)_{i+2}} \delta_{i+1} \left[\dfrac{1 - (\delta^*/\delta)_{i+1}}{1 - (\delta^*/\delta)_{i+2}} \right]}{\delta_{i+2}} \right| \leq .001 \qquad (13)$$

When these equations are satisfied, the conditions downstream of the discontinuity are known, and the procedure for the next restoring component is repeated. A simplified flow diagram for this program is illustrated in Figure 53.

APPENDIX II

PREDICTING PRESSURE DISTRIBUTION NORMAL TO THE WALL IN PRESSURE GRADIENT FLOWS

The problem of predicting pressure distribution through the boundary layer and normal to a curved wall is treated in this section. A prediction is necessary in existing boundary layer theories to account for pressure gradients normal to the wall since experimental static pressure profiles are not always available. An approximate method for predicting pressure gradients normal to the wall is suggested. The method consists of obtaining an inviscid or characteristics solution to the body which is corrected for boundary layer displacement thickness δ^*_w. The body is corrected by adding the calculated displacement thickness δ^*_w normal to the physical body surface. It has been found that the static pressure distribution normal to the wall from this corrected inviscid solution approximates the actual static pressure distribution normal to the wall in the boundary layer.

Consider the static pressure profiles obtained from the static probe measurements on the Mach 10 compression surface in Figure 8. These static pressure profiles are duplicated in Figure 54 and are compared with the inviscid static pressure profiles at the corresponding stations obtained by the method discussed above. The experimental displacement thickness δ^*_w was used here to correct the body for the boundary layer. Since the streamlines for both the viscous and inviscid flows are matched at the corresponding surface, the static pressures should also be matched at the corresponding surface. This has been done in the above comparison. The agreement between the viscous and corrected inviscid pressure profiles is felt to be reasonable considering the complexity of the flow field. The wall static pressure distribution for the corrected inviscid solution is compared to the measured static pressures in Figure 55. It is noted that the agreement is very good and indicates that the actual wall static pressure may be estimated from a characteristics solution corrected for boundary layer displacement thickness.

In the absence of experimental pressure distribution data, the calculation procedure involves first obtaining the characteristics solution neglecting the displacement thickness. Then using the results from this characteristics solution in the boundary layer theory, compute the displacement thickness δ^*_w, and recompute the characteristics solution correcting the body for the above displacement thickness δ^*_w. If the displacement thickness δ^*_w is relatively small compared to the body, one iteration of the characteristics solution is sufficient.

APPENDIX III

HEAT TRANSFER BENCH TEST

A heat transfer bench test was initiated to determine if steady state heat transfer could be measured across a relatively thin stainless steel wall. The nominal heat flux on the cylinder installed in Tunnel B with a wall temperature at 490°R is approximately 3000 BTU/hr/ft^2. This corresponds to a temperature drop across the stainless steel wall of approximately 6 degrees. The furnace used to simulate the cooled cylinder of the heat transfer Mach 8 model in Tunnel B for the bench tests is shown schematically in Figure 56. The outer insulation and teflon seals are to minimize outward radial and longitudinal heat fluxes. A watt-meter, voltmeter, and ammeter were used to measure the heat input to the main heater. A schematic of the stainless steel specimen is shown in Figure 57. The thermocouple junctions are constructed of .010 inch diameter constantan wires soldered in circumferential grooves in the stainless steel specimen. The thermocouple locations are shown in Figure 57. The distance between the thermocouples at a given station on the specimen is 0.178 inch. The thermocouples on the stainless steel specimen measure absolute temperatures using the common lead system, and the pairs of thermocouples across the specimen wall measure differential temperatures directly by a special wiring hook-up. This hook-up, shown in Figure 58, uses the stainless steel wall as one leg of the differential thermocouple. Since the reference temperature thermocouples are at the same temperature, they do not enter into the differential thermocouple reading. Note the reference thermocouple junction is copper-constantan, and the main thermocouple junction is stainless steel-constantan. Since this is not a standard thermocouple installation, a special calibration was required. This was done resulting in the calibration curve shown in Figure 59.

Some representative data obtained from the bench tests are shown in Figure 60. The main heater heat fluxes of 2330 and 3460 BTU/hr/ft^2 correspond approximately to the heat fluxes on the cylinder of the heat transfer model. The absolute and differential thermocouple readings are given in Figure 60 along with the difference between absolute temperatures across the wall. As seen from these tests, Figure 60, the longitudinal temperature distributions are reasonably constant indicating small longitudinal heat transfer. The outward radial heat flux through the outer insulation was found to be negligible compared to the inward radial heat flux to the stainless steel specimen. Thus, the main heater heat flux is approximately equal to the heat flux to the main specimen. This known heat flux can be compared to the computed heat flux to the main specimen from Fourier's law.

Using the results shown in Figure 60, the average wall temperature and temperature drop across the wall are 71.4° F. and 4.02° F. , respectively, for the 2330 BTU/hr/ft^2 heat flux. The thermal conductivity of stainless steel at 71.4° F. is 8.54 BTU/hr° ft^2/ ft. Then the computer heat flux to the specimen becomes

HEAT TRANSFER BENCH TEST

$$q_c = - k \frac{\Delta T}{\Delta h}$$

$$= - \frac{8.54 \times 4.02}{.178/12}$$

$$= - 2314 \quad \frac{BTU}{hr\ ft^2}$$

This computed heat flux agrees well with the heater heat flux of 2330 BTU/hr/ft^2. Similarly, the computed heat flux for the higher heater flux of 3460 BTU/hr/ft^2 shown in Figure 60 was found to be 3280 BTU/hr/ft^2. These results indicate that a steady state heat flux of approximately 3000 BTU/hr/ft^2 across a stainless steel wall, approximately 0.20 inches thick, can be computed with reasonable accuracy.

MACH 10 DESIGN MODEL

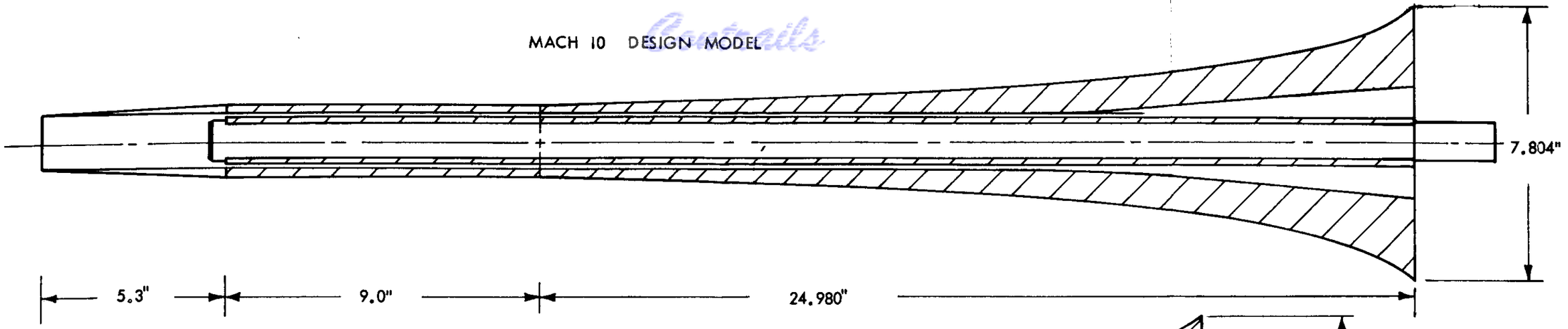

MACH 6 DESIGN MODEL

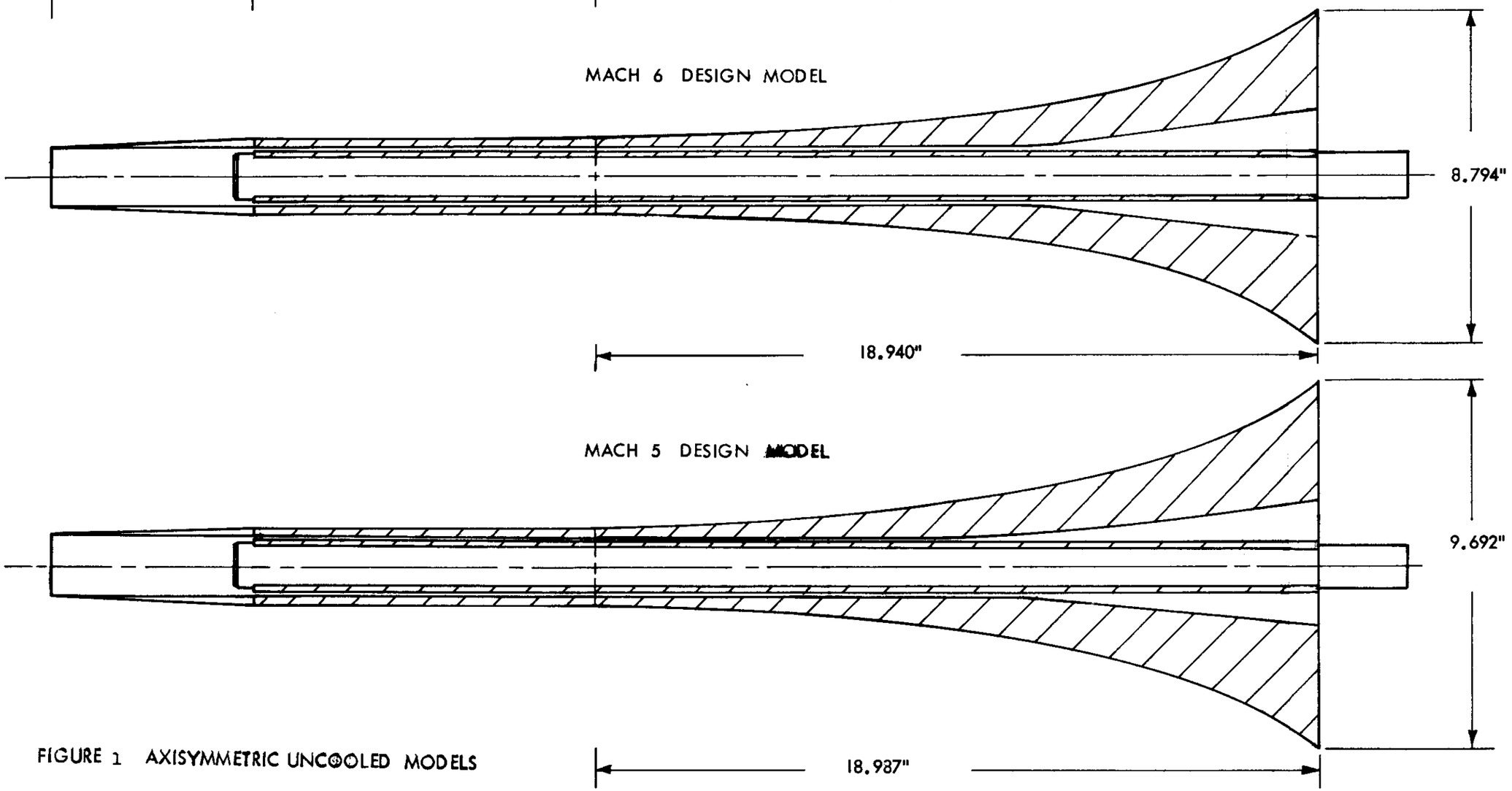

MACH 5 DESIGN MODEL

FIGURE 1 AXISYMMETRIC UNCOOLED MODELS

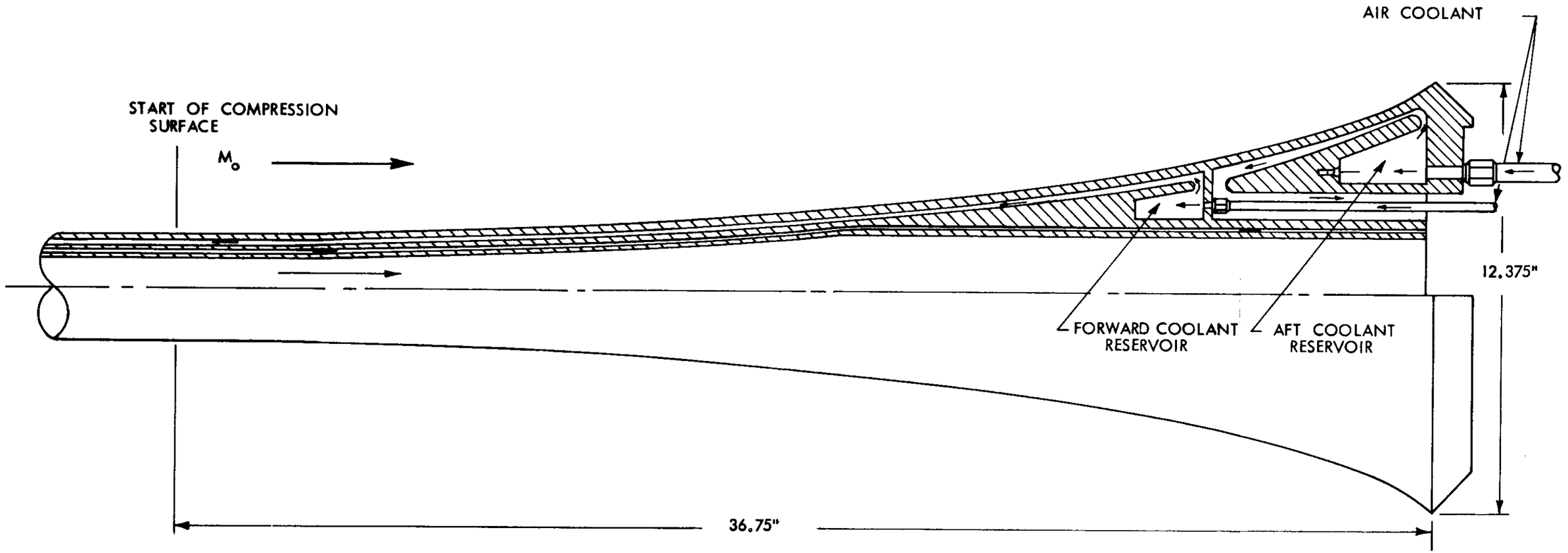

FIGURE 2 HEAT TRANSFER MACH 8 MODEL

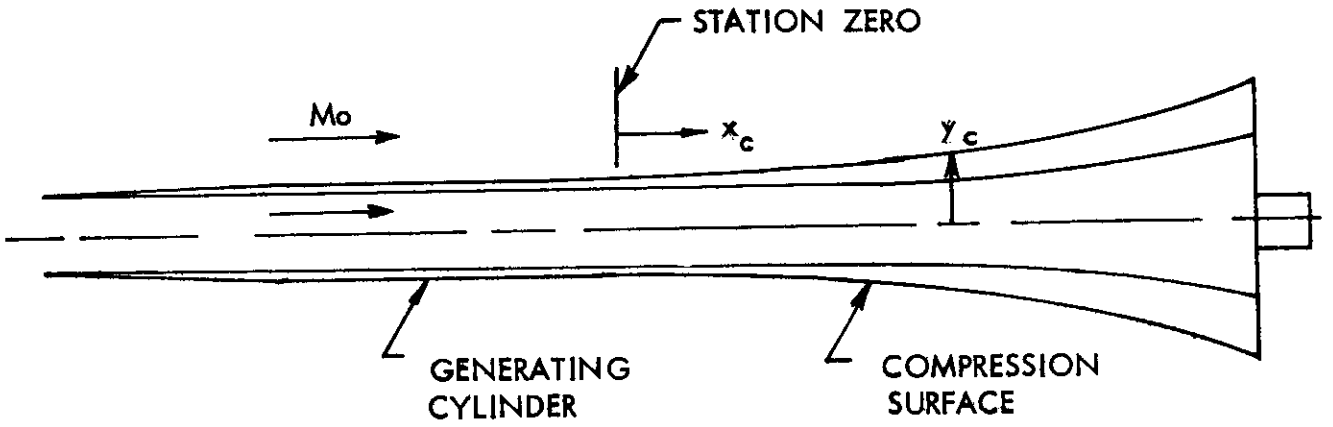

Mach 5 Design

x_c	y_c	x_c	y_c	x_c	y_c
.001	1.000	13.878	2.498	16.944	3.496
1.368	1.013	14.131	2.562	17.017	3.530
2.626	1.050	14.367	2.624	17.087	3.562
3.778	1.104	14.588	2.684	17.153	3.593
4.830	1.169	14.796	2.742	17.216	3.623
5.791	1.244	14.990	2.798	17.276	3.653
6.668	1.324	15.173	2.853	17.333	3.681
7.470	1.408	15.345	2.906	17.387	3.709
8.204	1.493	15.507	2.957	17.439	3.736
8.877	1.579	15.660	3.007	17.487	3.762
9.495	1.664	15.803	3.055	17.534	3.788
10.064	1.749	15.939	3.101	17.578	3.812
10.558	1.832	16.066	3.147	17.661	3.860
11.072	1.914	16.187	3.190	17.736	3.904
11.520	1.994	16.301	3.233	17.804	3.947
11.934	2.072	16.408	3.274	17.886	3.986
12.319	2.148	16.510	3.314	17.923	4.024
12.677	2.222	16.607	3.353	17.974	4.060
13.009	2.294	16.698	3.390	18.022	4.094
13.319	2.364	16.784	3.427	18.085	4.141
13.608	2.432	16.866	3.462	18.140	4.185
				18.157	4.198
				Conical	
				18.987	4.846

Mach 6 Design

x_c	y_c	x_c	y_c	x_c	y_c
0	1.000	13.968	2.282	16.901	3.116
1.549	1.014	14.238	2.341	16.977	3.146
2.951	1.052	14.489	2.399	17.048	3.175
4.217	1.106	14.722	2.455	17.115	3.203
5.357	1.172	14.939	2.508	17.179	3.230
6.386	1.245	15.140	2.560	17.238	3.256
7.314	1.323	15.328	2.610	17.295	3.281
8.153	1.403	15.502	2.658	17.398	3.329
8.913	1.484	15.666	2.704	17.491	3.373
9.603	1.565	15.818	2.749	17.574	3.415
10.230	1.645	15.960	2.792	17.648	3.454
10.802	1.724	16.094	2.833	17.715	3.490
11.325	1.801	16.219	2.873	17.774	3.524
11.804	1.877	16.336	2.912	17.828	3.556
12.243	1.950	16.445	2.949	17.877	3.586
12.646	2.020	16.548	2.985	17.921	3.614
13.017	2.089	16.645	3.020	17.979	3.652
13.359	2.155	16.736	3.053	18.029	3.688
13.675	2.220	16.821	3.085	18.073	3.720
				18.110	3.749
				Conical	
				18.94	4.397

All Coordinates in Inches

FIGURE 3 EXTERNAL COORDINATES OF AXISYMMETRIC WIND TUNNEL MODELS

FIGURE 3 (Continued)

Mach 8 Design

x_c	y_c	x_c	y_c	x_c	y_c
.0045	1.500	27.8505	3.4590	33.5085	4.6935
2.0265	1.5090	28.1880	3.5160	33.6000	4.7220
3.9285	1.5345	28.5105	3.5715	33.6900	4.7490
5.7090	1.5750	28.8165	3.6270	33.7755	4.7760
7.3725	1.6245	29.1090	3.6795	33.8565	4.8015
8.9280	1.6830	29.3880	3.7320	33.9360	4.8270
10.3815	1.7475	29.6535	3.7815	34.0125	4.8510
11.7390	1.8165	29.9070	3.8310	34.0860	4.8750
13.0080	1.8900	30.1485	3.8805	34.1580	4.8990
14.1960	1.9665	30.3810	3.9270	34.2255	4.9230
15.3075	2.0430	30.6015	3.9735	34.2915	4.9455
16.3500	2.1225	30.8130	4.0170	34.3560	4.9645
17.3265	2.2005	31.0155	4.0620	34.4175	4.9890
18.2430	2.2800	31.2090	4.1040	34.4760	5.0100
19.1055	2.3595	31.3935	4.1460	34.5885	5.0505
19.9154	2.4375	31.5705	4.1865	34.6920	5.0895
20.6775	2.5140	31.7415	4.2270	34.7895	5.1270
21.3960	2.5905	31.9440	4.2660	34.8810	5.1630
22.0725	2.6655	32.0595	4.3035	34.9650	5.1960
22.7115	2.7390	32.2095	4.3395	35.0820	5.2455
23.3160	2.8110	32.3520	4.3770	35.1885	5.2905
23.8860	2.8830	32.4900	4.4115	35.3130	5.3460
24.4260	2.9520	32.6220	4.4460	35.4495	5.4105
24.9375	3.0210	32.7495	4.4790	35.5650	5.4675
25.4205	3.0870	32.8710	4.5120	35.6820	5.5290
25.8795	3.1530	32.9880	4.5450	35.8095	5.5995
26.3160	3.2175	33.1005	4.5765	35.9190	5.6670
26.7300	3.2790	33.2085	4.6065	36.0045	5.7240
27.1215	3.3405	33.3120	4.6365	36.0510	5.7570
27.4950	3.4005	33.4125	4.6650	36.0645	5.7675

Conical

36.750 6.188

Mach 10 Design

x_c	y_c	x_c	y_c	x_c	y_c
0	1.000	18.906	2.085	22.536	2.752
1.614	1.007	19.160	2.121	22.602	2.769
3.110	1.026	19.399	2.156	22.665	2.786
4.490	1.054	19.626	2.190	22.725	2.802
5.762	1.089	19.839	2.223	22.783	2.817
6.935	1.129	20.041	2.256	22.838	2.832
8.017	1.173	20.232	2.287	22.891	2.847
9.015	1.220	20.412	2.317	22.942	2.861
9.938	1.268	20.583	2.347	22.990	2.875
10.792	1.318	20.745	2.375	23.036	2.888
11.582	1.369	20.899	2.403	23.080	2.902
12.315	1.419	21.044	2.430	23.164	2.927
12.996	1.469	21.182	2.456	23.240	2.951
13.628	1.519	21.313	2.482	23.310	2.973
14.217	1.569	21.438	2.506	23.374	2.994
14.765	1.617	21.556	2.530	23.434	3.015
15.277	1.665	21.668	2.554	23.515	3.043
15.754	1.712	21.775	2.576	23.608	3.078
16.201	1.758	21.877	2.598	23.688	3.109
16.619	1.802	21.974	2.619	23.757	3.137
17.010	1.846	22.066	2.640	23.843	3.174
17.377	1.889	22.154	2.660	23.912	3.206
17.722	1.930	22.238	2.680	23.984	3.242
18.045	1.970	22.317	2.699	24.056	3.281
18.350	2.010	22.394	2.717	24.103	3.310
18.636	2.048	22.466	2.735	24.150	3.342

Conical

24.980 3.902

All Coordinates in Inches

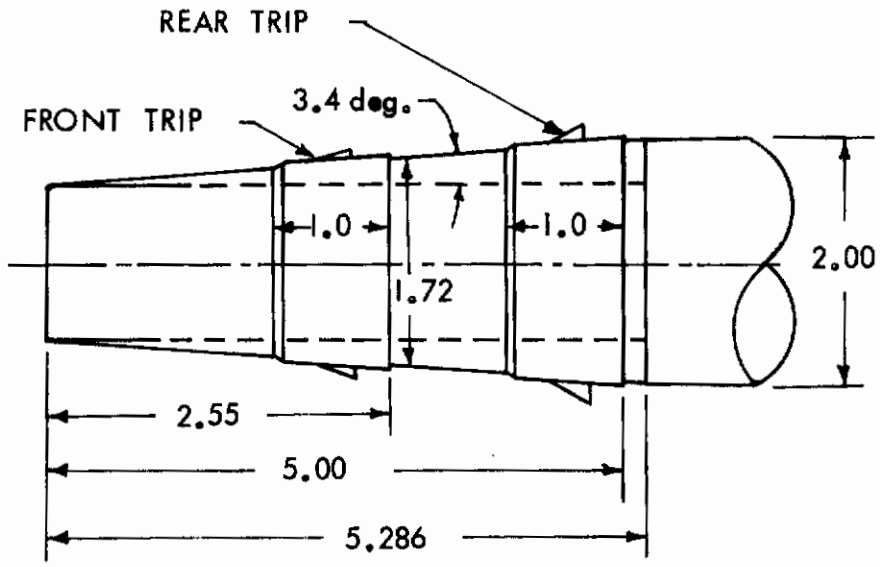

ALL DIMENSIONS IN INCHES

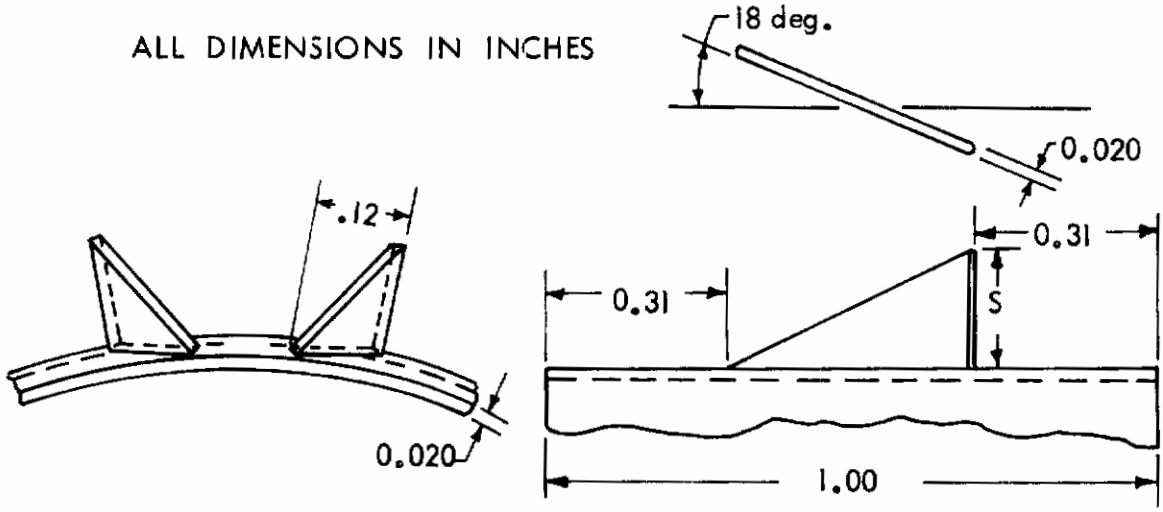

VORTEX GENERATOR DIMENSIONS

Alternate Vortex Generators Turned in Opposite Directions, 16 Evenly Spaced

Trip	S
Rear	0.16
Front	0.08

FIGURE 4 INLET AND VORTEX GENERATORS FOR UNCOOLED MODELS

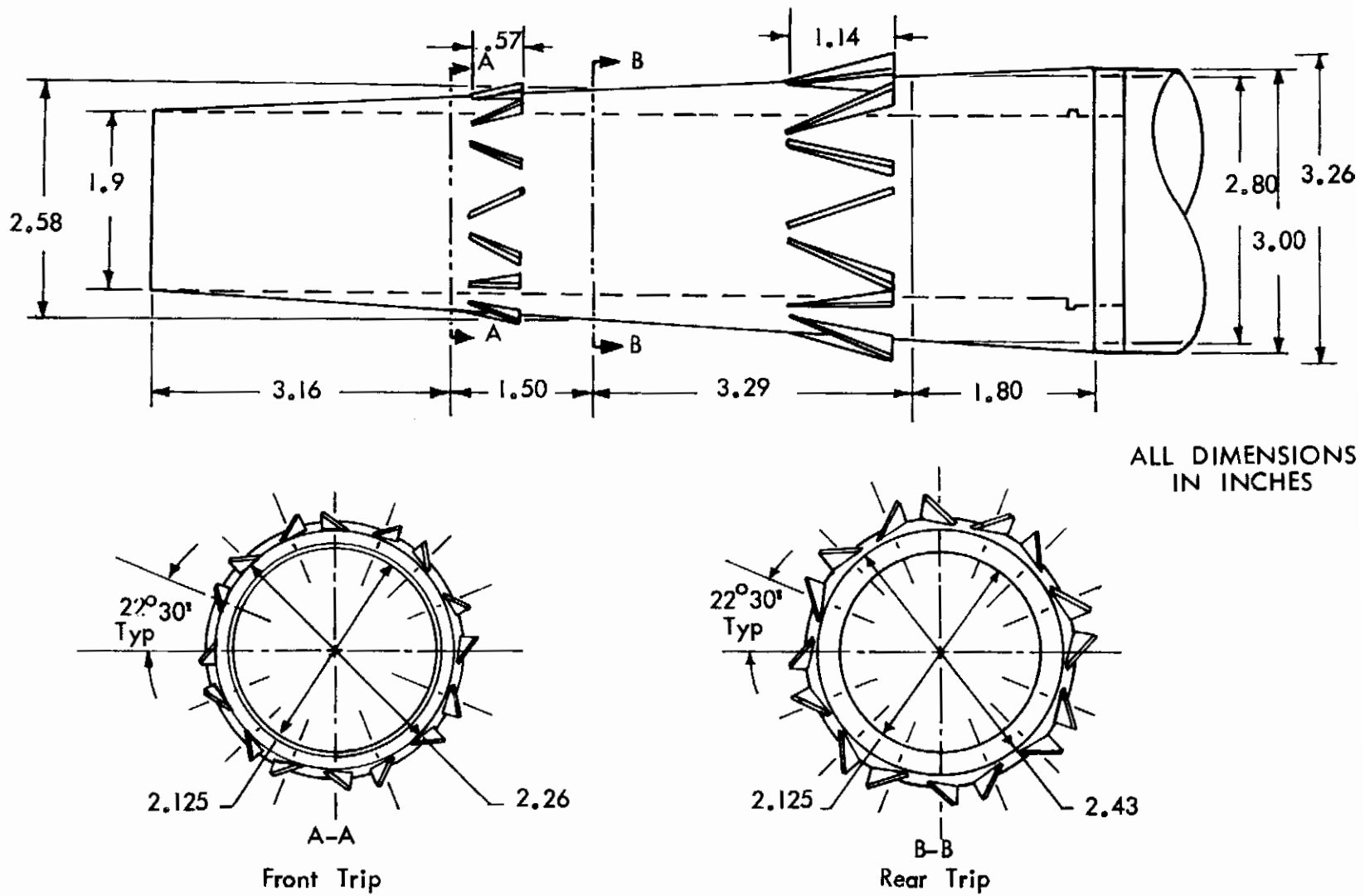

FIGURE 5 INLET AND VORTEX GENERATORS FOR HEAT TRANSFER MODEL

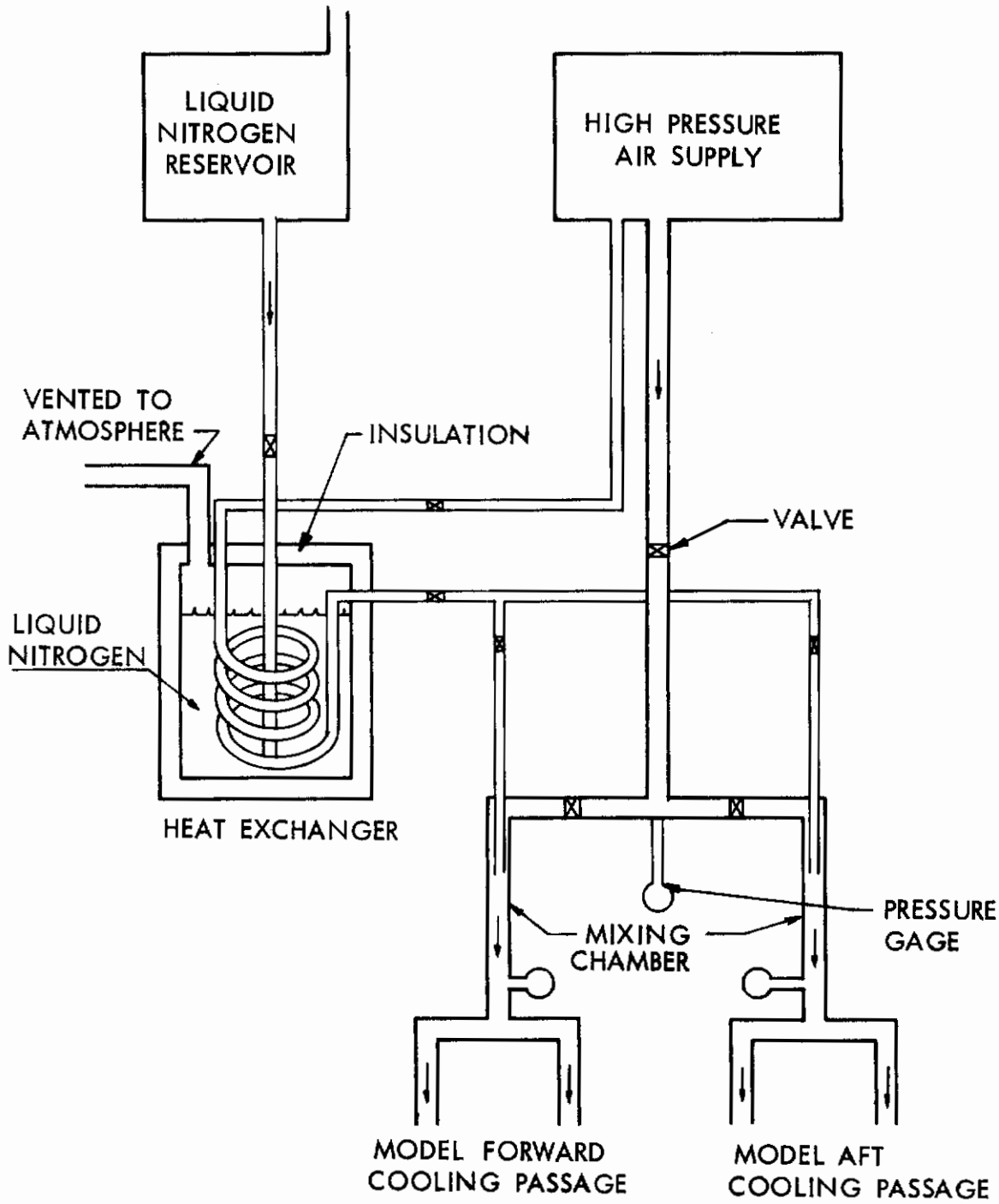

FIGURE 6. COOLING SYSTEM SCHEMATIC

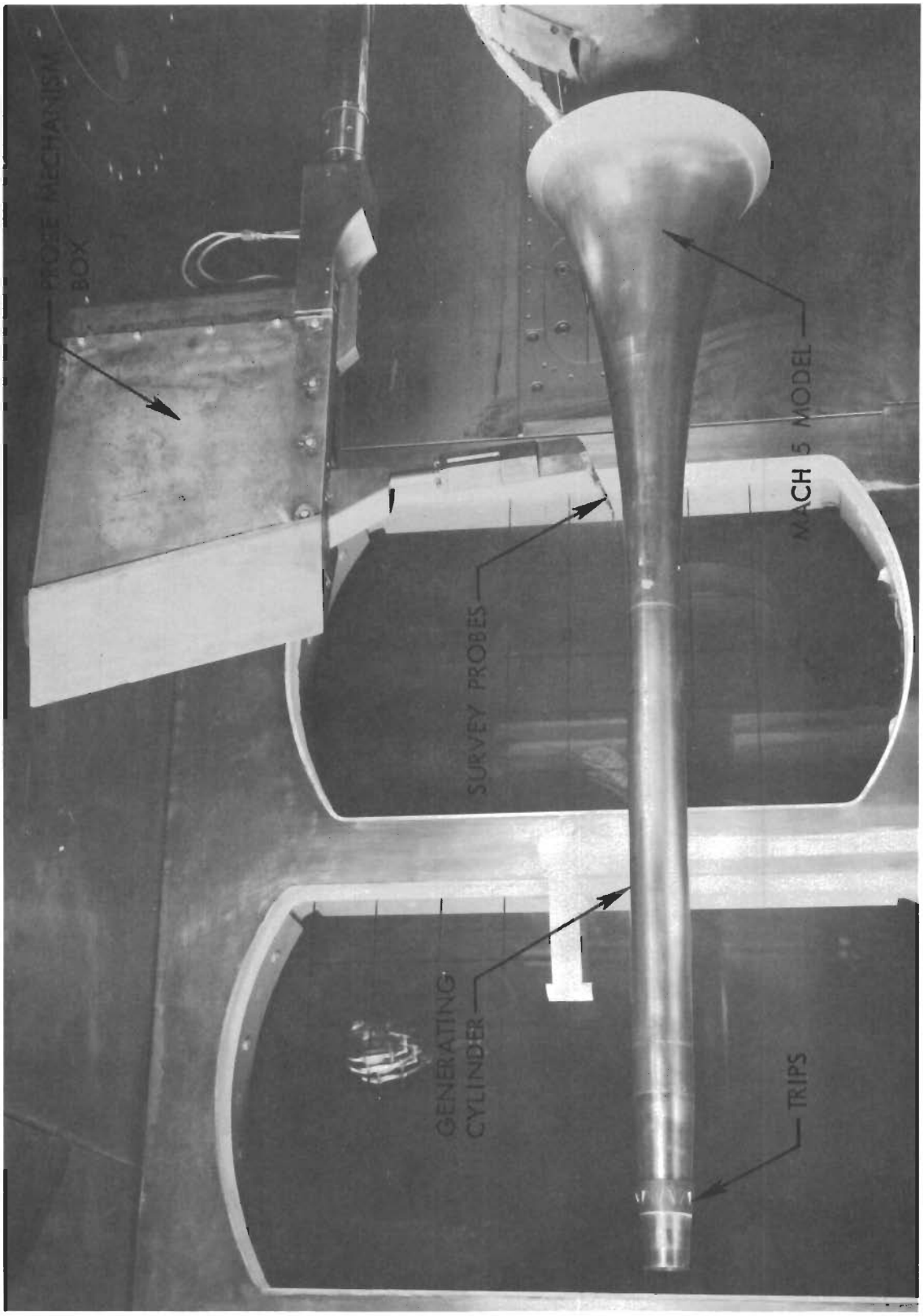

FIGURE 7. MACH 5 MODEL IN AEDC TUNNEL A

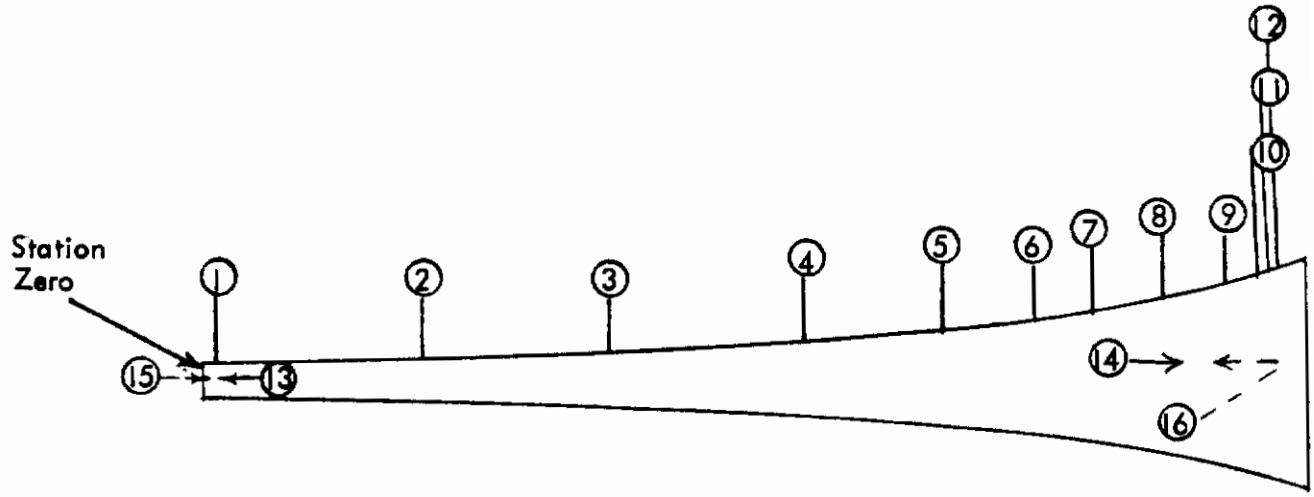

Circled numbers indicate static pressure tube numbers and chromel-alumel thermocouple numbers.

Static Pressure and Thermocouple Numbers	Station X Inches
1	.5
2	4.5
3	8.5
4	12.5
5	16.
6	18.
7	20.
8	22.
9	23.
10	23.5
11	23.75
12	24
*13	.5
*14	22
*15	.5
*16	22

* Pressure Only

FIGURE 8 MACH 10 MODEL INSTRUMENTATION

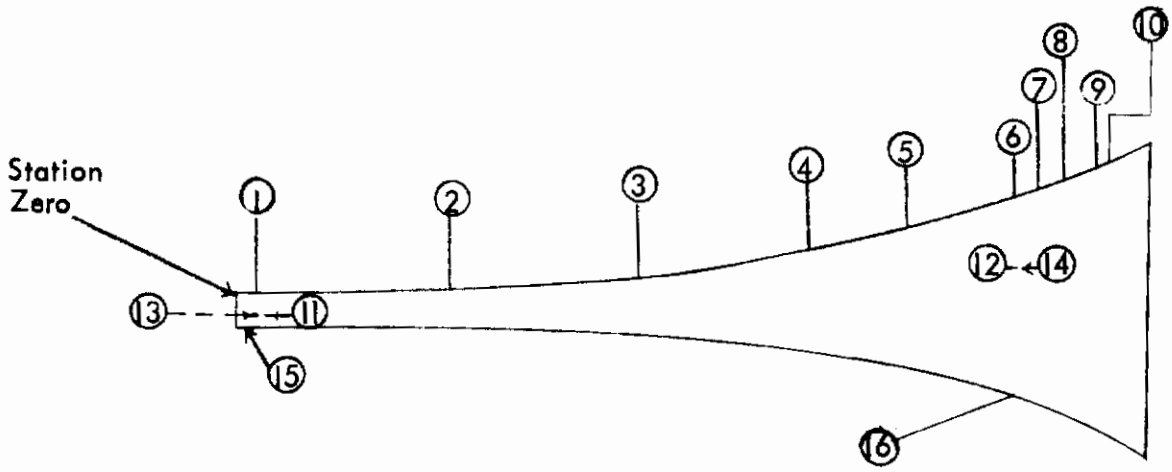

Circled numbers indicate static pressure tube numbers and chromel-alumel thermocouple numbers.

Static Pressure and Thermocouple Numbers	Station X Inches
1	.5
2	4.5
3	8.5
4	12
5	14
6	16
7	17
8	17.5
9	18
10	18.15
*11	.5
*12	16
*13	.5
*14	16
*15	.5
*16	16

* Pressure Only

FIGURE 9 MACH 5 AND 6 MODEL INSTRUMENTATION

9" Generating Cylinder Instrumentation

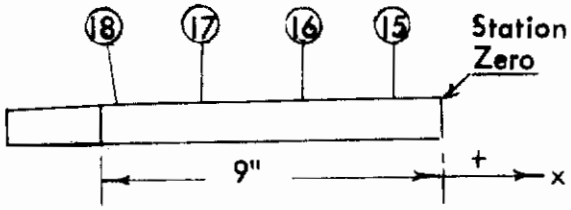

Circled numbers indicate static pressure tube numbers and chromel - alumel thermocouple numbers.

Static Pressure and Thermocouple Numbers	Station x Inches
15	-.5
16	-2.5
17	-4.5
18	-7.5

17" Generating Cylinder Instrumentation

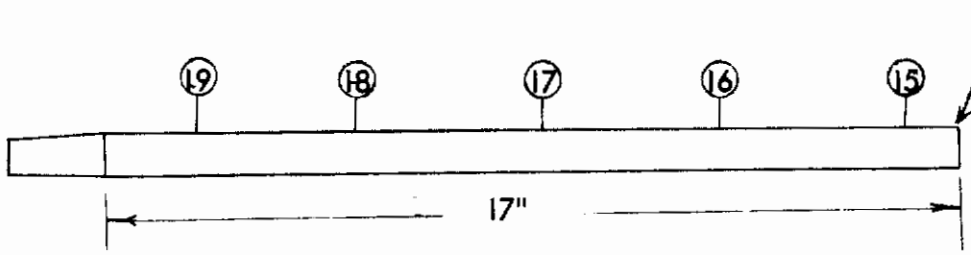

Circled numbers indicate static pressure tube numbers and chromel-alumel thermocouple numbers

Static Pressure and Thermocouple Numbers	Station x Inches
15	- .5
16	-3.5
17	-9.5
18	-12.
19	-14.5

FIGURE 10 NINE AND SEVENTEEN INCH CYLINDER INSTRUMENTATION

Numbers in triangles indicate presence of a static pressure tap and a differential thermocouple.

Numbers in circles indicate presence of a static pressure tap and an absolute thermocouple.

Note: Stations 5 and 13 are instrumented as follows:
(a) A static pressure tap every 90° on the circumference
(b) Three absolute thermocouples spaced 90° apart
(c) One differential thermocouple at top 0°.

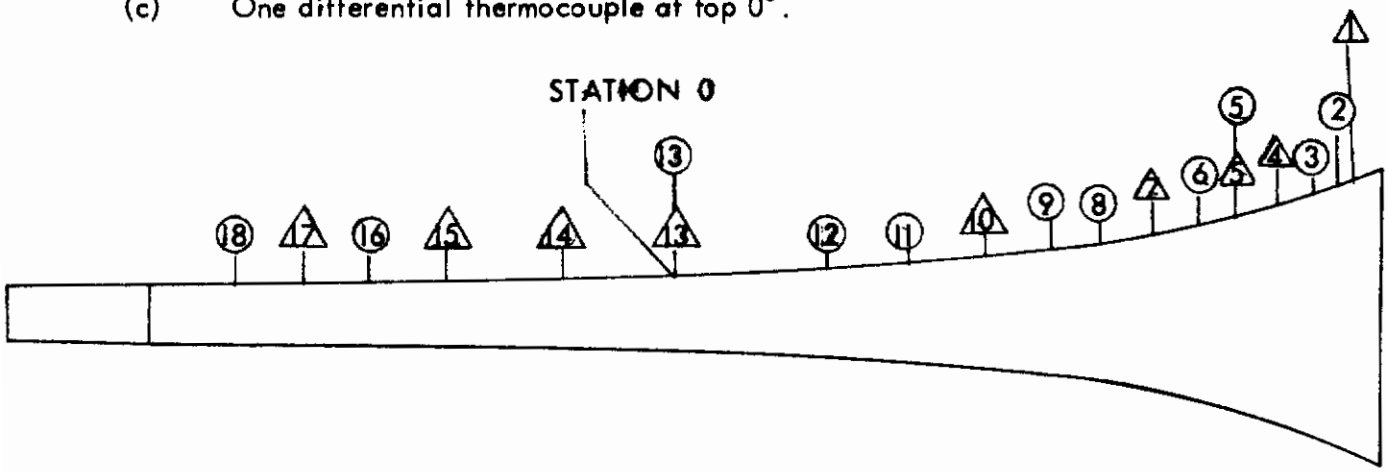

Station	X(Inches)	Press. Tap.	Abs. T/C	Diff. T/C
1	36.00	0°		0°
2	35.625	0°	0°	
3	35.25	0°	0°	
4	34.50	0°		0°
5	33.00	0°		0°
		90°	90°	
		180°	180°	
		270°	270°	
6	31.00	0°	0°	
7	29.00	0°		0°
8	27.00	0°	0°	
9	24.00	0°	0°	
10	18.75	0°		0°
11	12.75	0°	0°	
12	6.75	0°	0°	
13	0	0°		0°
		90°	90°	
		180°	180°	
		270°	270°	
14	-3.75	0°		0°
15	-7.50	0°		0°
16	-11.25	0°	0°	
17	-16.25	0°		0°
18	-21.25	0°	0°	

Note: 0° is TDC looking aft with all angles measured counterclockwise.

FIGURE 11 HEAT TRANSFER MACH 8 MODEL INSTRUMENTATION

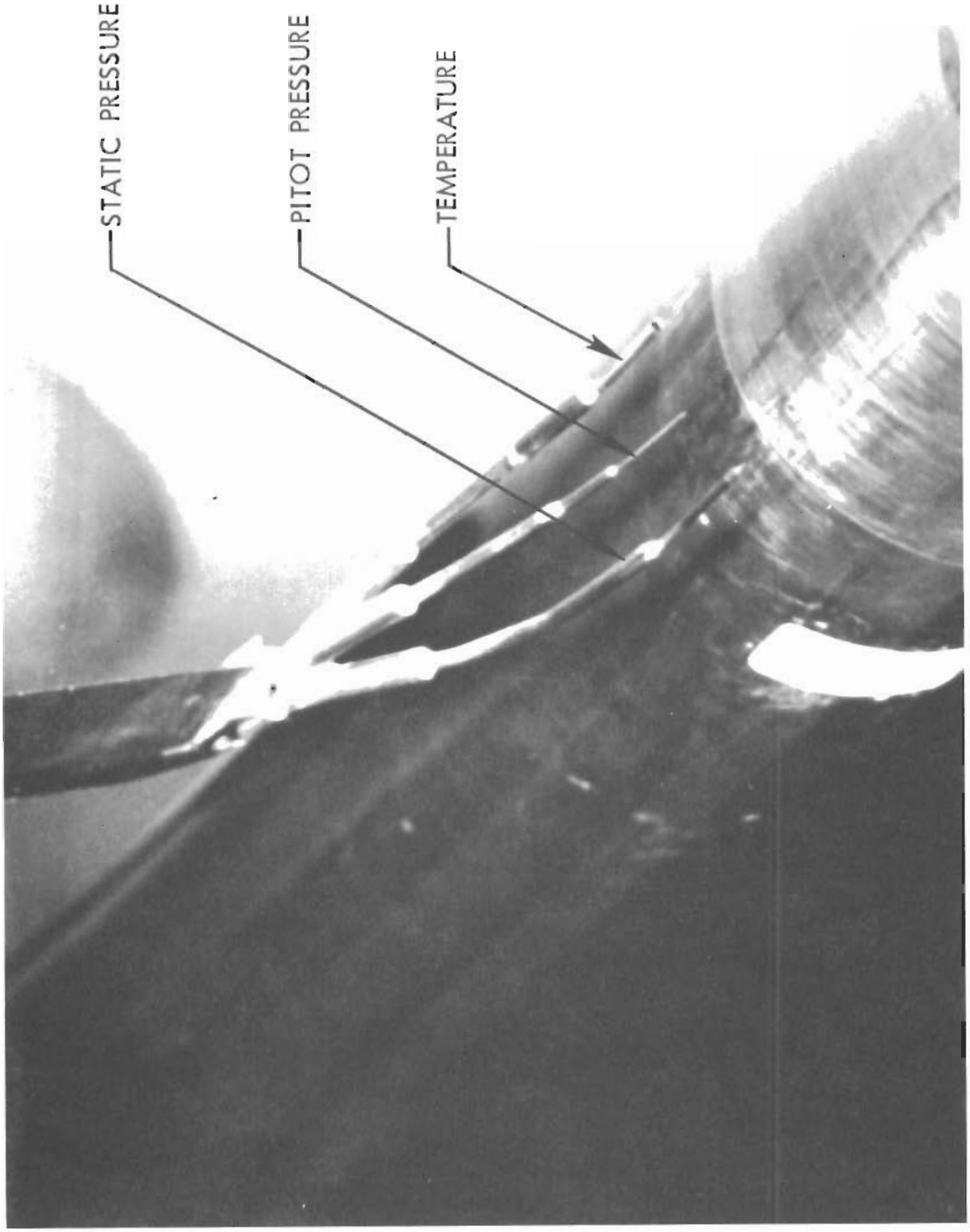

FIGURE 12. BOUNDARY LAYER SURVEY SYSTEM

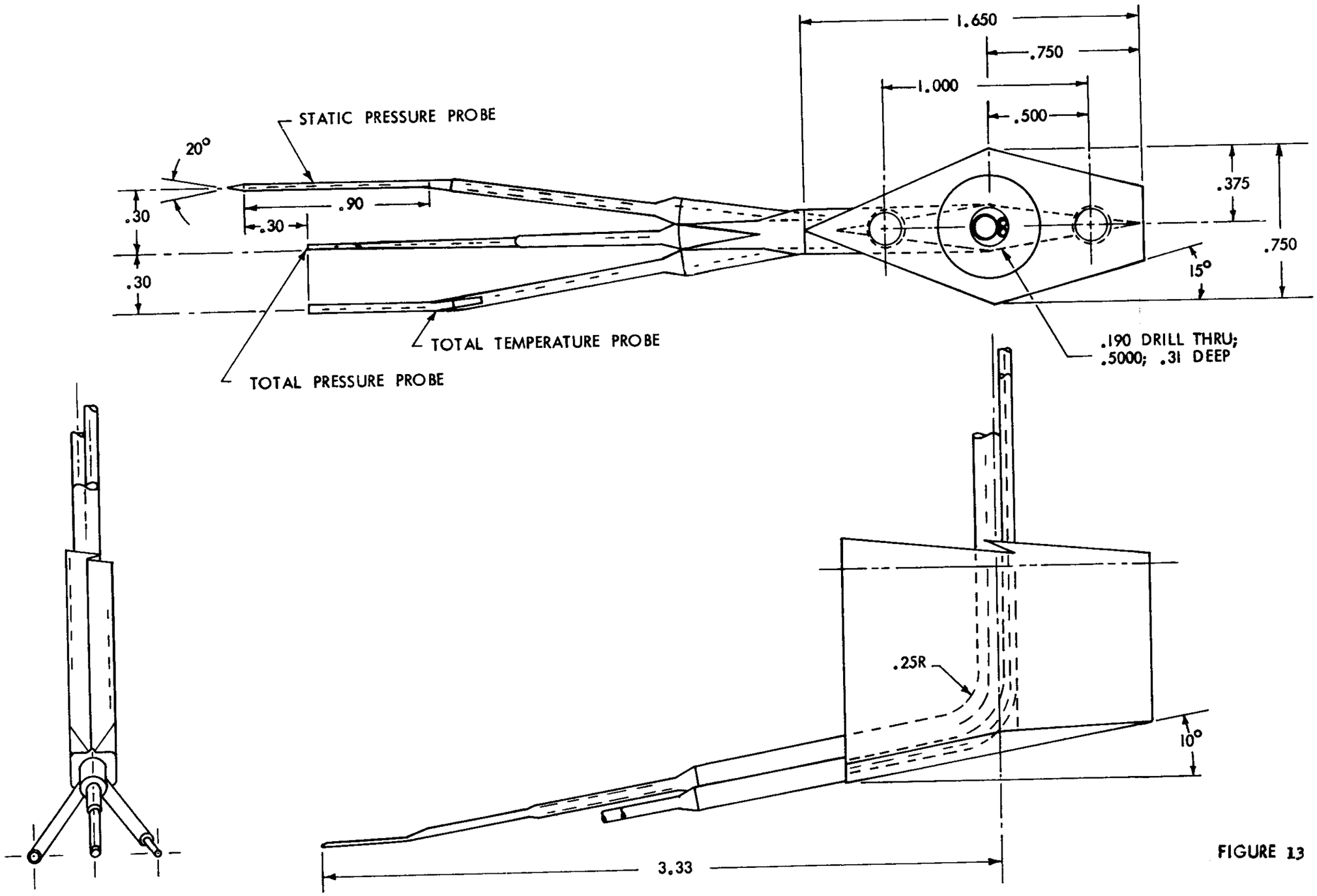

ALL DIMENSIONS
IN INCHES

FIGURE 13 DETAILS OF THREE - PRONG PROBE SYSTEM

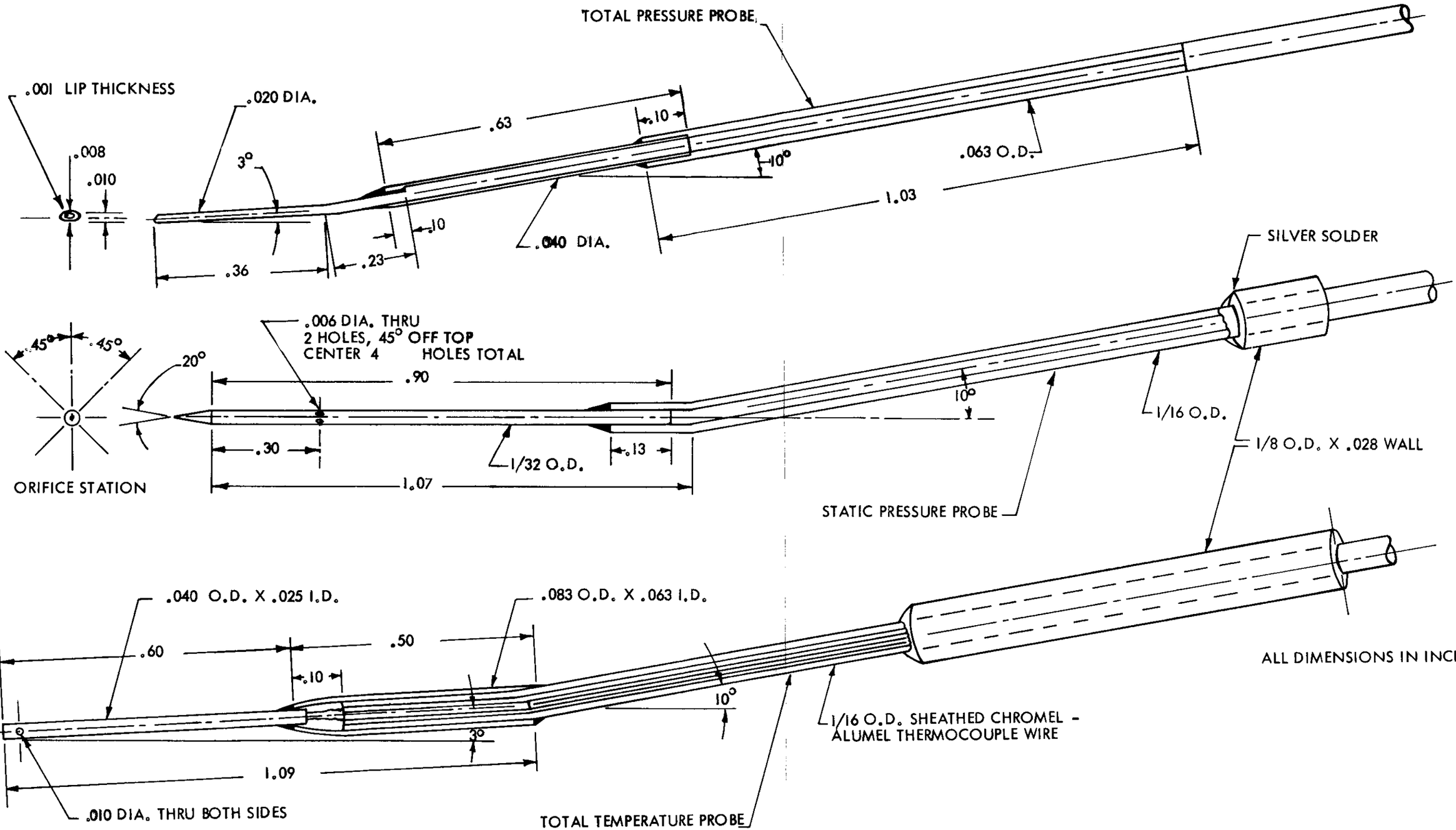

FIGURE 14 DETAILS OF BOUNDARY LAYER PROBES

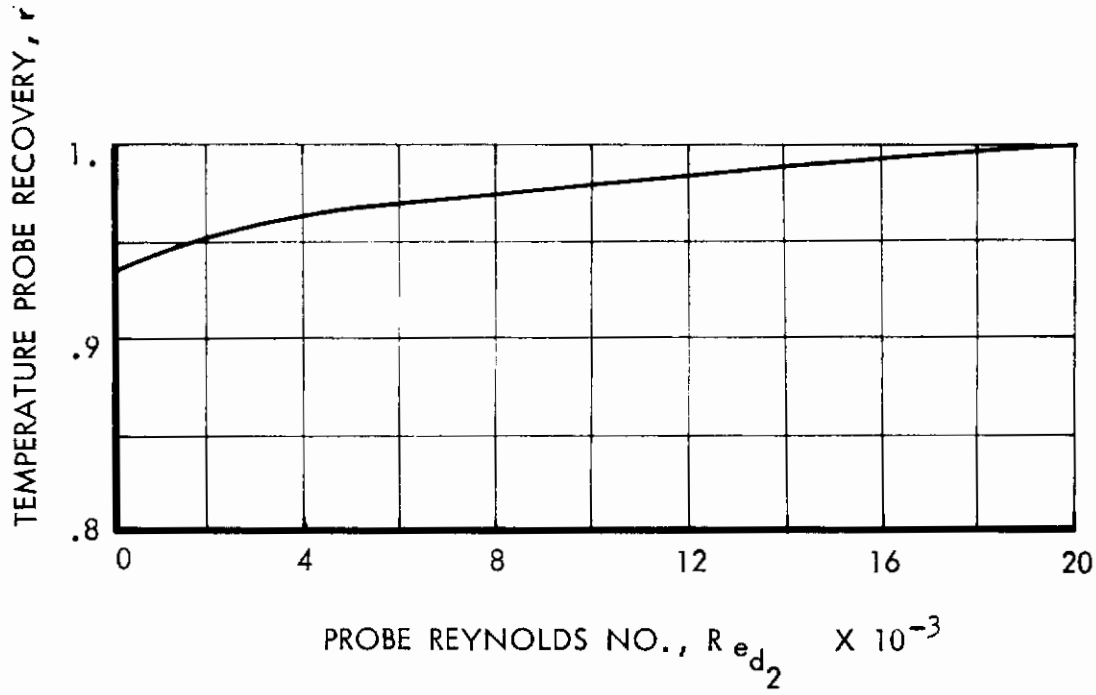

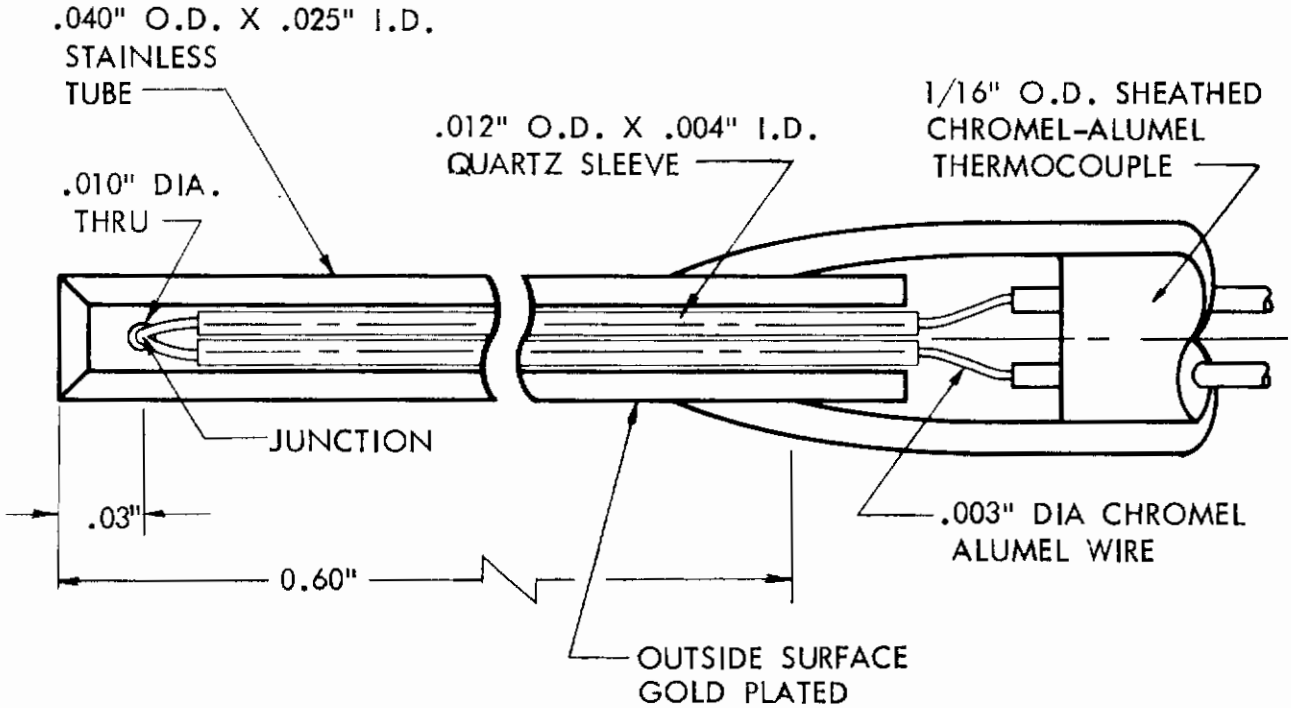

FIGURE 15 TOTAL TEMPERATURE PROBE CALIBRATION

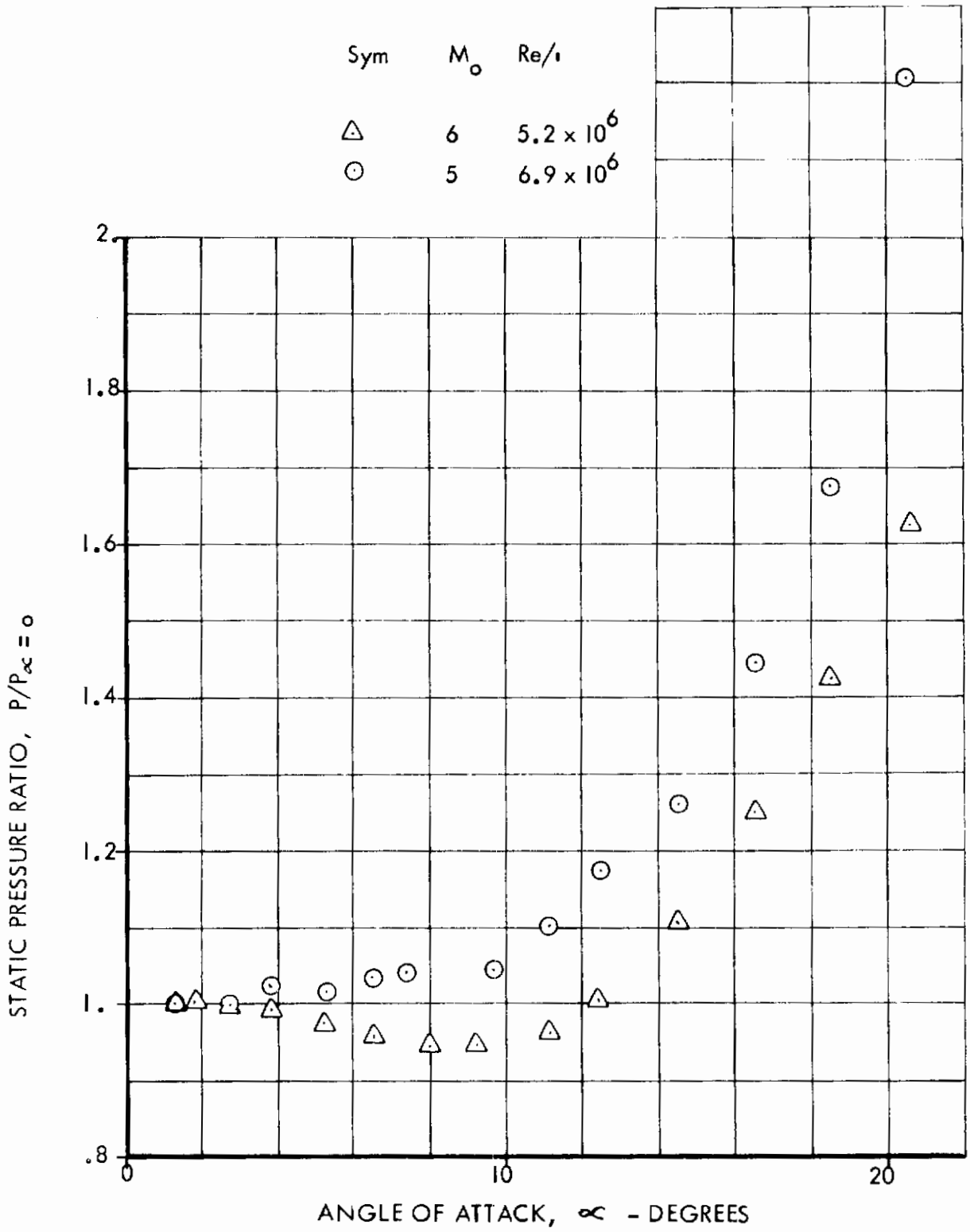

FIGURE 16 STATIC PROBE TESTS

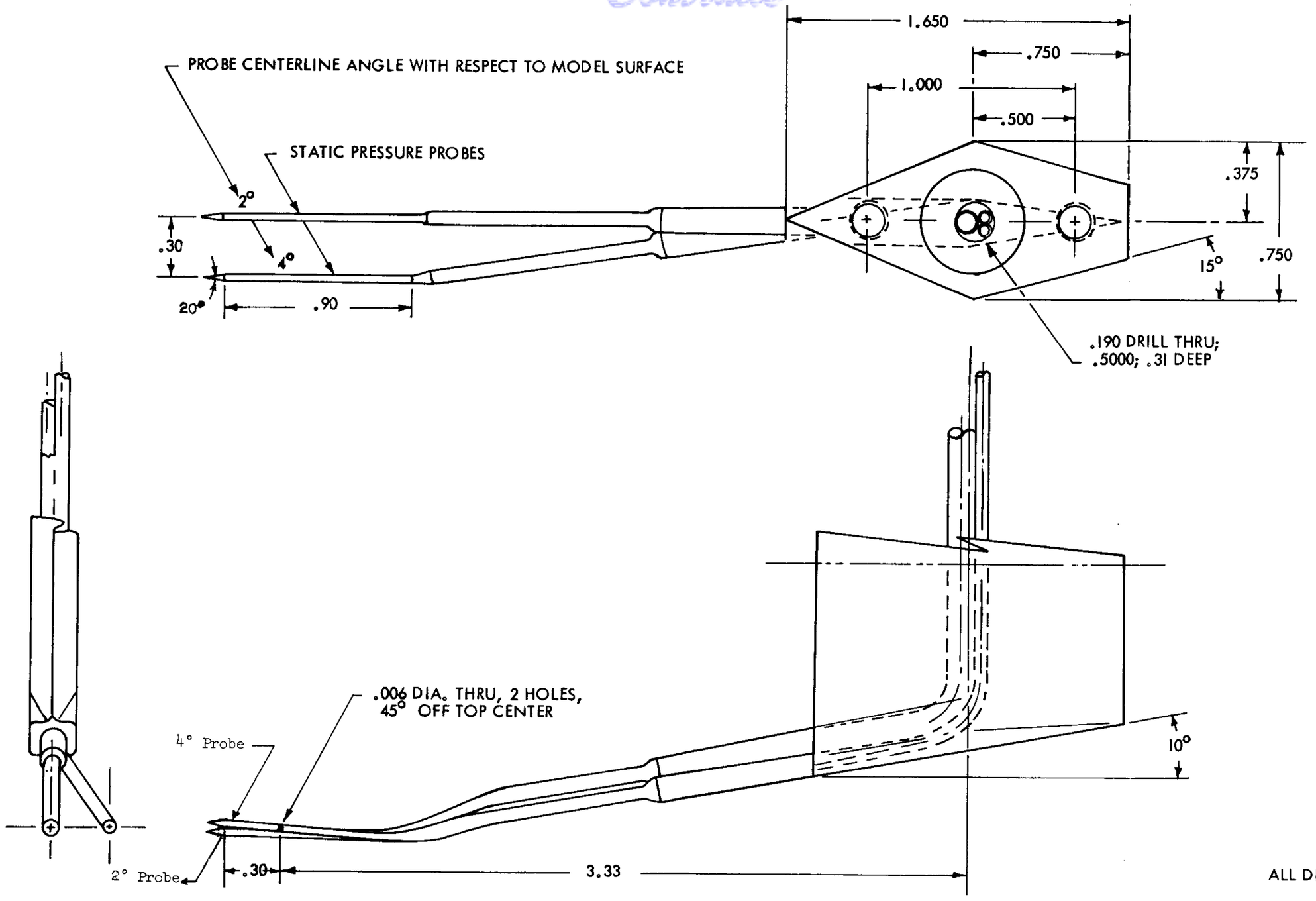

ALL DIMENSIONS IN INCHES

FIGURE 17 TWO PRONG STATIC RAKE

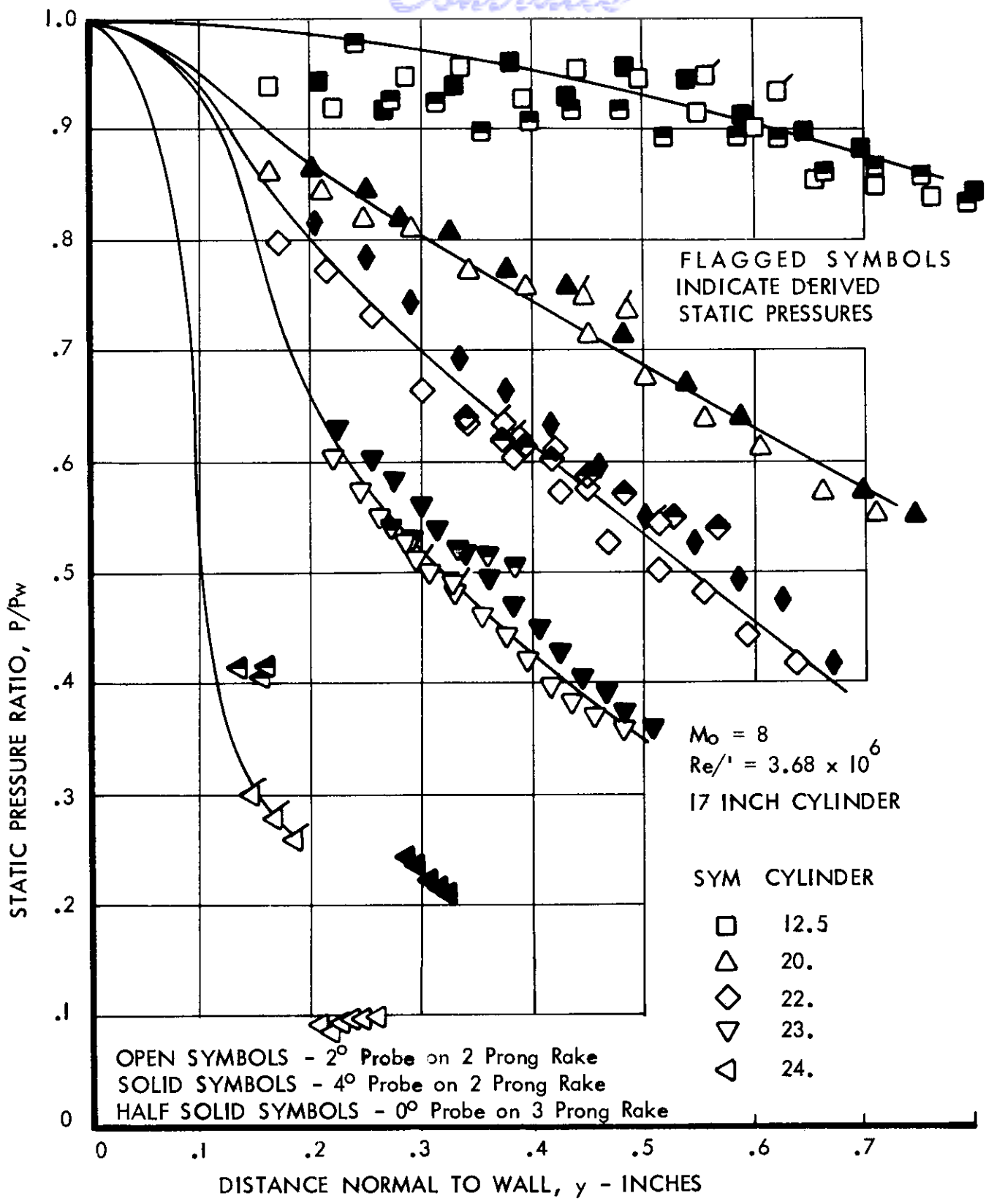

FIGURE 18. STATIC PRESSURE PROFILES ON MACH 10 MODEL

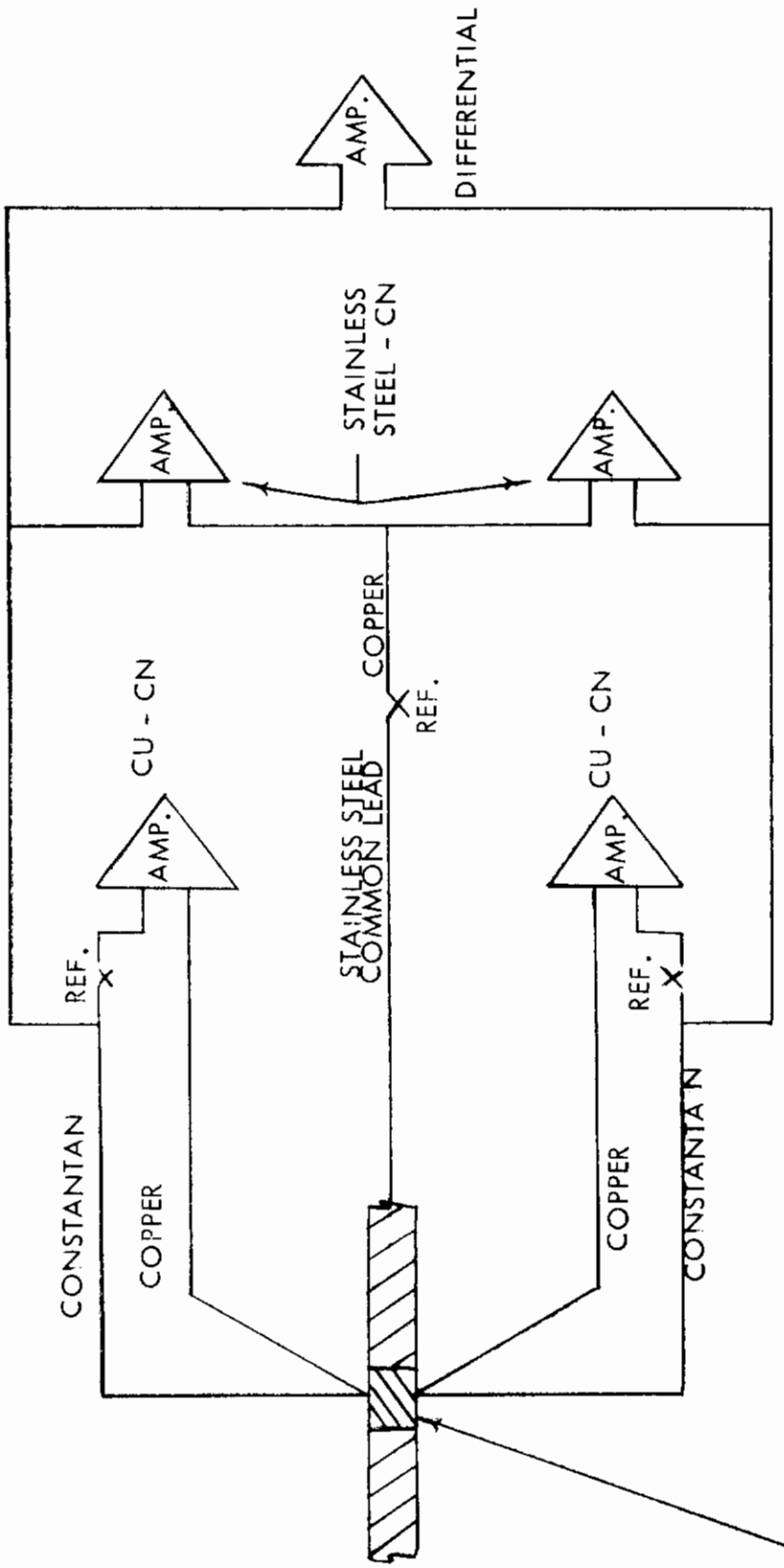

FIGURE 19 TYPICAL HEAT TRANSFER PLUG HOOK-UP

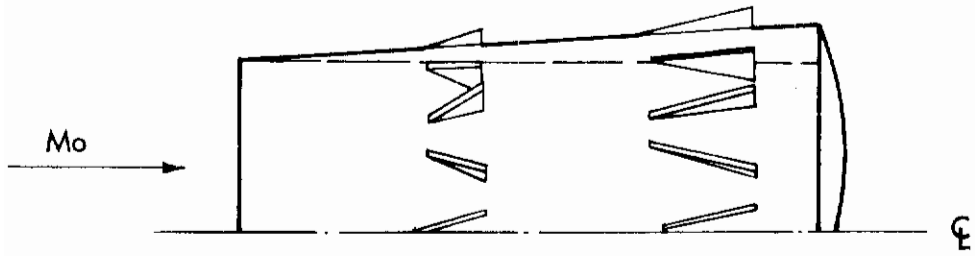

VORTEX GENERATORS

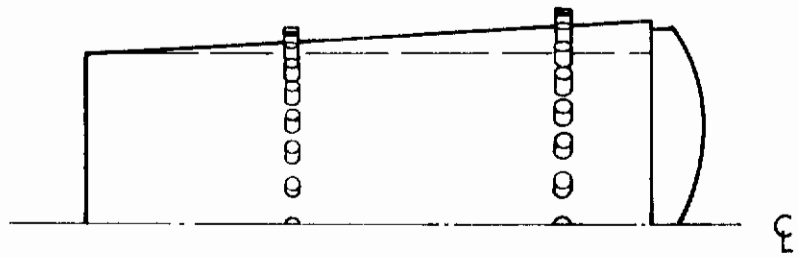

WIRE TRIPS

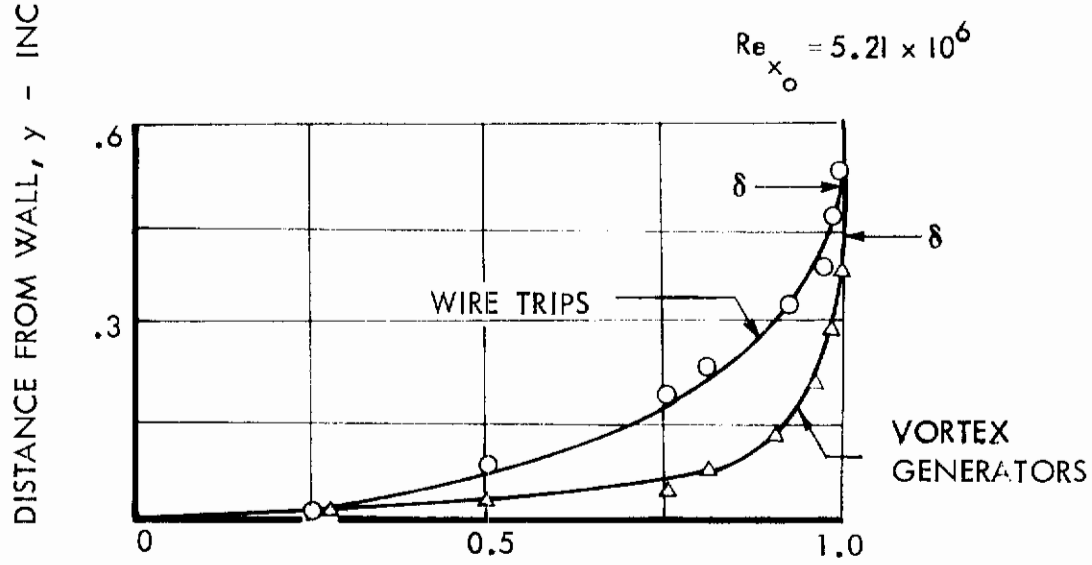

FIGURE 20 TRANSITION DEVICES AND RESULTS, $M_o = 8$

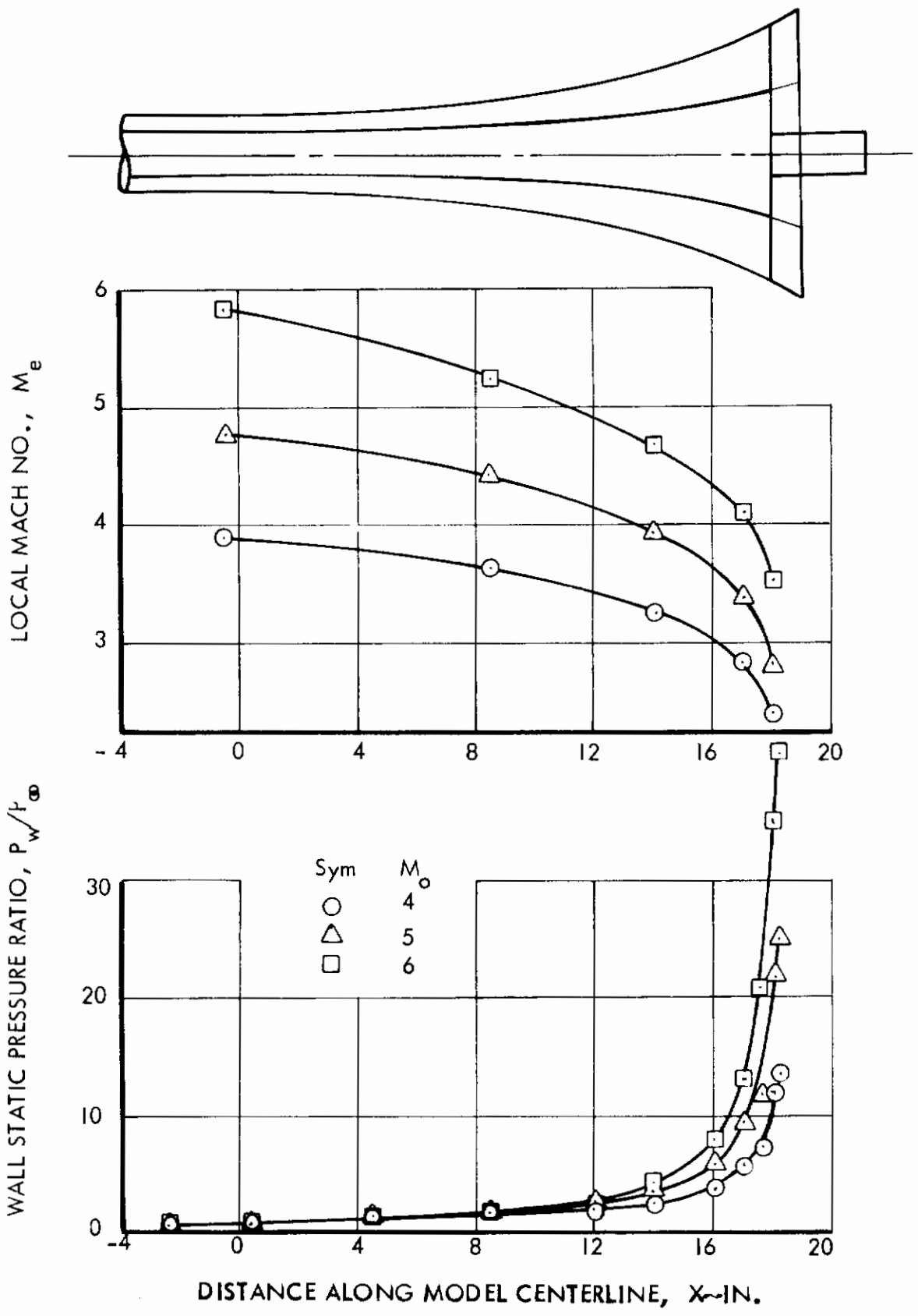

FIGURE 21 MACH NUMBER AND PRESSURE DISTRIBUTION ON MACH 5 MODEL

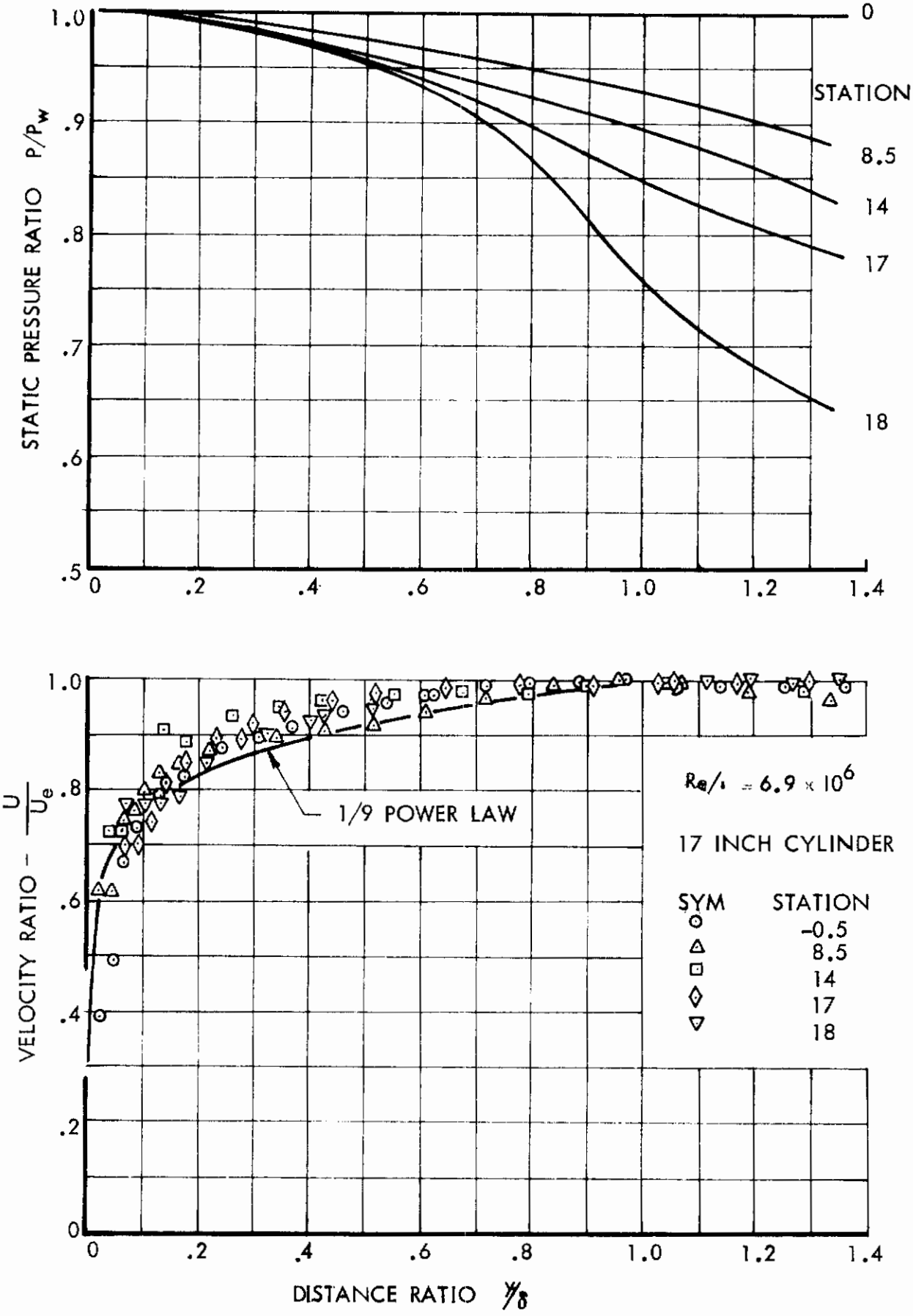

FIGURE 22 VELOCITY AND STATIC PRESSURE PROFILES ON MACH 5 MODEL, $M_o = 5$

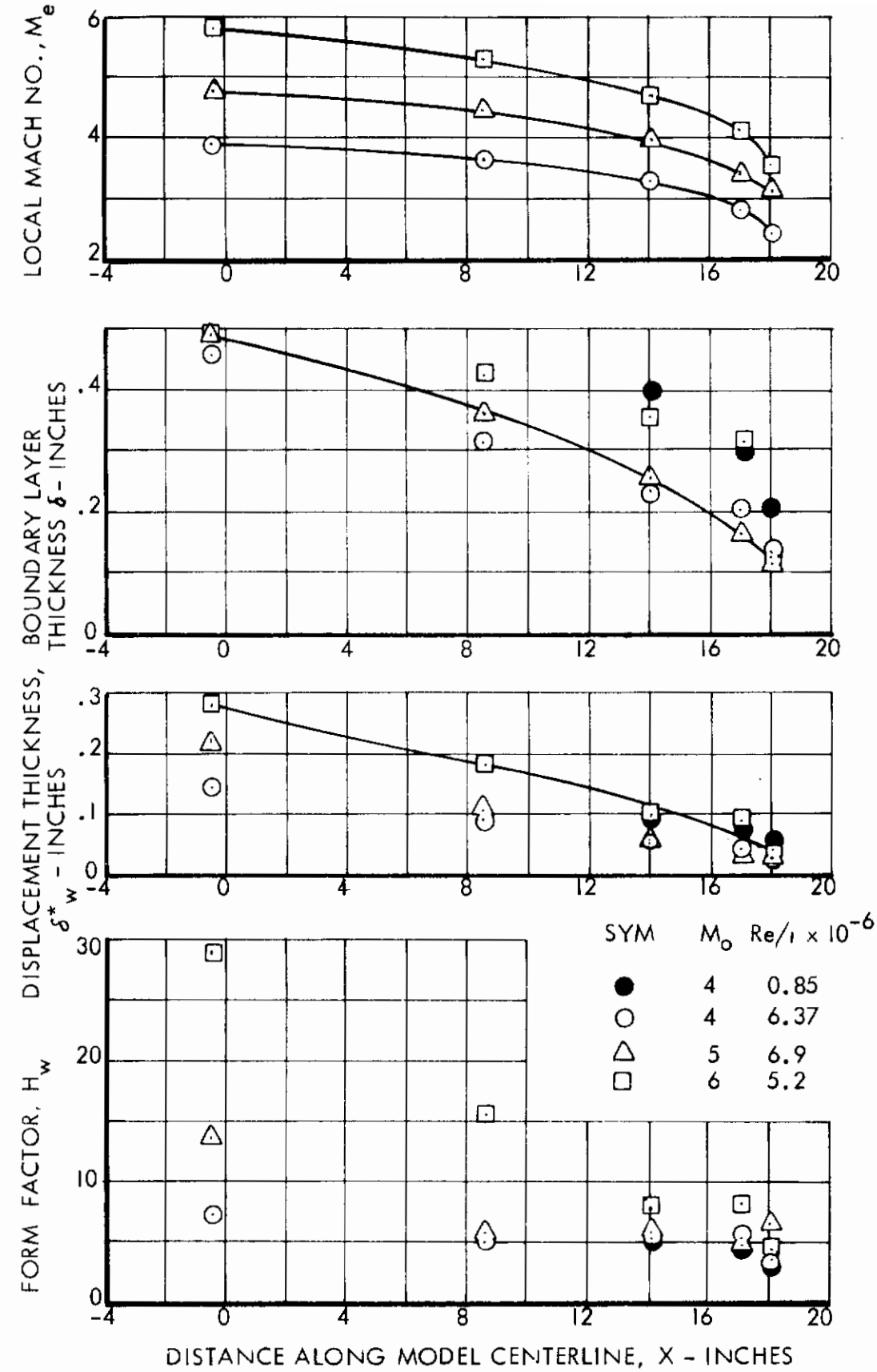

FIGURE 23 BOUNDARY LAYER CHARACTERISTICS ALONG MACH 5 MODEL, 17 INCH CYLINDER

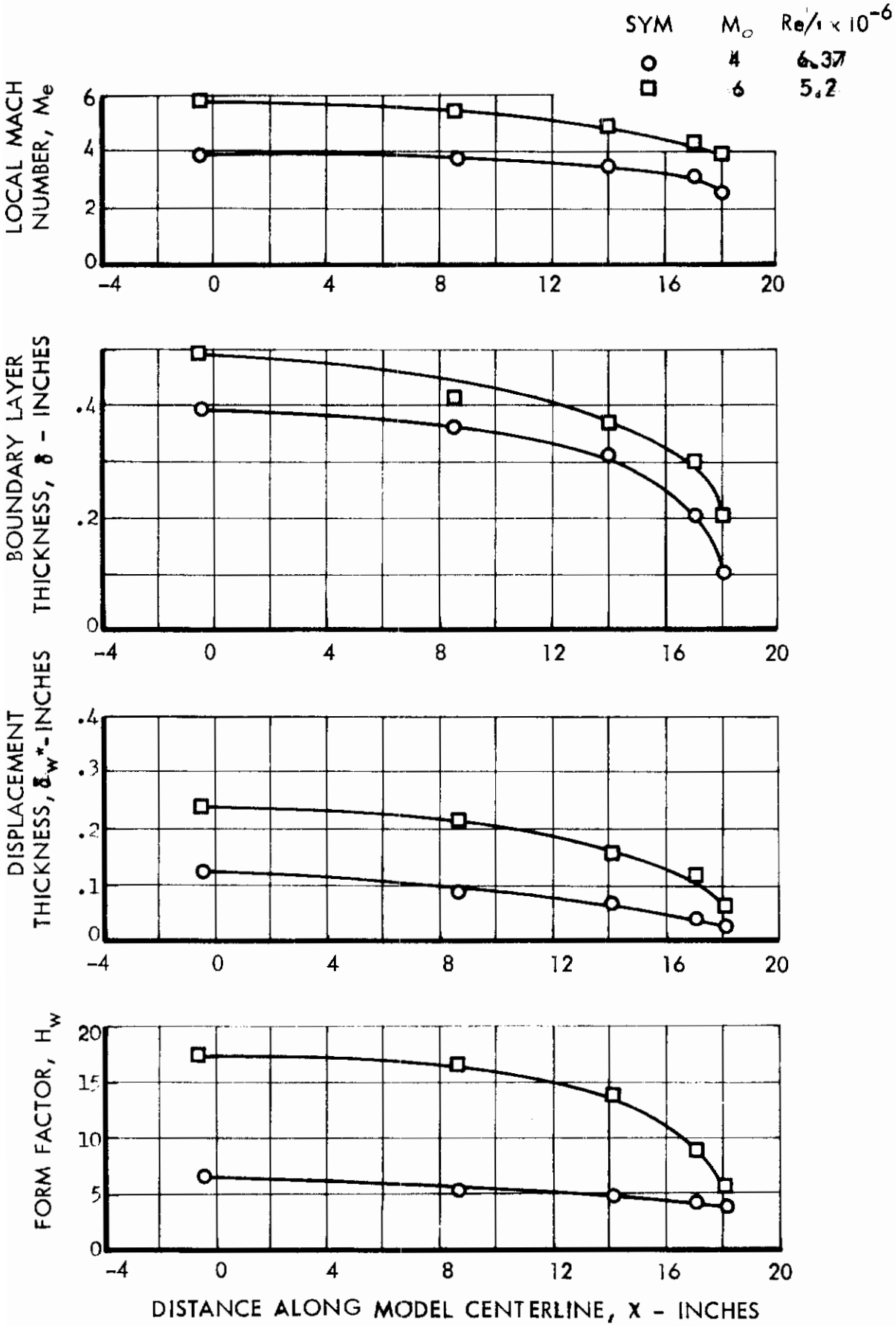

FIGURE 24 BOUNDARY LAYER CHARACTERISTICS ALONG MACH 6 MODEL, 17 INCH CYLINDER

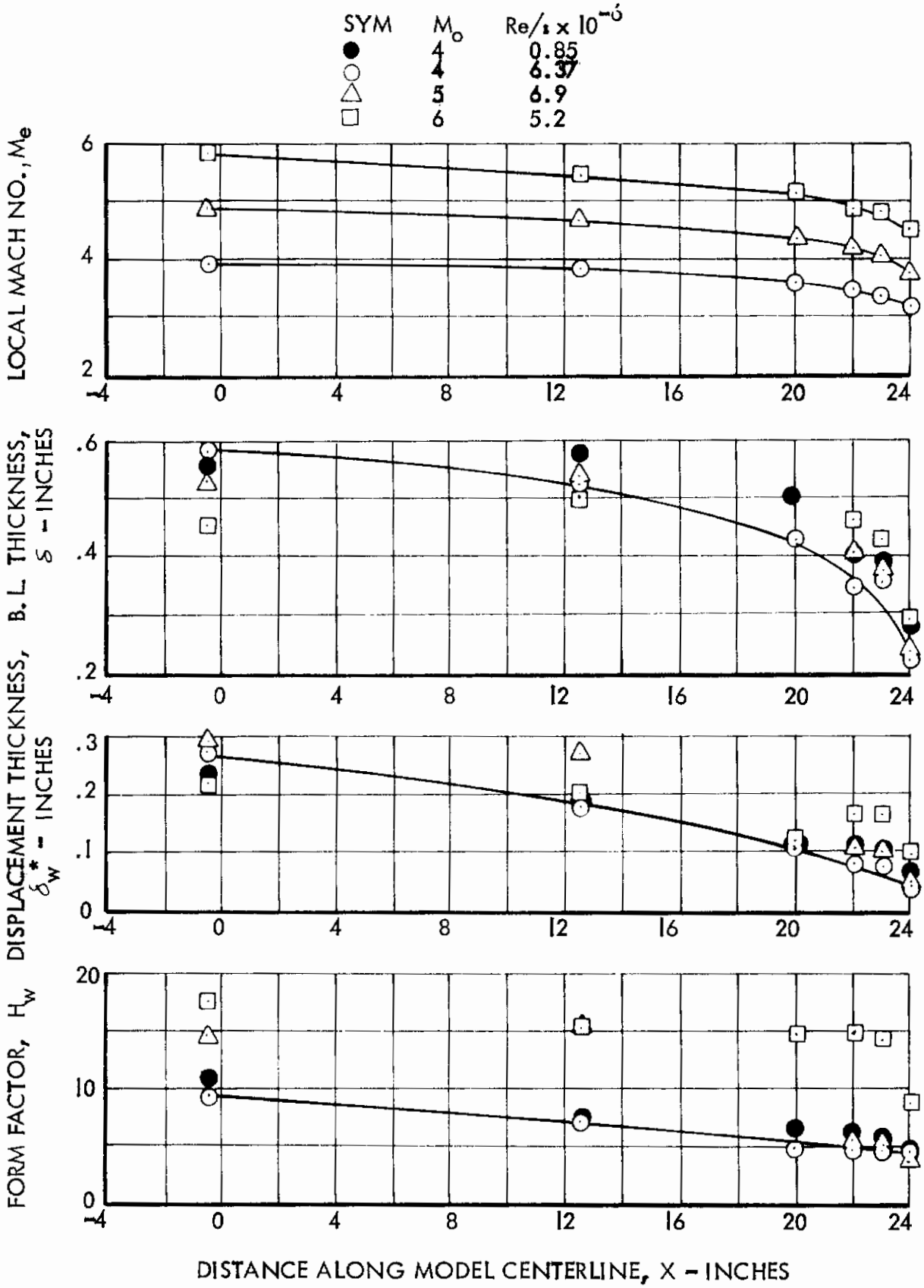

FIGURE 25 BOUNDARY LAYER CHARACTERISTICS ALONG MACH 10 MODEL, 17 INCH CYLINDER

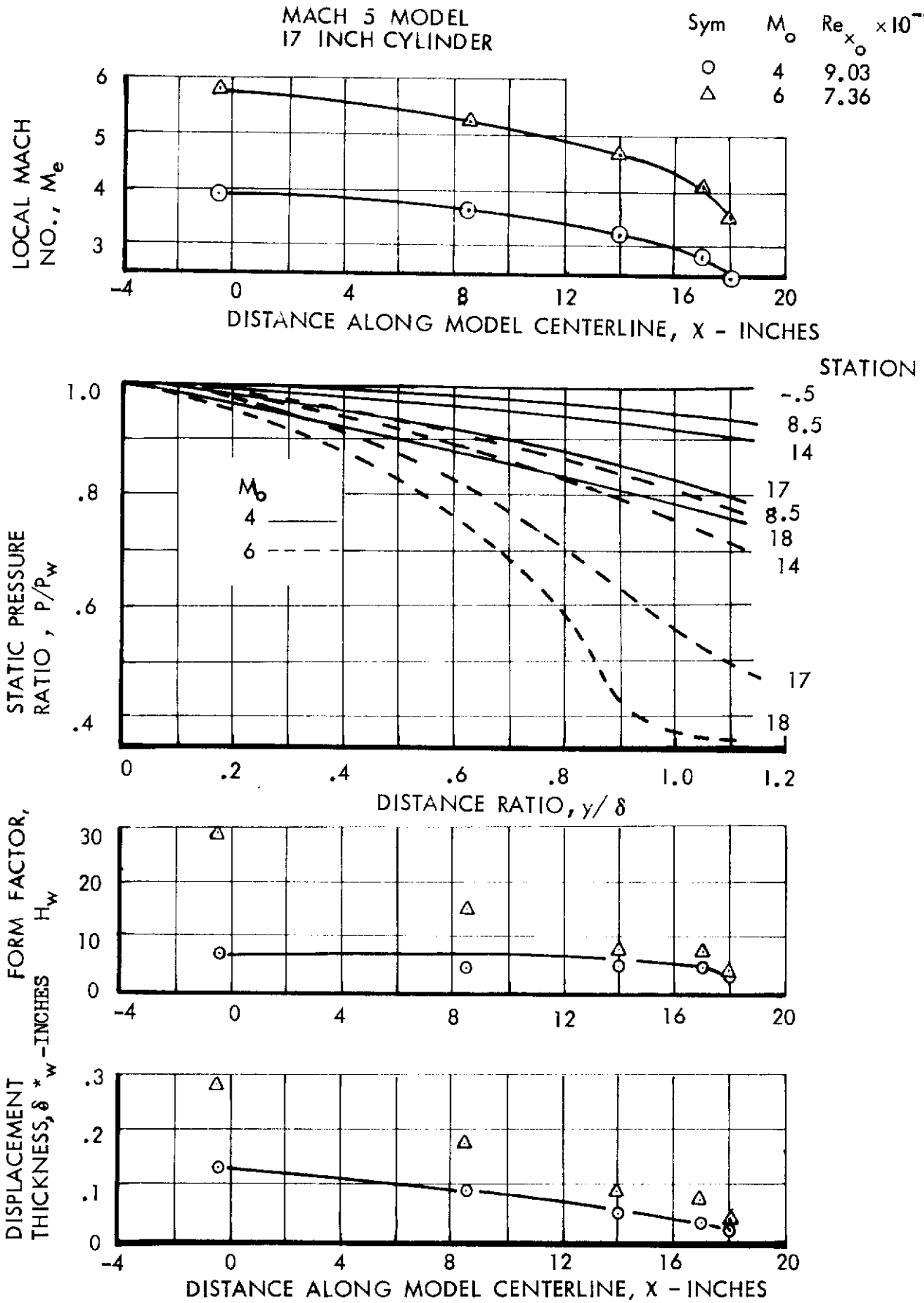

FIGURE 26 EFFECT OF MACH NUMBER ON BOUNDARY LAYER CHARACTERISTICS

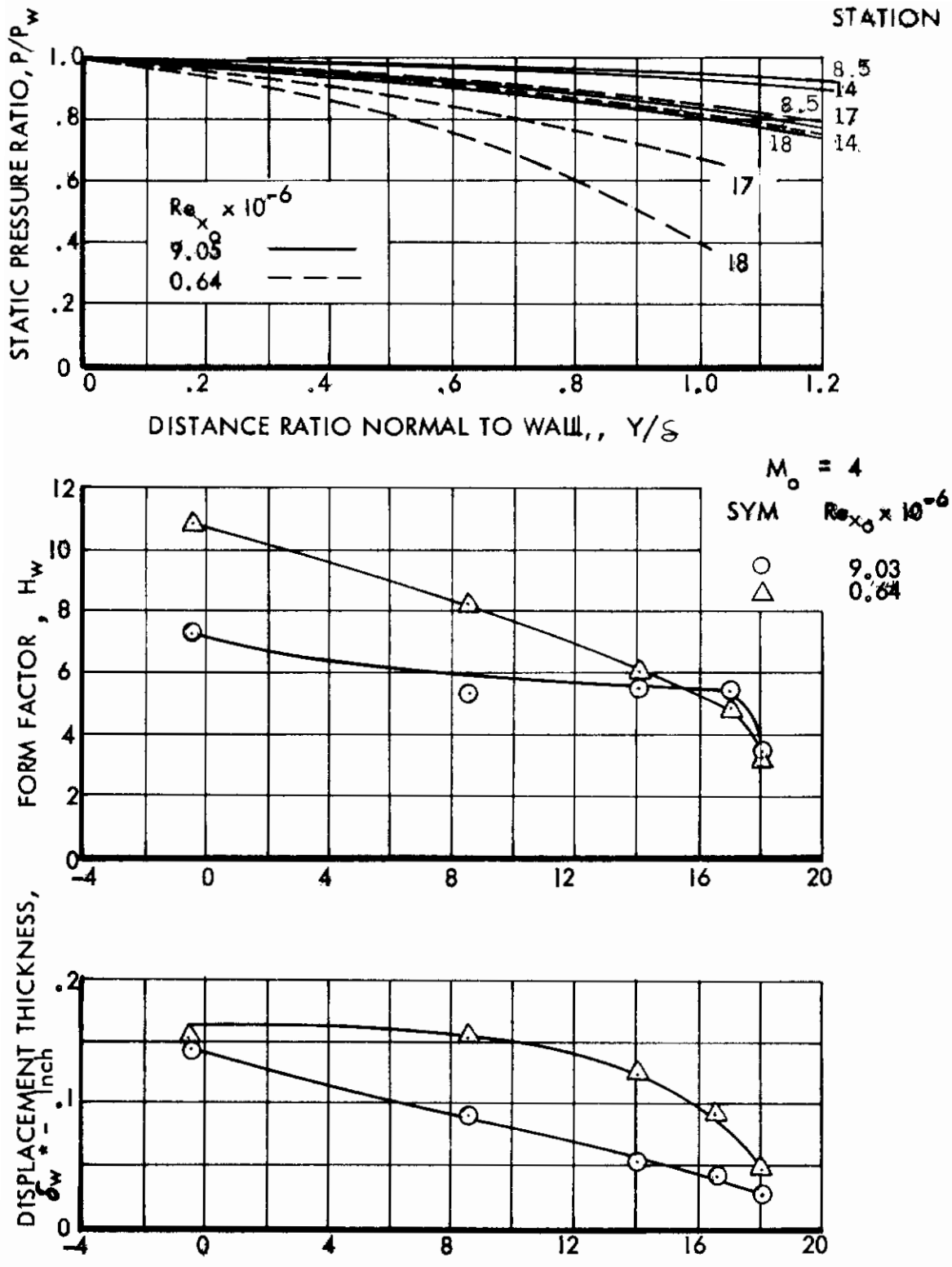

FIGURE 27 EFFECT OF REYNOLDS NUMBER ON BOUNDARY LAYER CHARACTERISTICS

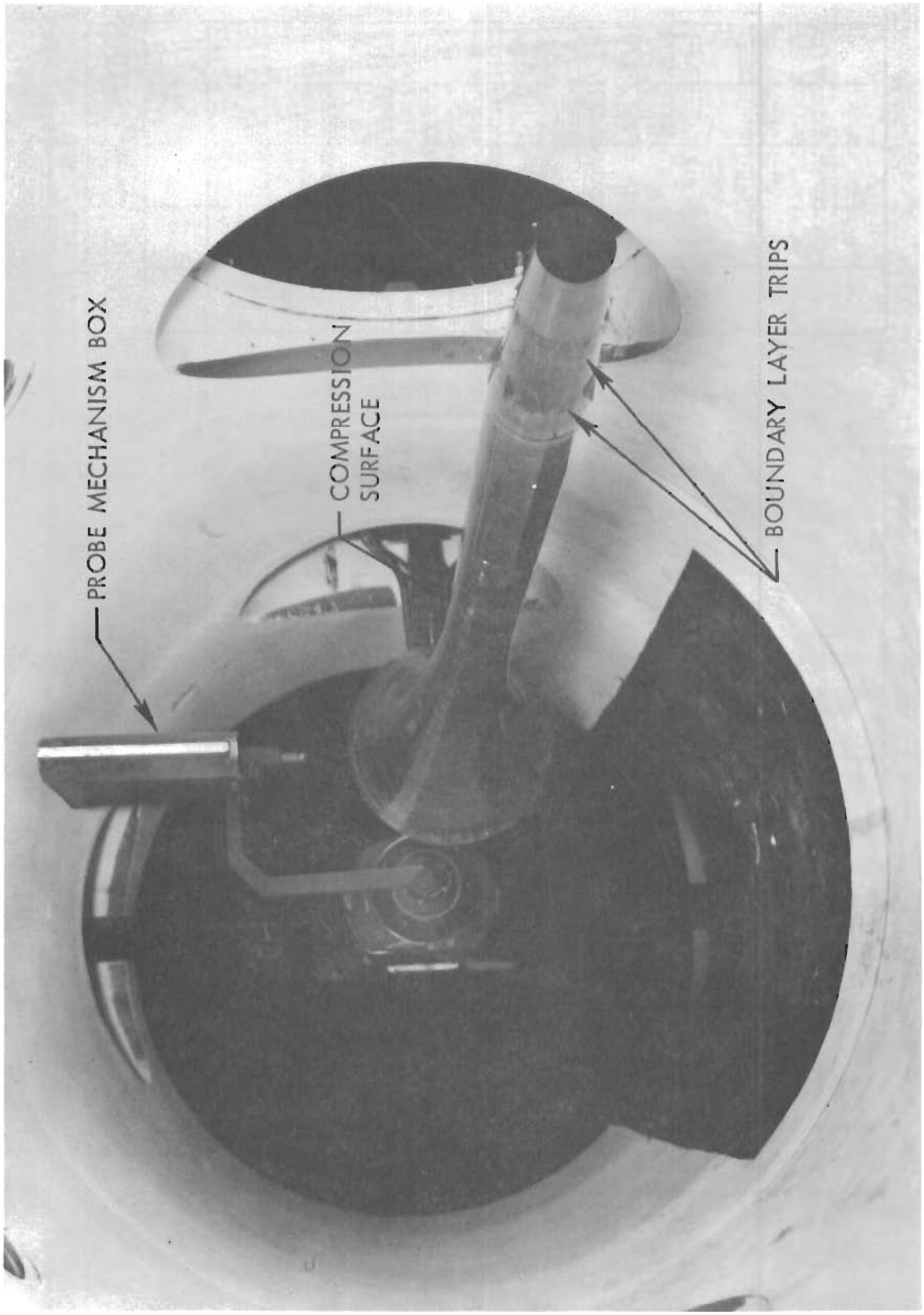

FIGURE 28. HEAT TRANSFER MACH 8 MODEL IN AEDC TUNNEL B

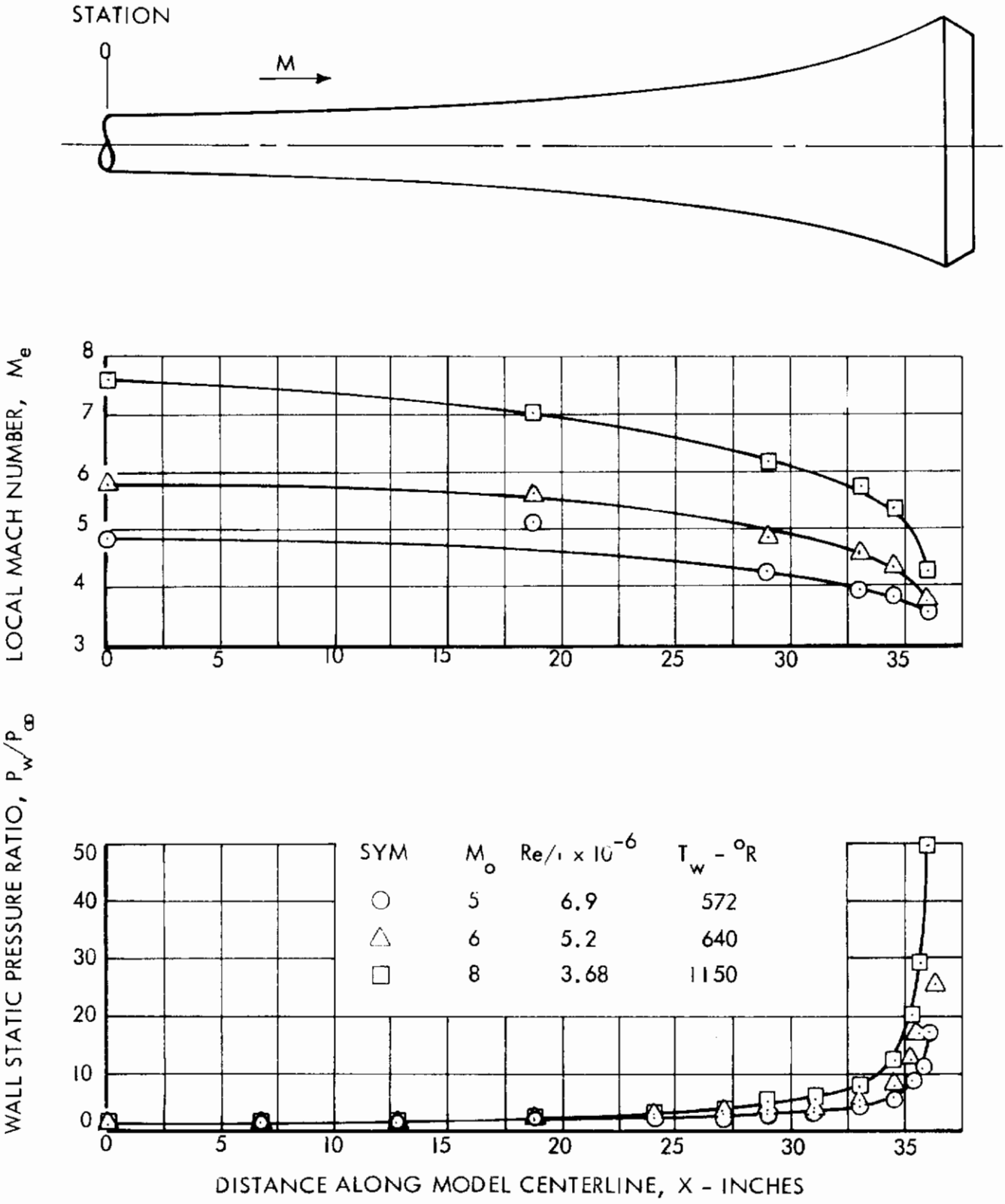

FIGURE 29 MACH NUMBER AND PRESSURE DISTRIBUTION ON HEAT TRANSFER MACH 8 MODEL

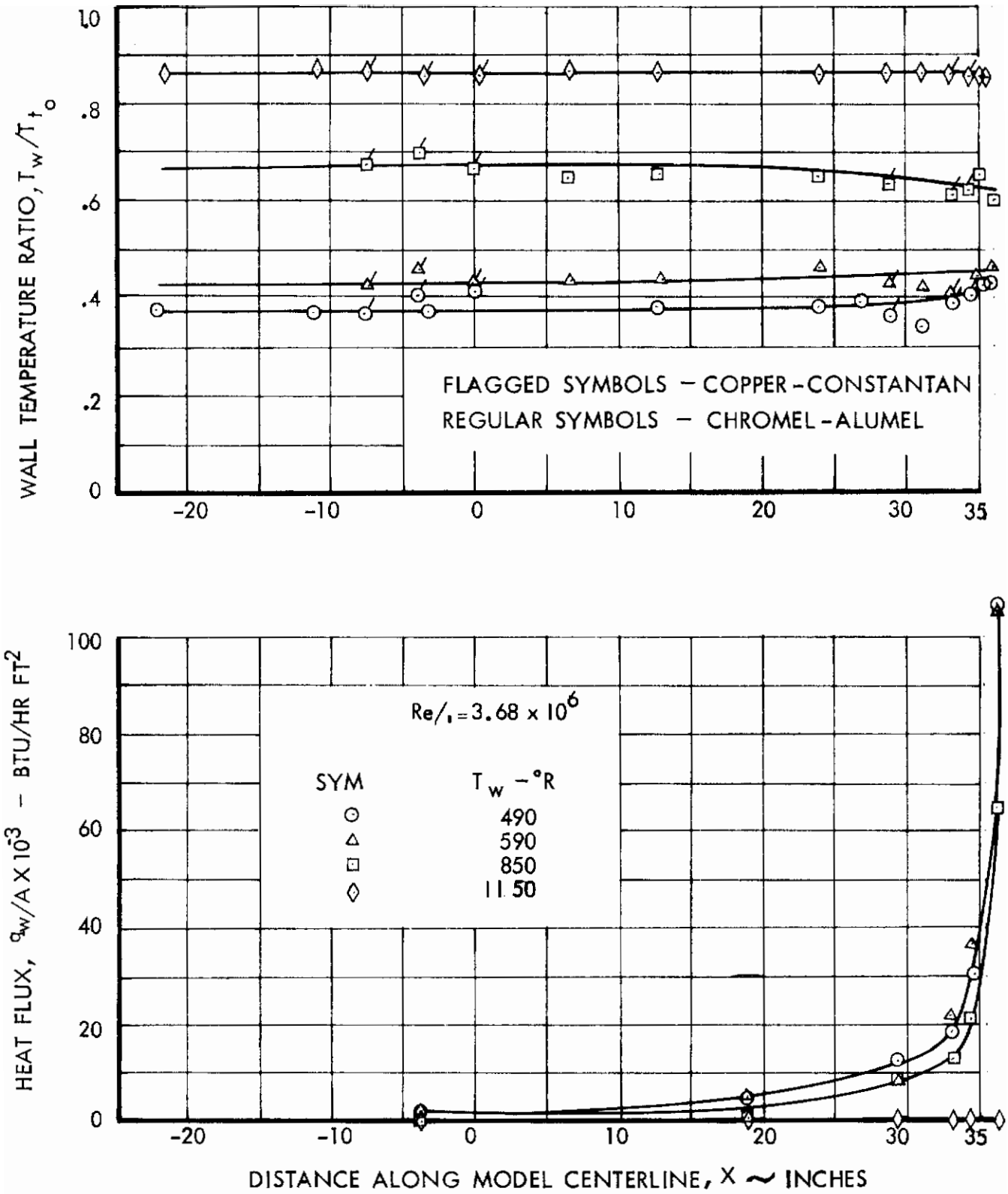

FIGURE 30 WALL TEMPERATURE AND HEAT FLUX DISTRIBUTION ALONG HEAT TRANSFER MACH 8 MODEL, $M_o = 8$

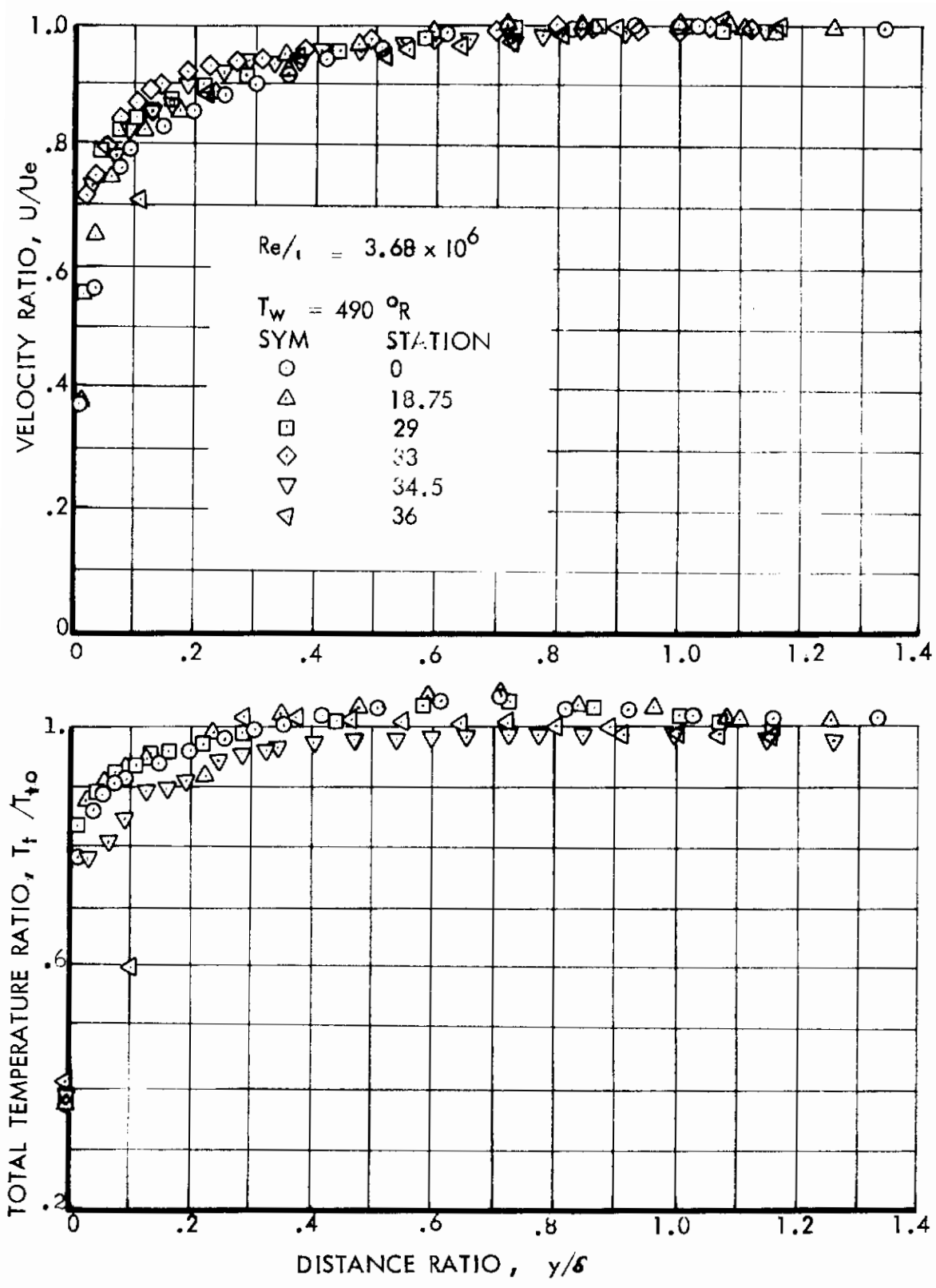

FIGURE 31 VELOCITY AND TEMPERATURE PROFILES ON THE HEAT TRANSFER MACH 8 MODEL, Mo = 8

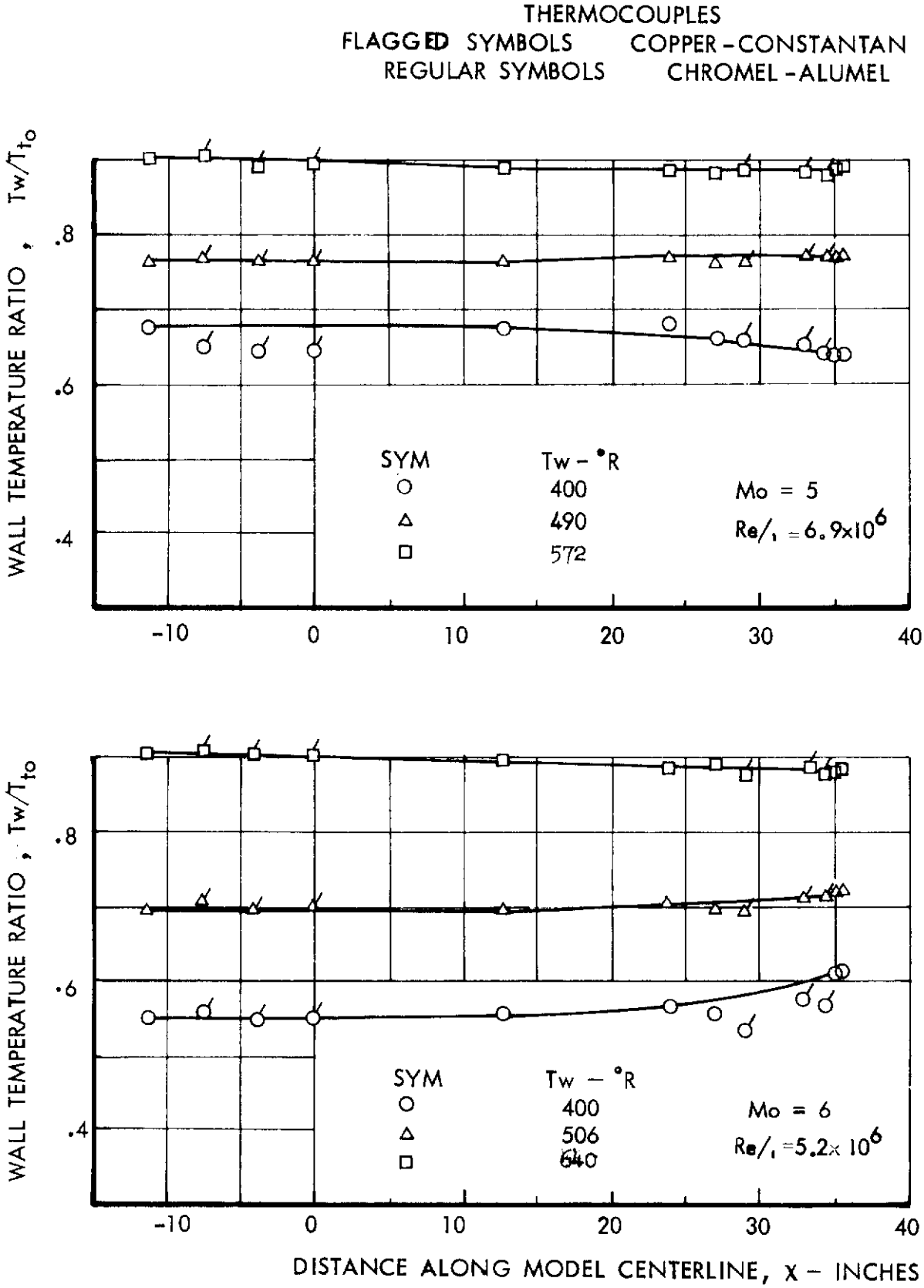

FIGURE 32. WALL TEMPERATURE DISTRIBUTION ALONG HEAT TRANSFER MODEL, Mo = 5,6 | MACH 8

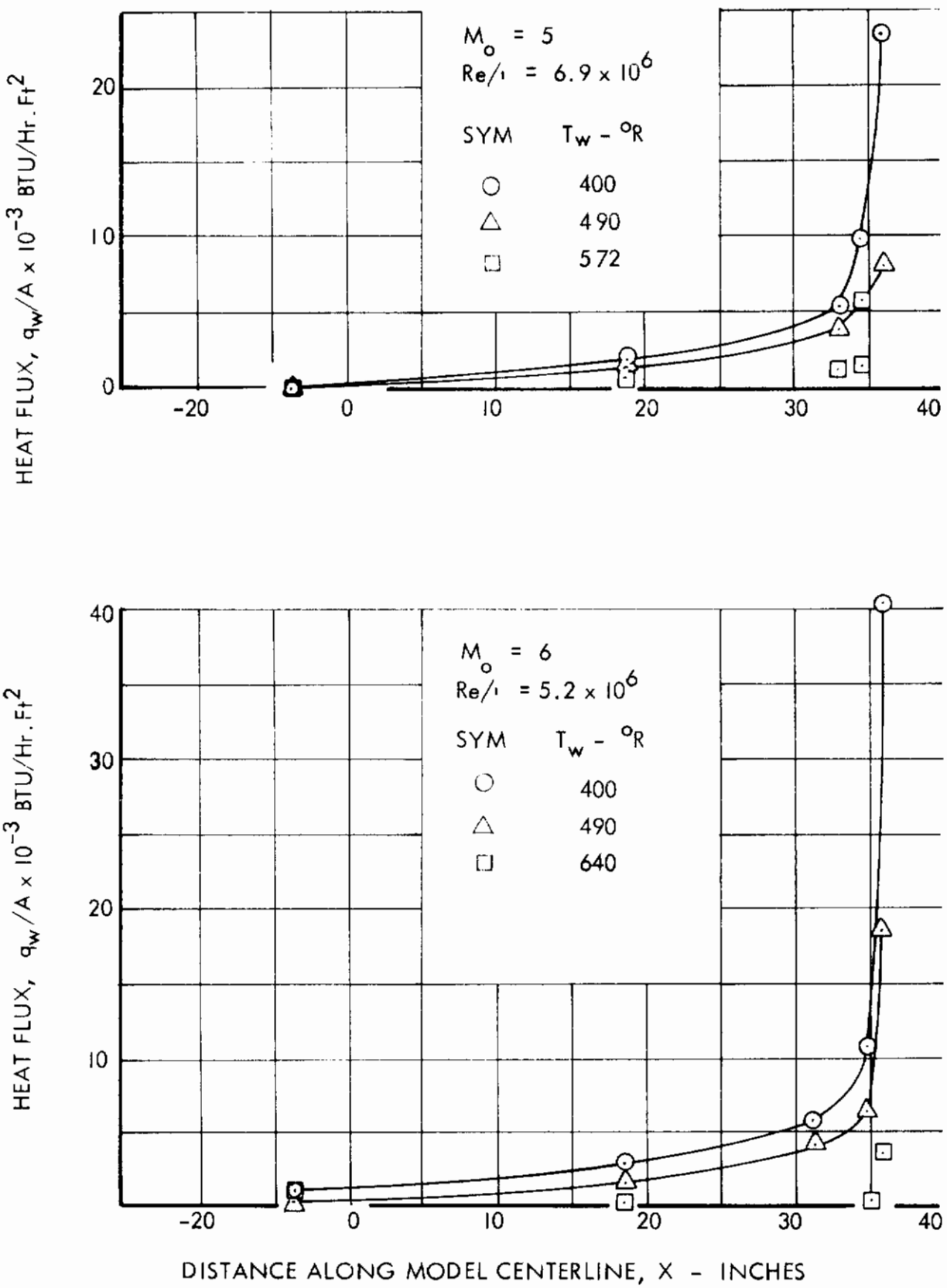

FIGURE 33 HEAT FLUX DISTRIBUTION ALONG HEAT TRANSFER MACH 8 MODEL., M_o = 5, 6

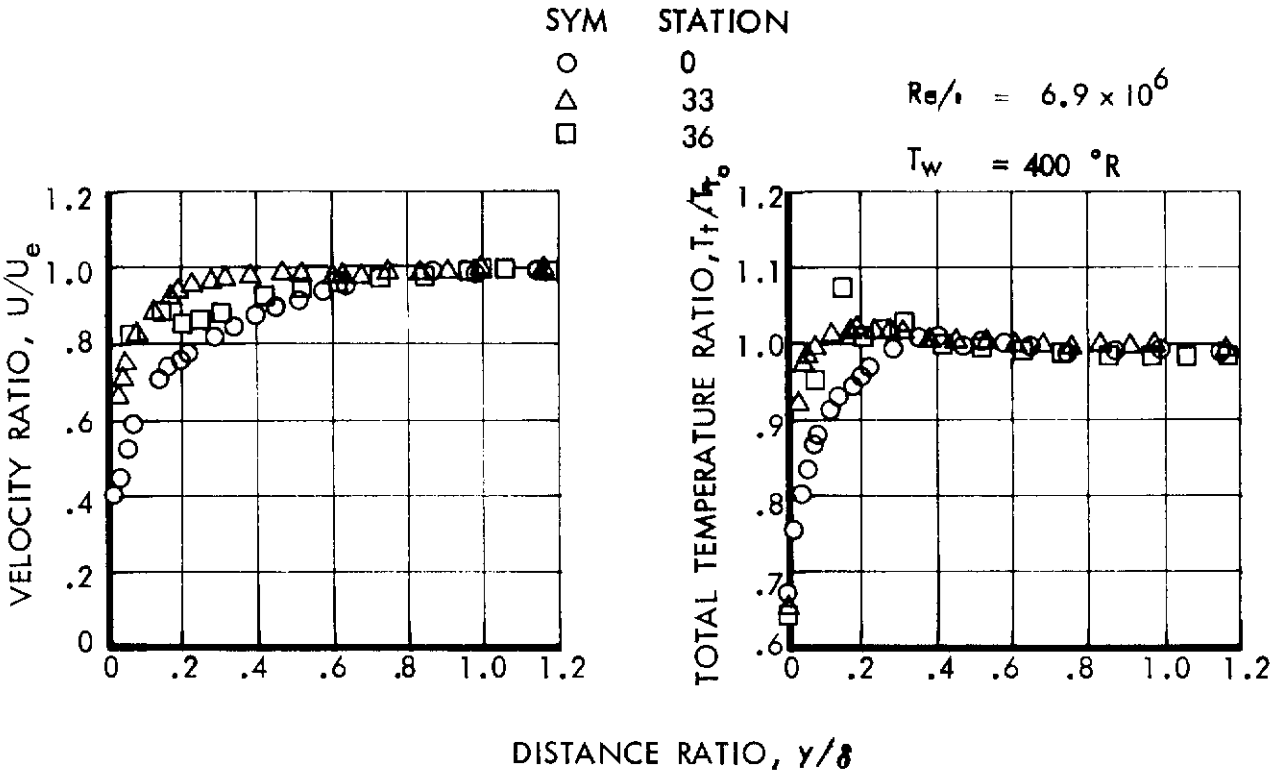

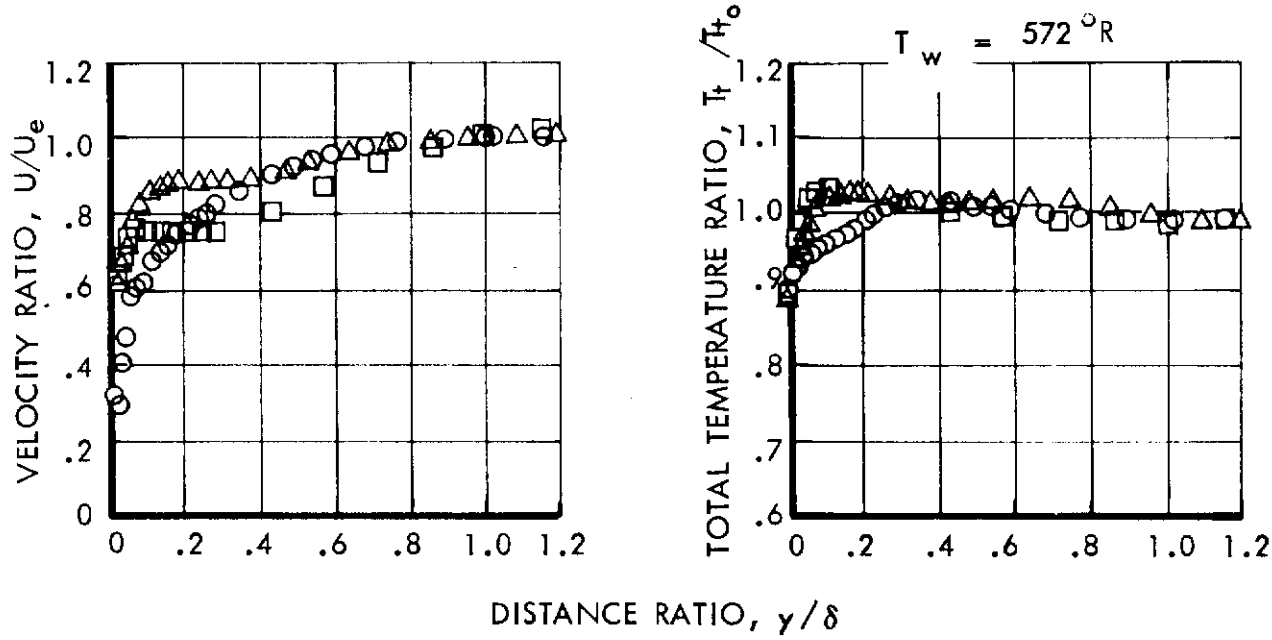

FIGURE 34 VELOCITY AND TOTAL TEMPERATURE PROFILES ON HEAT TRANSFER MACH 8 MODEL, $M_o = 5$

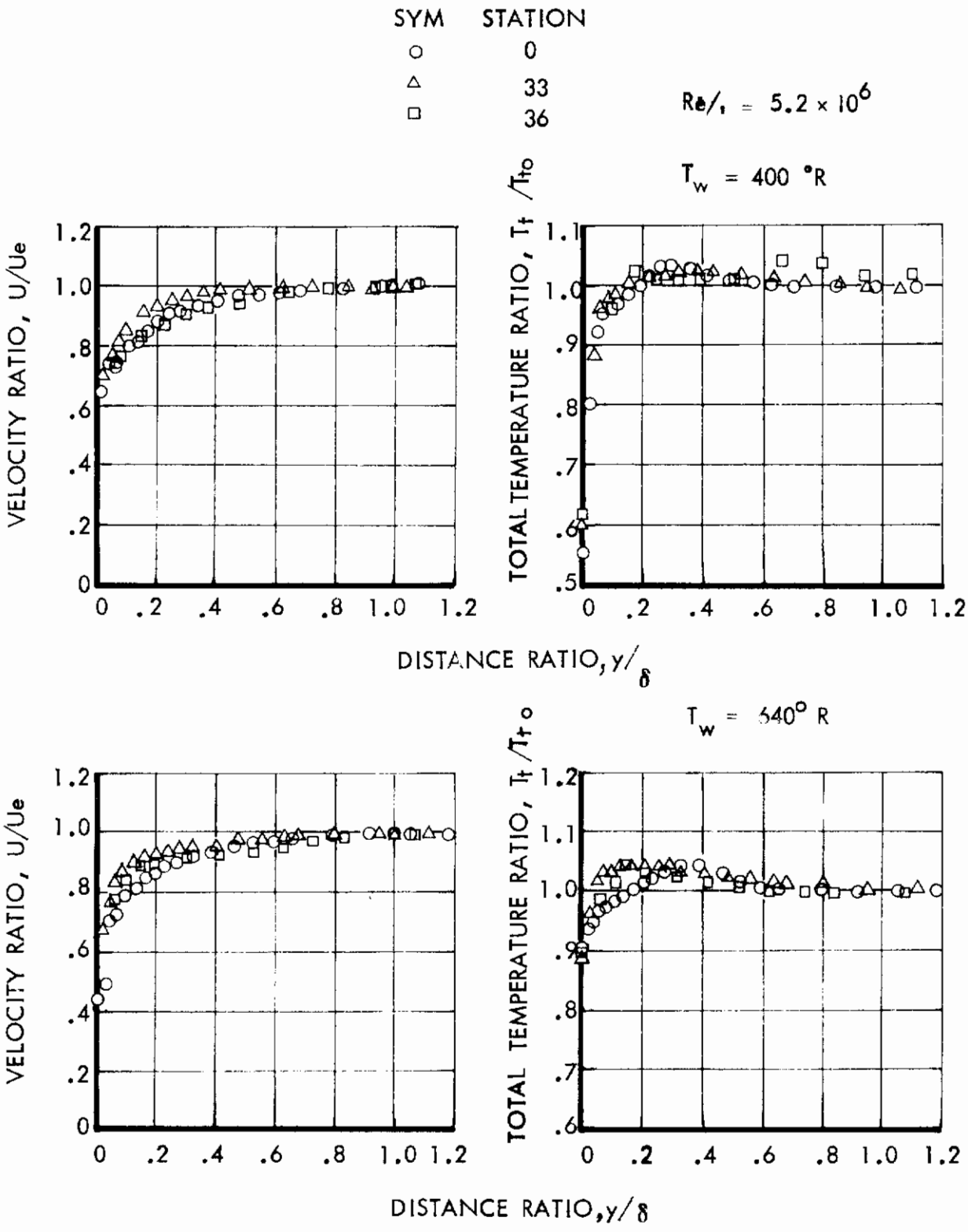

FIGURE 35 VELOCITY AND TOTAL TEMPERATURE PROFILES ON HEAT TRANSFER MACH 8 MODEL, Mo = 6

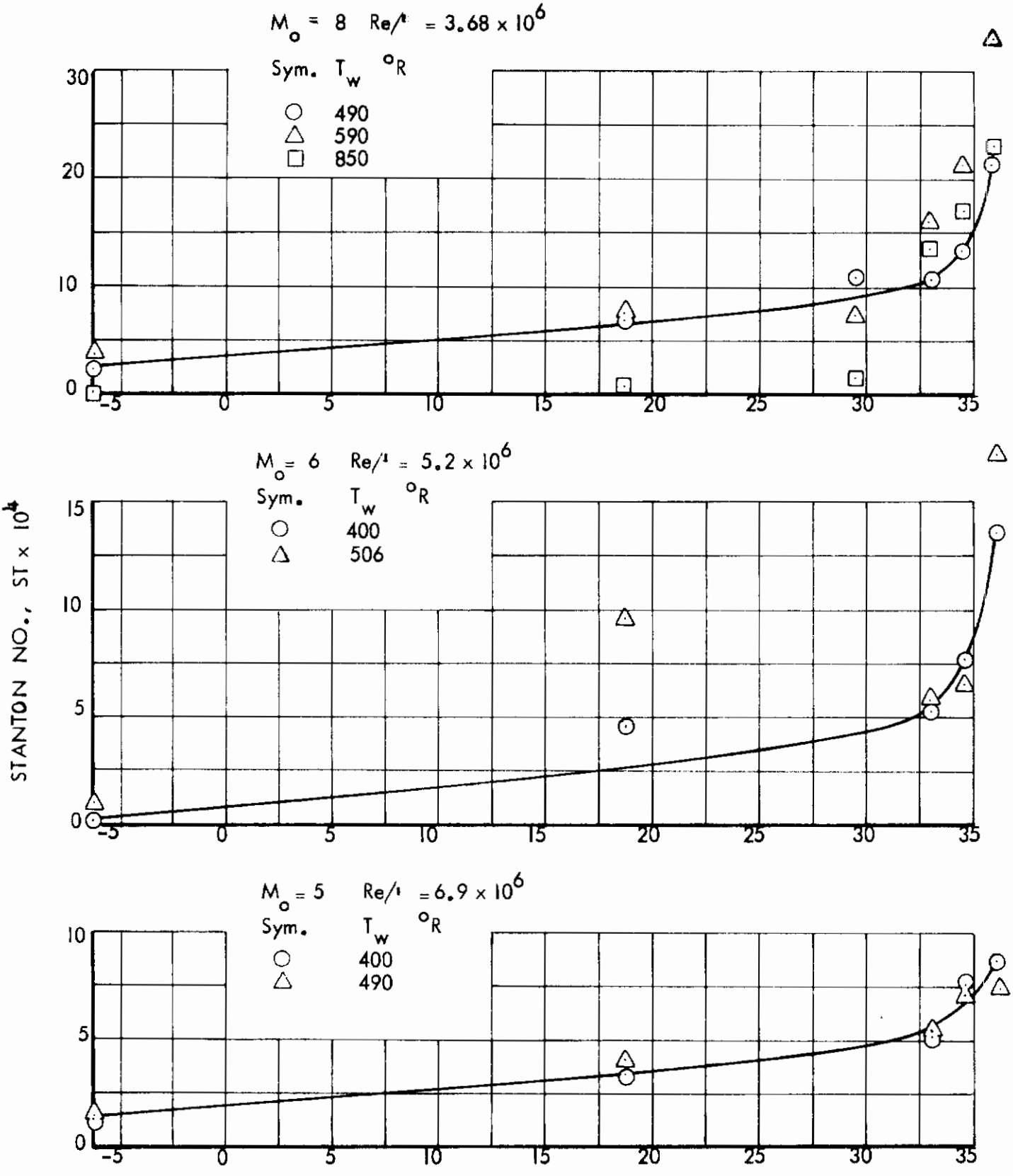

FIGURE 36 DISTRIBUTION OF STANTON NUMBER ALONG HEAT TRANSFER MACH 8 MODEL

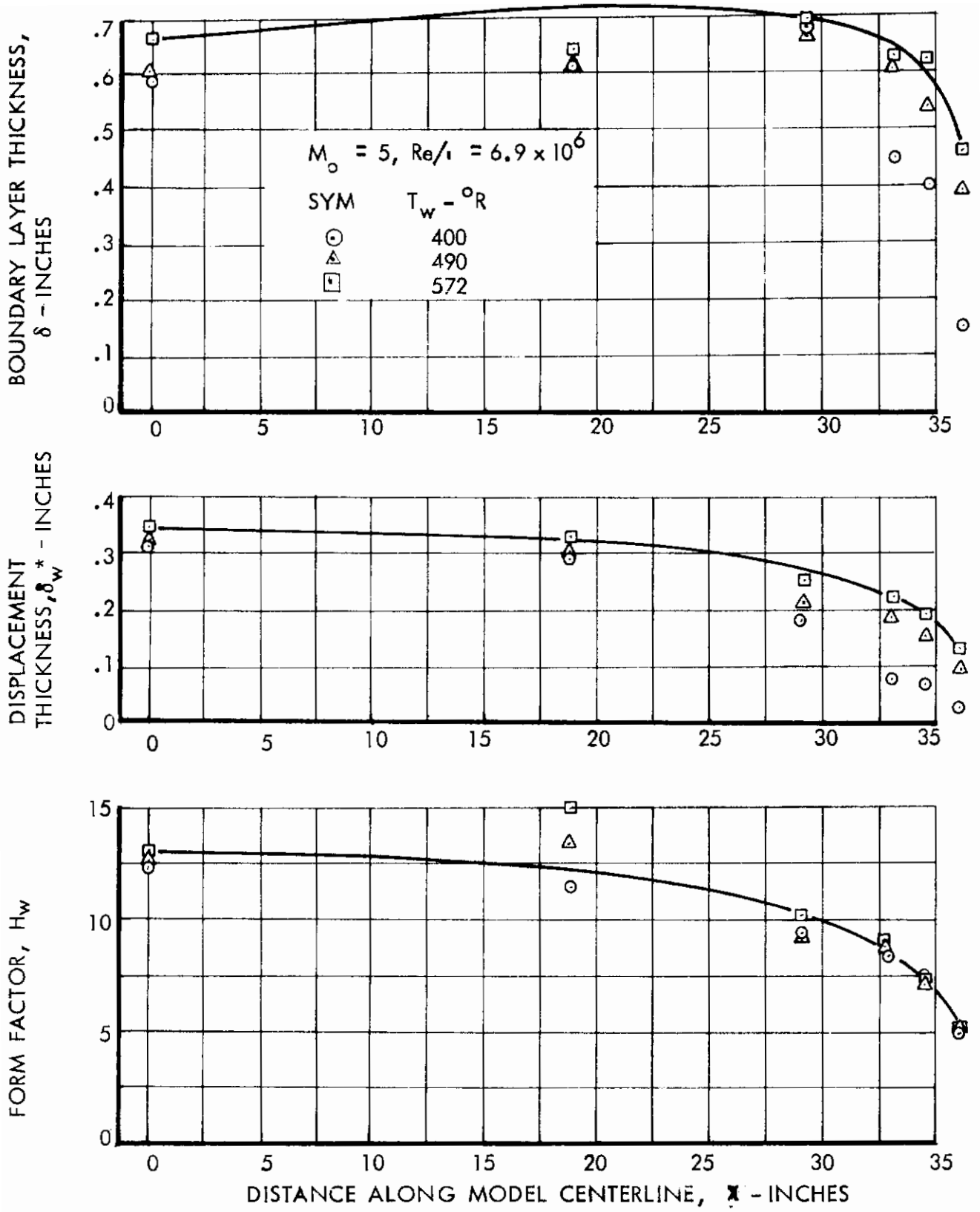

FIGURE 37 BOUNDARY LAYER CHARACTERISTICS ALONG HEAT TRANSFER MACH 8 MODEL, Mo = 5

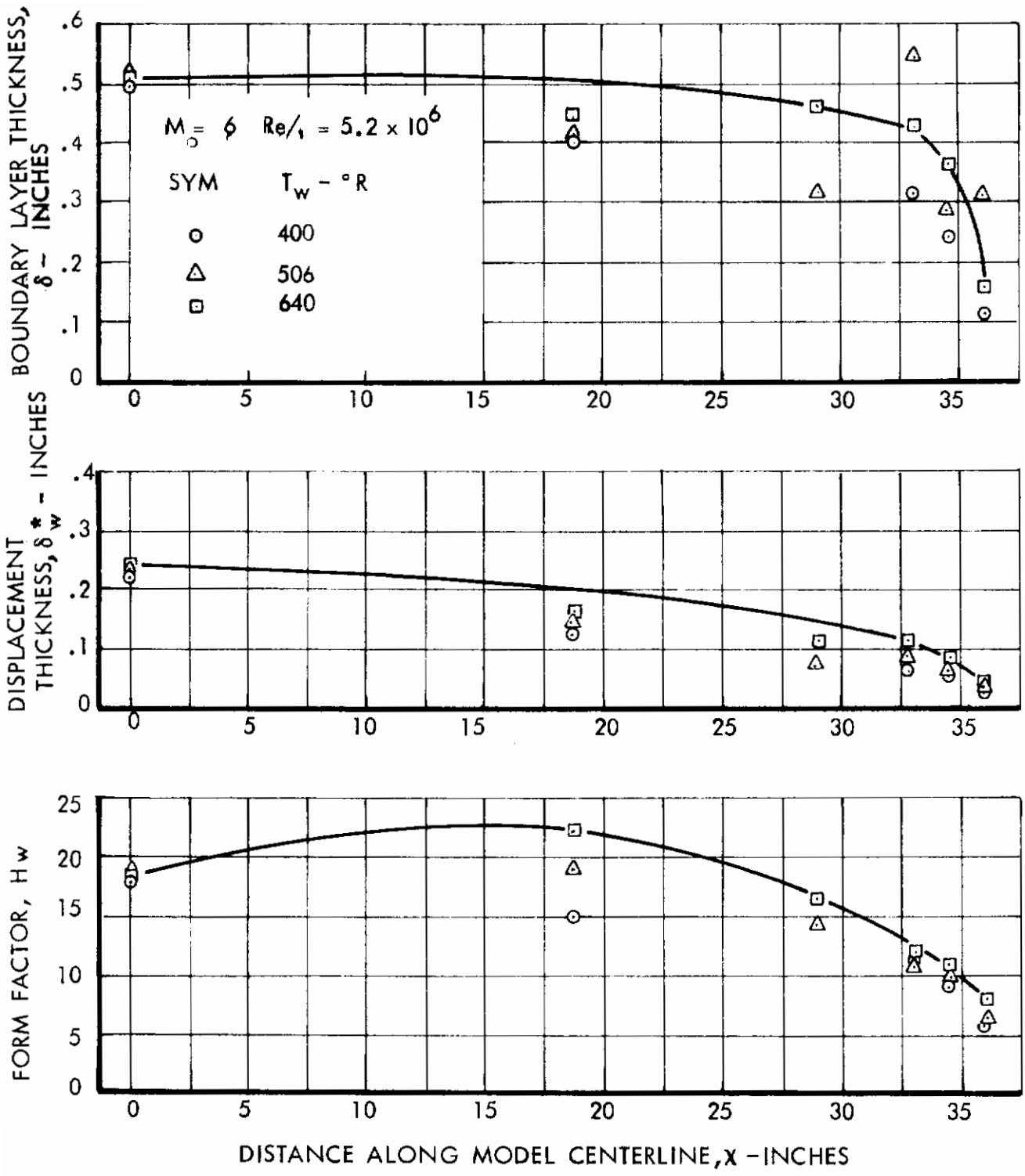

FIGURE 38 BOUNDARY LAYER CHARACTERISTICS ALONG HEAT TRANSFER MACH 8 MODEL, $M_o = 6$

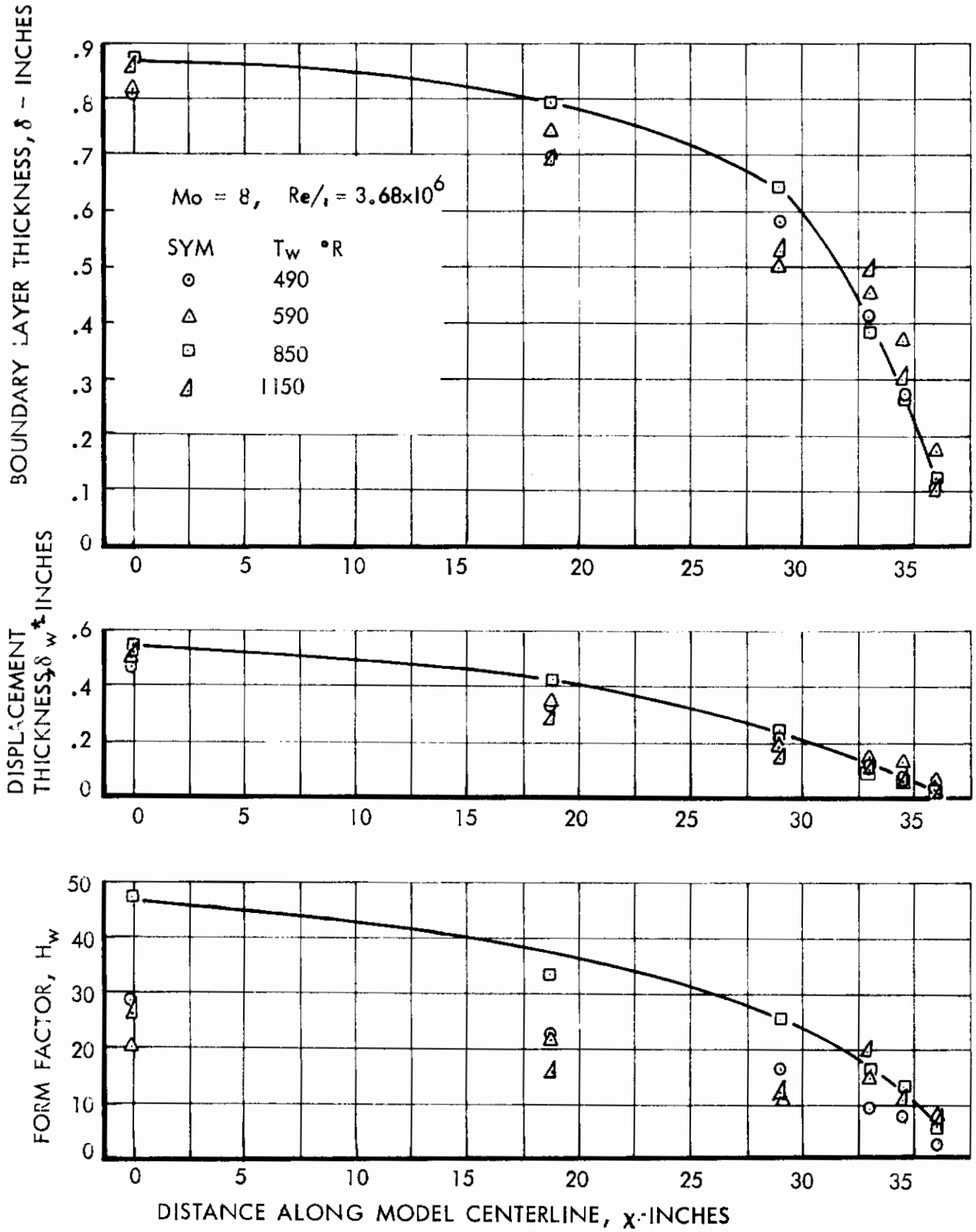

FIGURE 39 BOUNDARY LAYER CHARACTERISTICS ALONG HEAT TRANSFER MACH 8 MODEL, Mo = 8

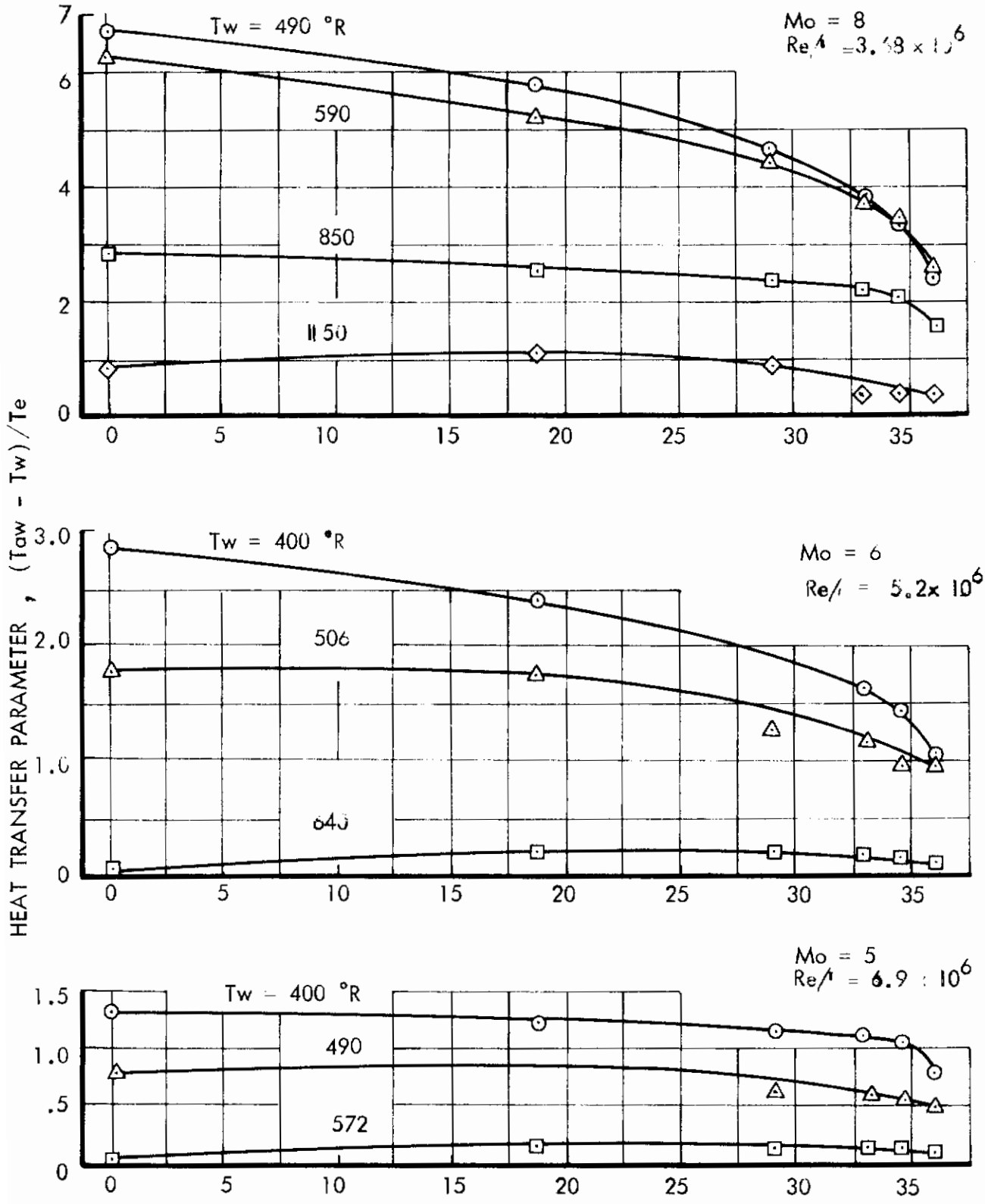

FIGURE 40 VARIATION OF HEAT TRANSFER PARAMETER ON MACH 8 MODEL

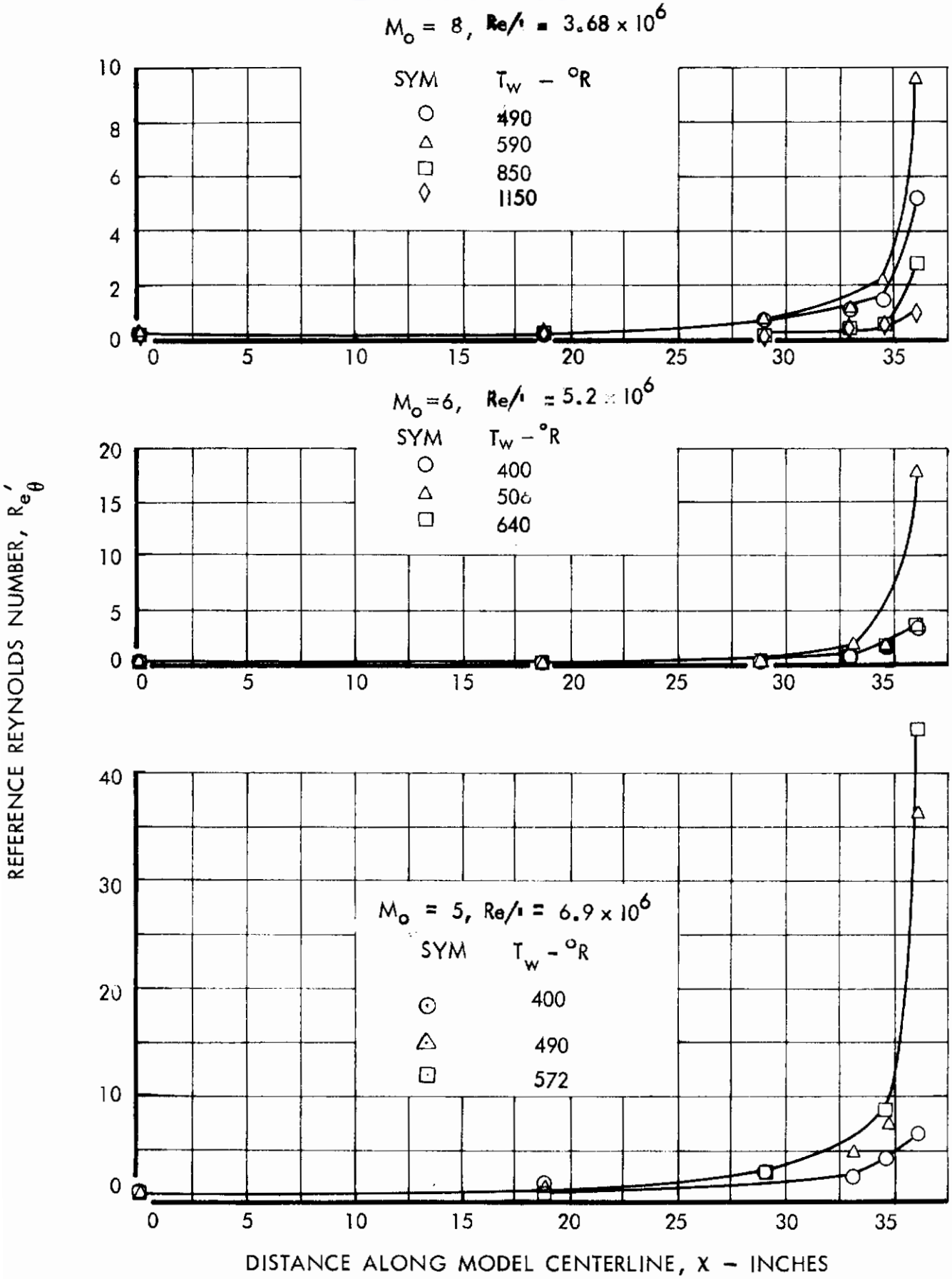

FIGURE 41 VARIATION OF REFERENCE REYNOLDS NUMBER Re'_θ ON MACH 8 MODEL

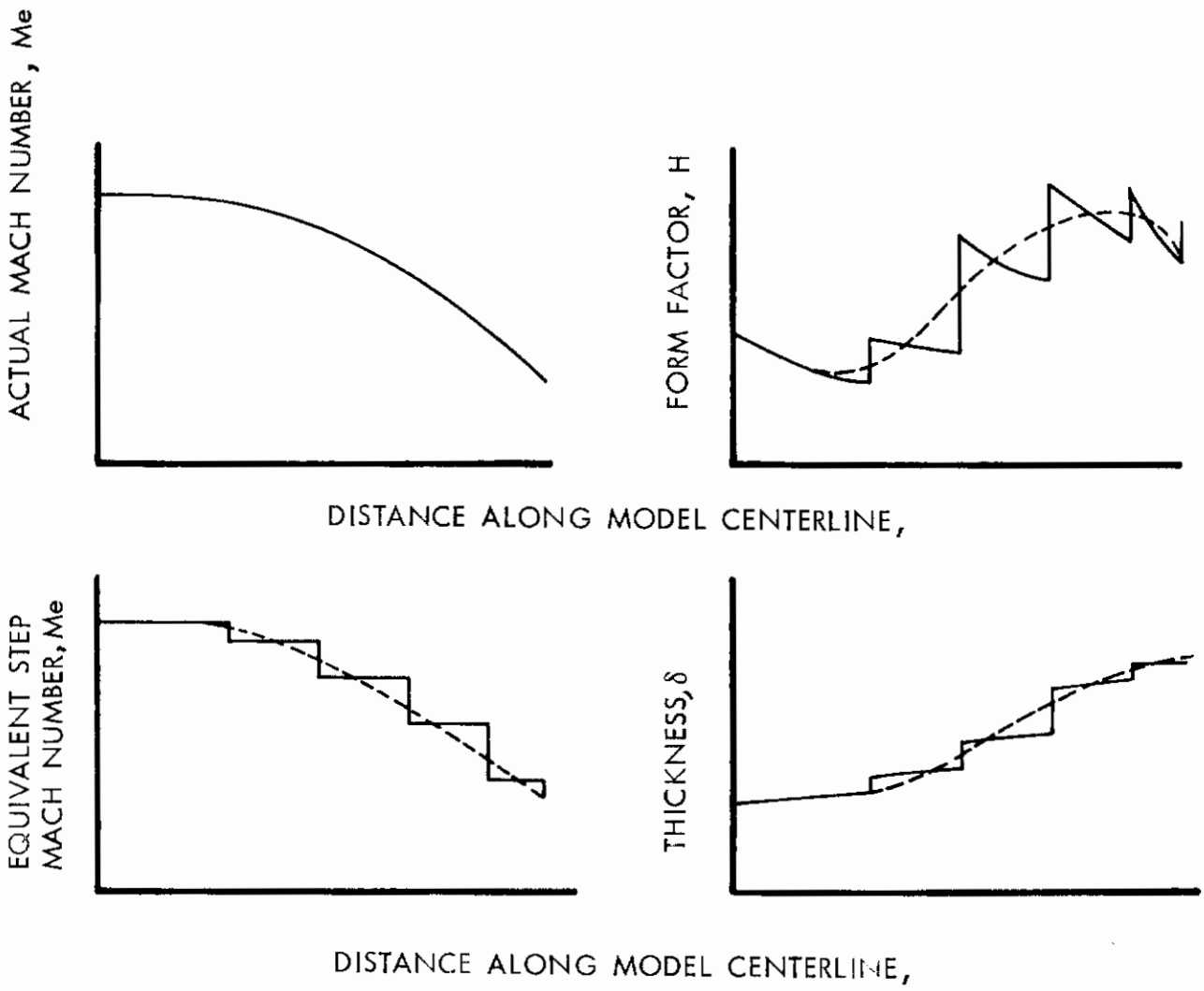

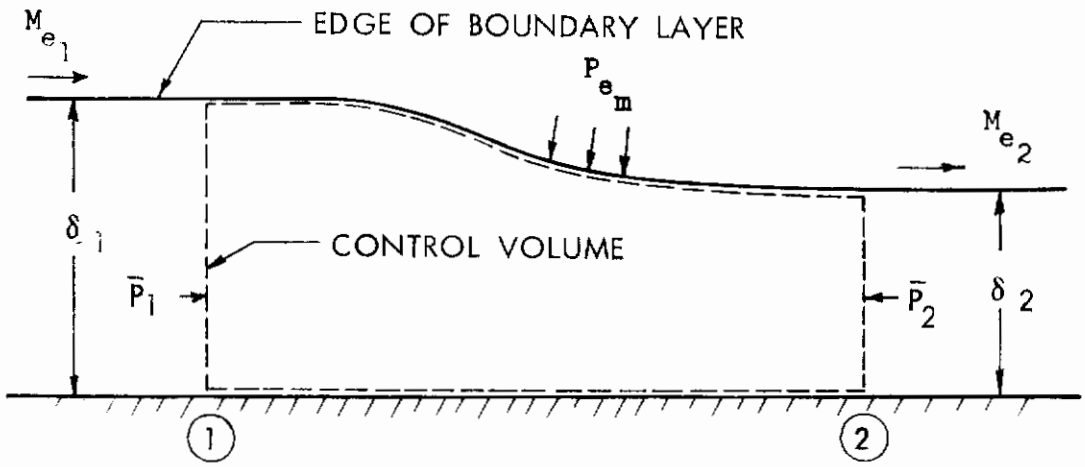

FIGURE 42. BOUNDARY LAYER DISCONTINUITY/ANALOGY METHOD

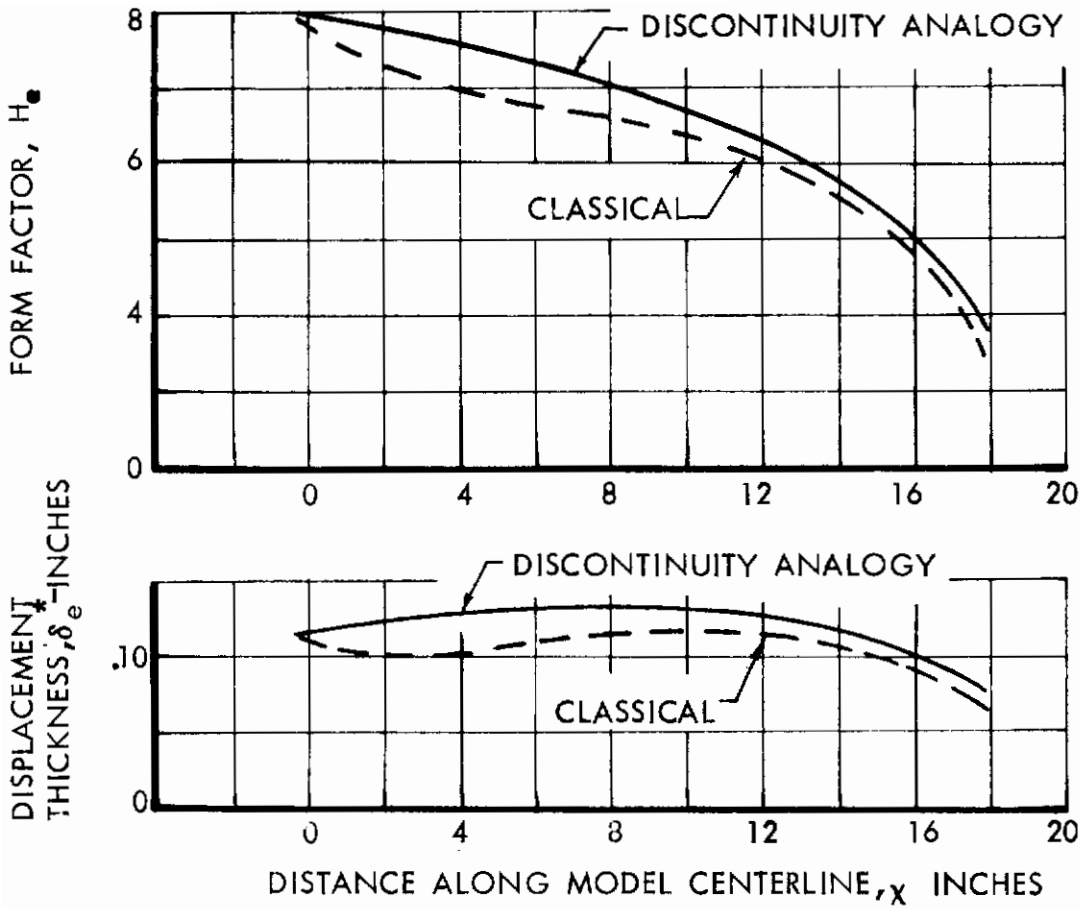

FIGURE 43 (a) COMPARISON OF DISCONTINUITY/ANALOGY AND CLASSICAL THEORIES, Mo =4

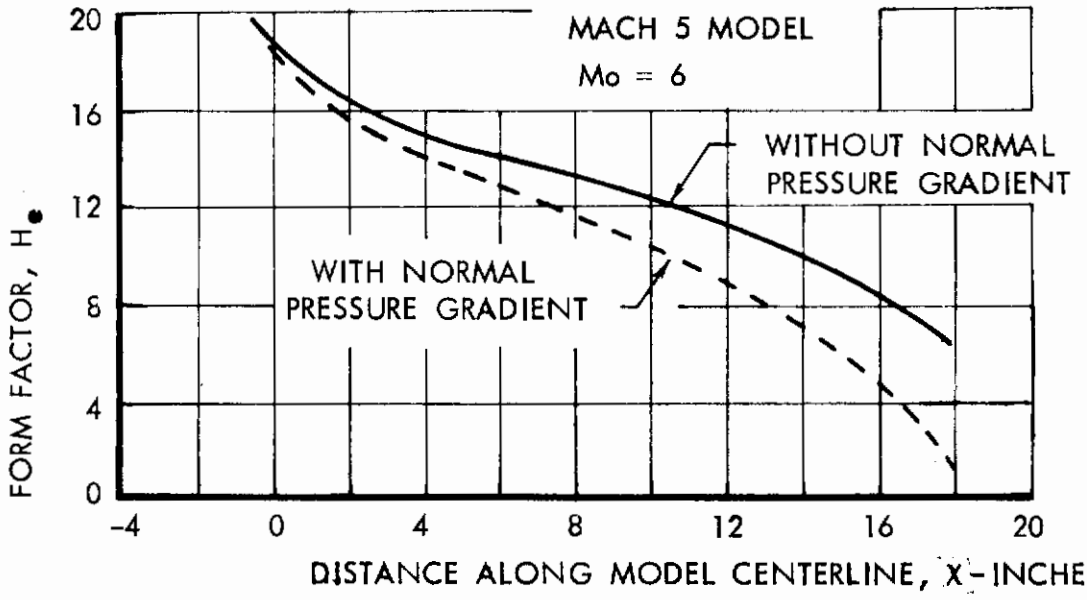

FIGURE 43 (b) CENTRIFUGAL FORCE EFFECTS ON FORM FACTOR

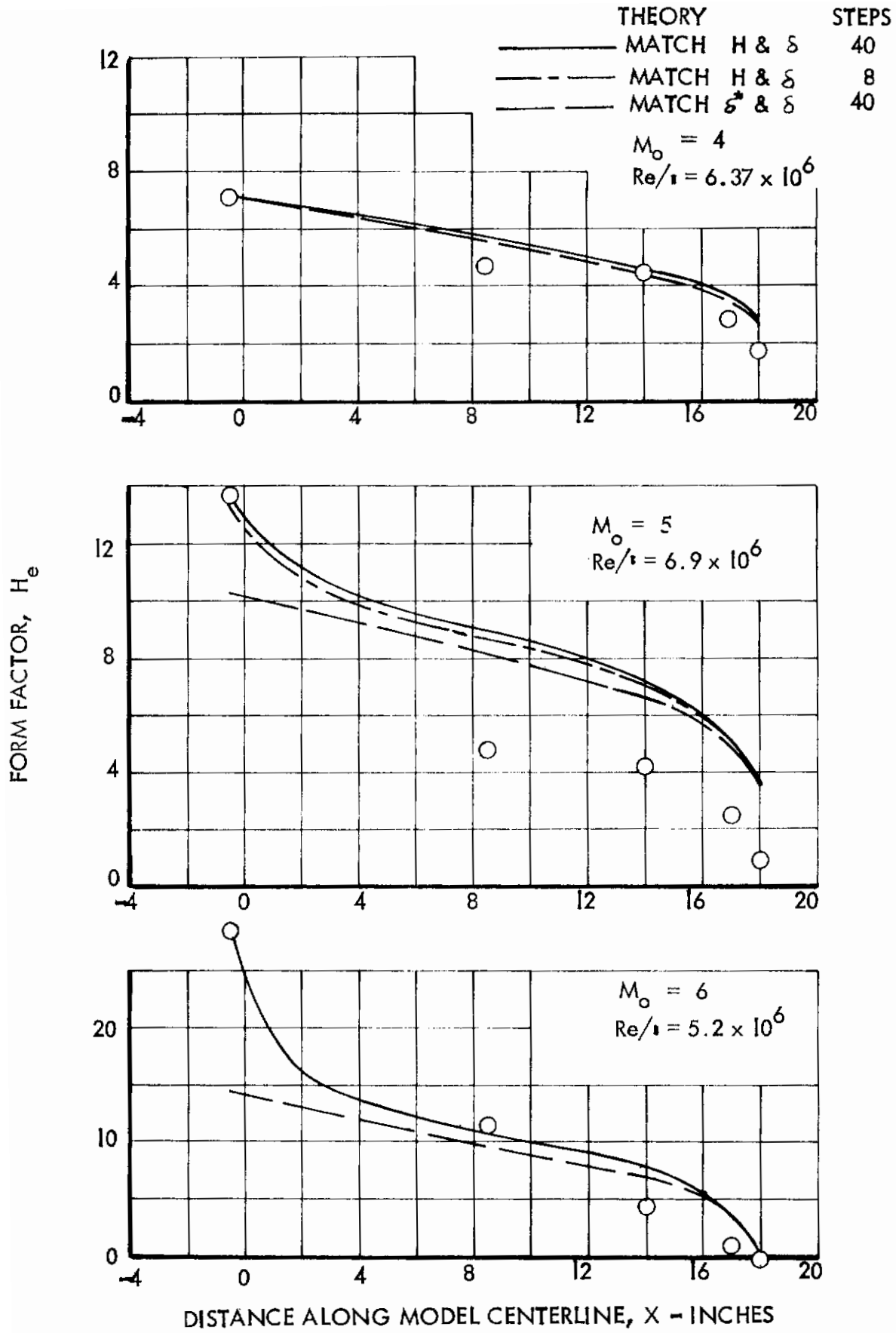

FIGURE 44 CORRELATION OF FORM FACTOR H_e ON MACH 5 MODEL, 17 INCH CYLINDER

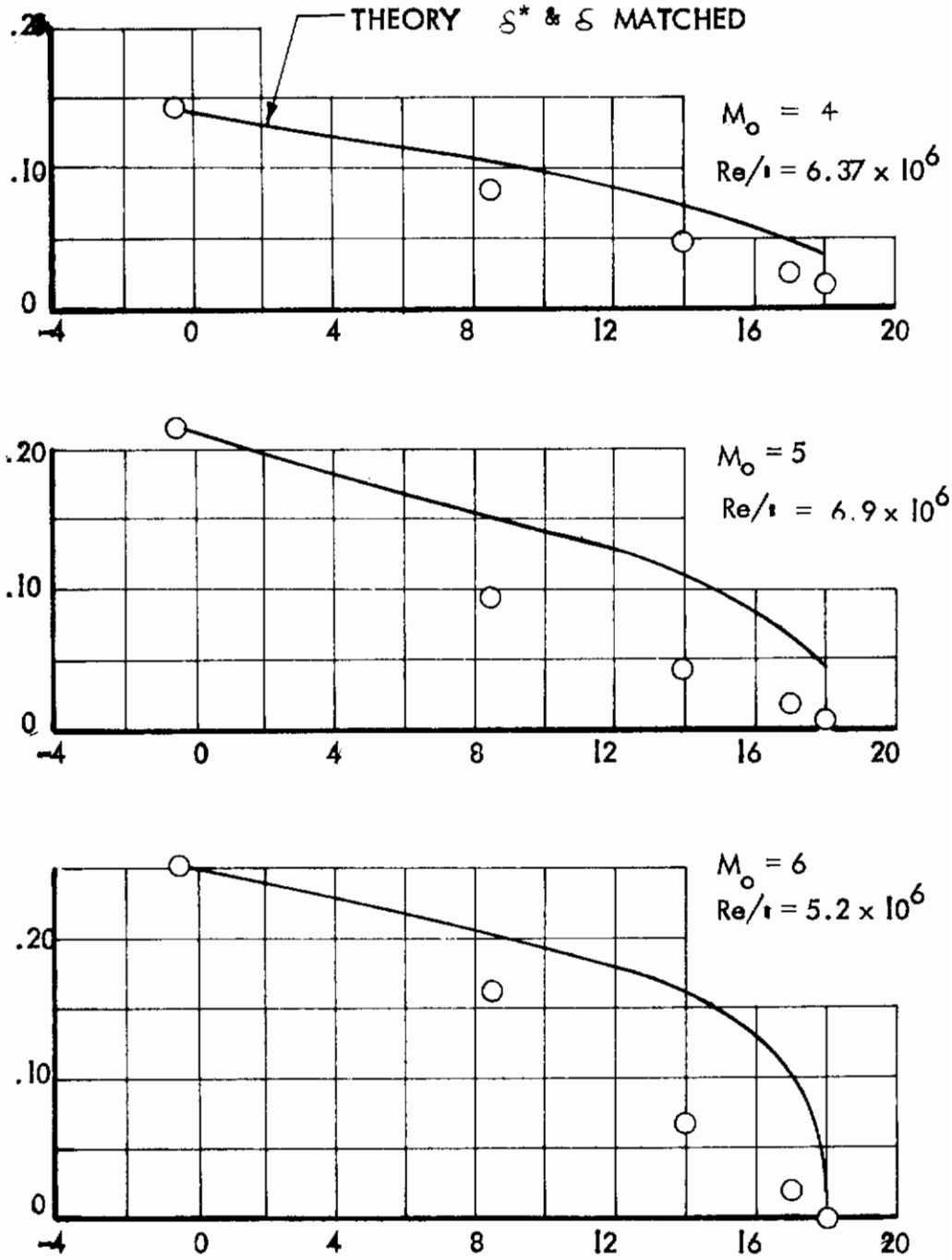

FIGURE 45 CORRELATION OF DISPLACEMENT THICKNESS δ_e^* ON MACH 5 MODEL, 17 INCH CYLINDER

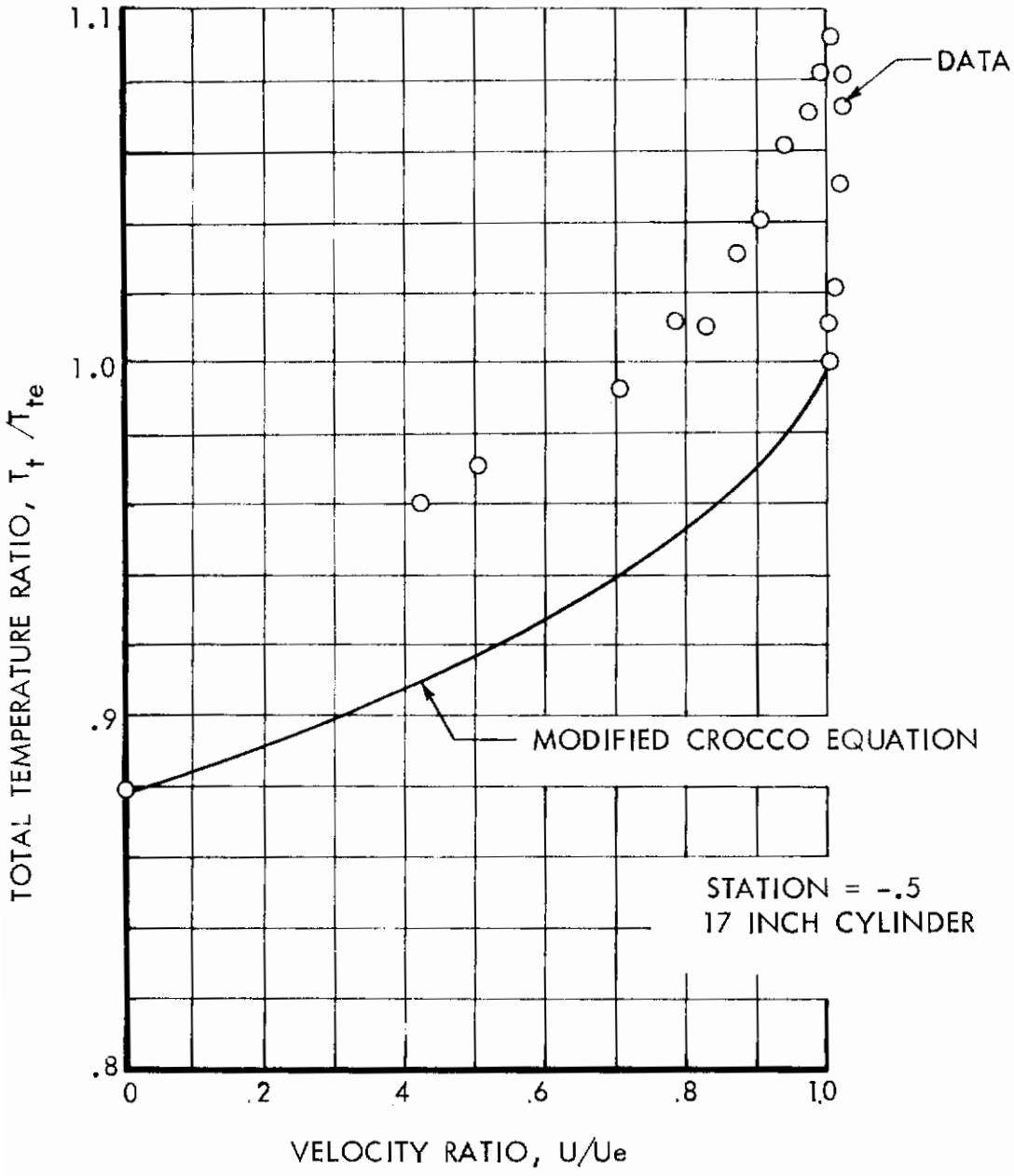

FIGURE 46. TOTAL TEMPERATURE COMPARISON, Mo = 6

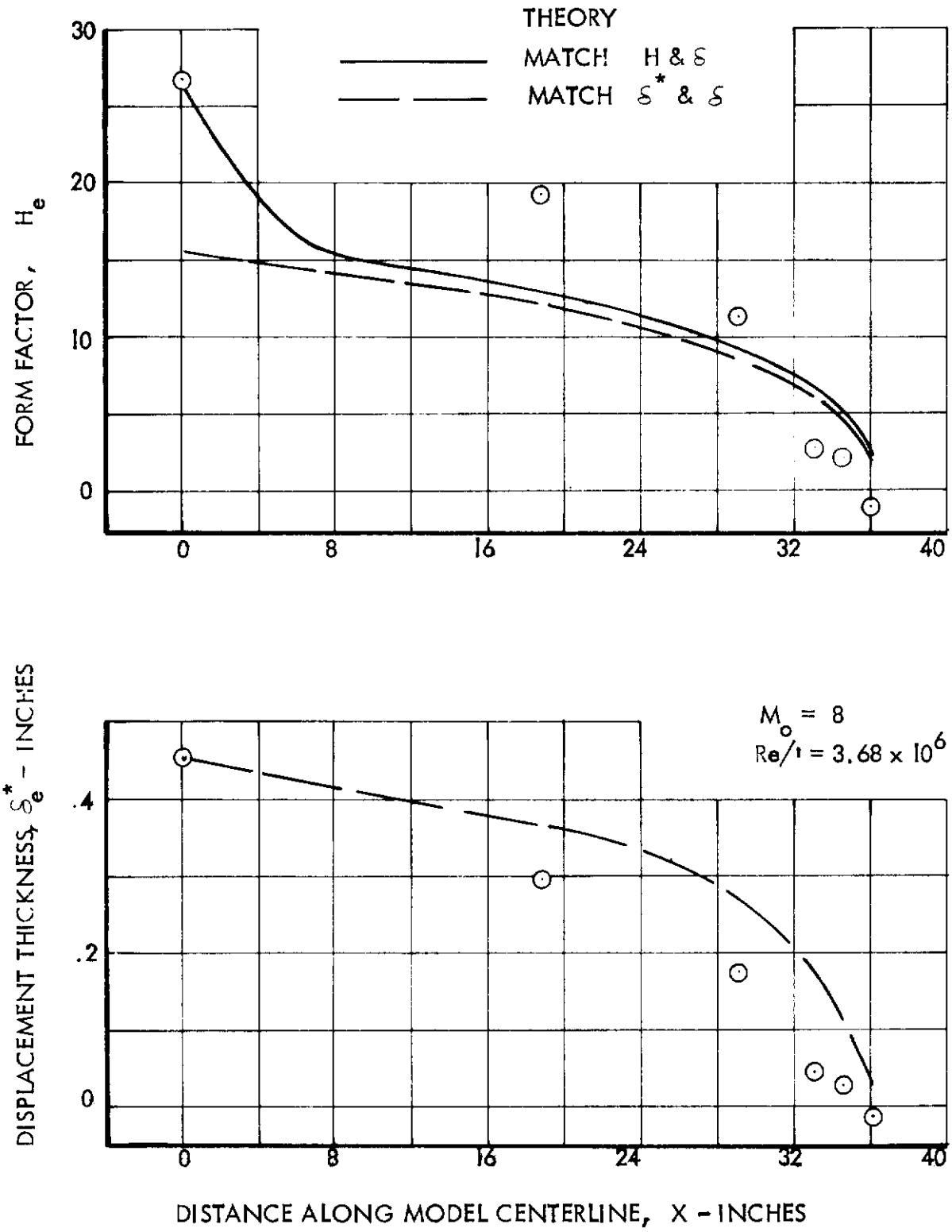

FIGURE 47 CORRELATION OF FORM FACTOR H_e AND DISPLACEMENT THICKNESS δ_e^* ON MACH 8 MODEL, $T_w = 490\ ^\circ R$

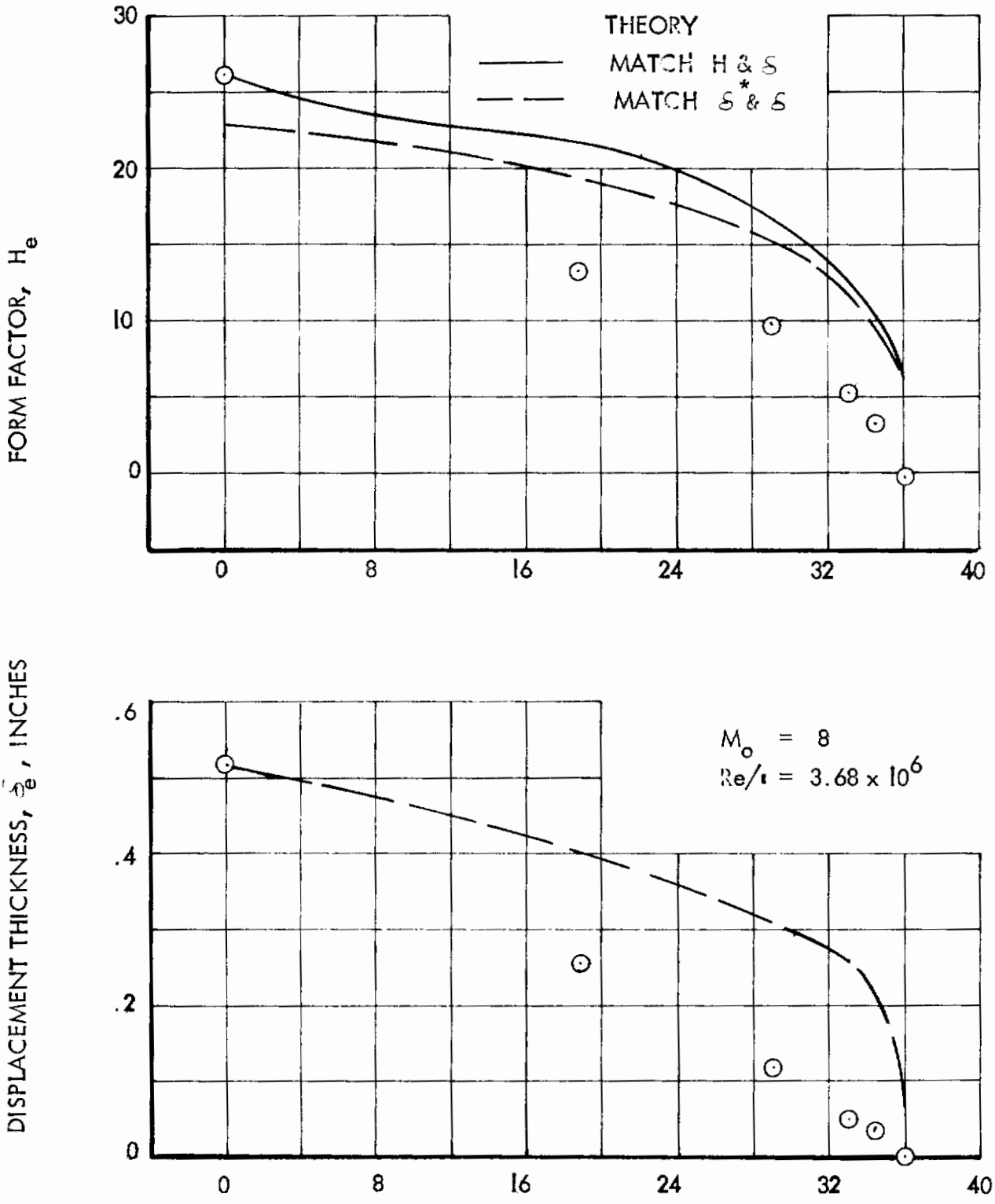

FIGURE 48 CORRELATION OF FORM FACTOR H_e AND DISPLACEMENT THICKNESS δ_e^* ON MACH 8 MODEL, T_w = 1150°R

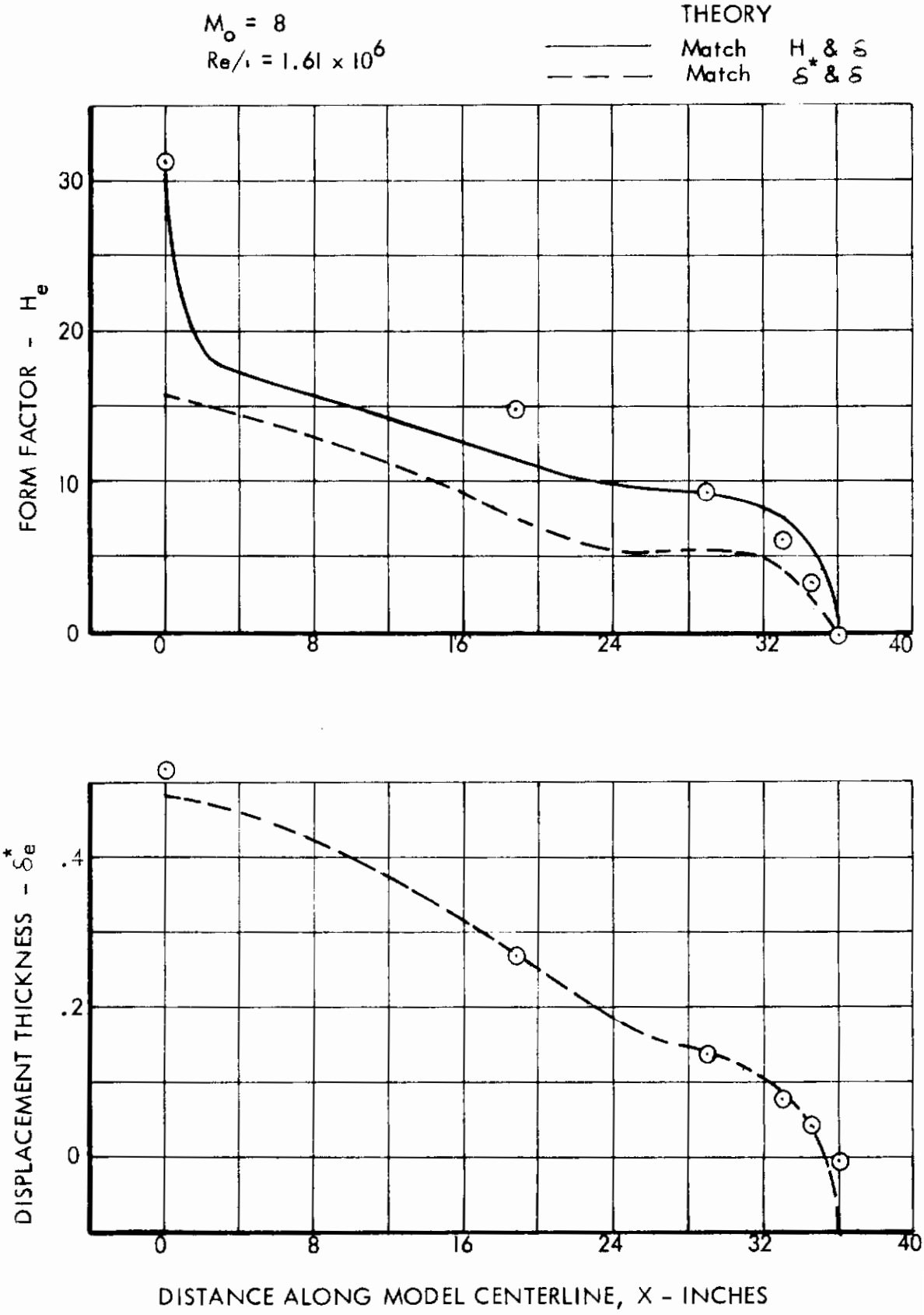

FIGURE 49 CORRELATION OF FORM FACTOR H_e AND DISPLACEMENT THICKNESS δ_e^* ON MACH 8 MODEL, T_w = 490 °R

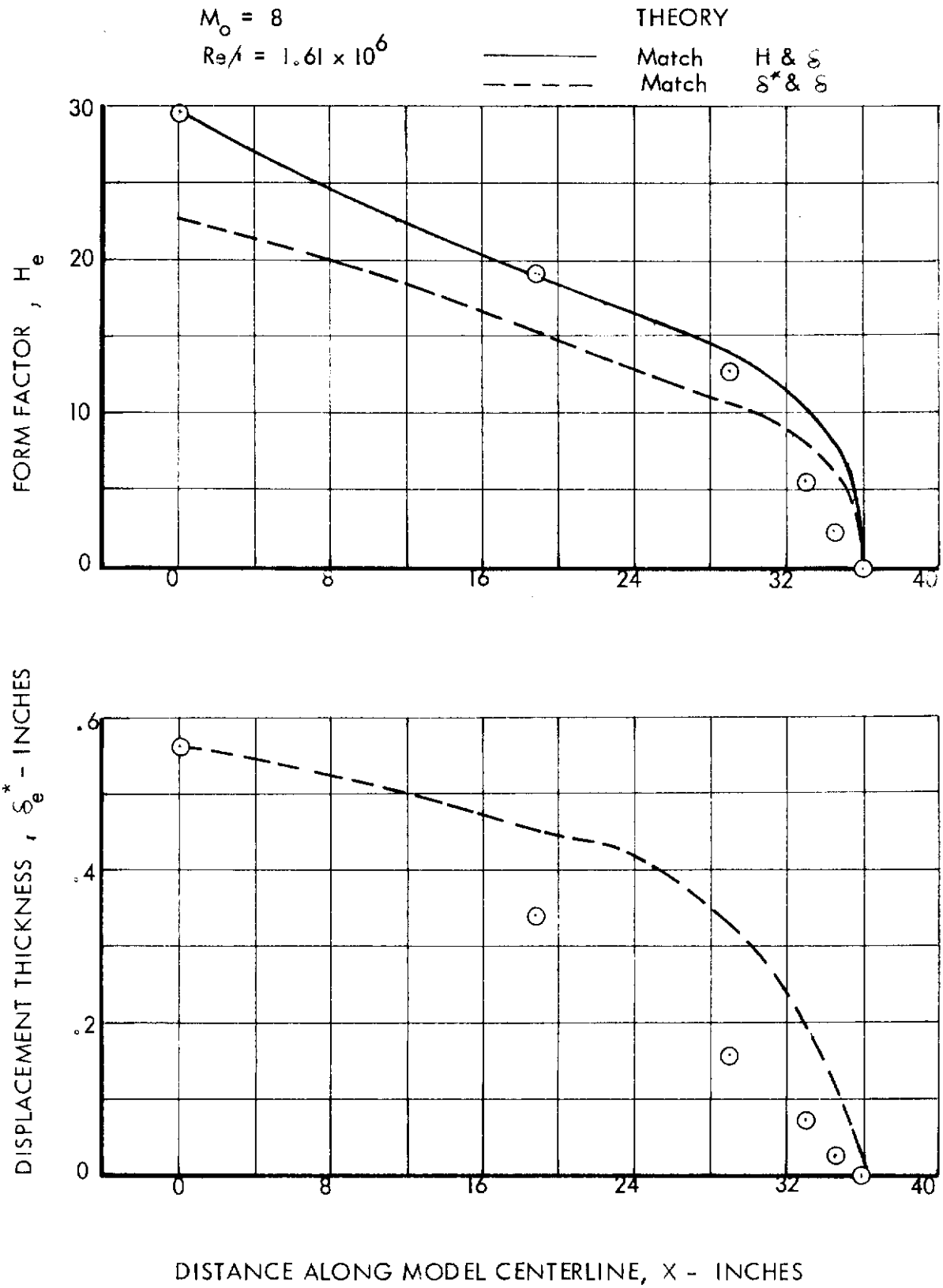

FIGURE 50 CORRELATION OF FORM FACTOR H_e AND DISPLACEMENT THICKNESS δ^*_e ON MACH 8 MODEL, T_w = 1178° R

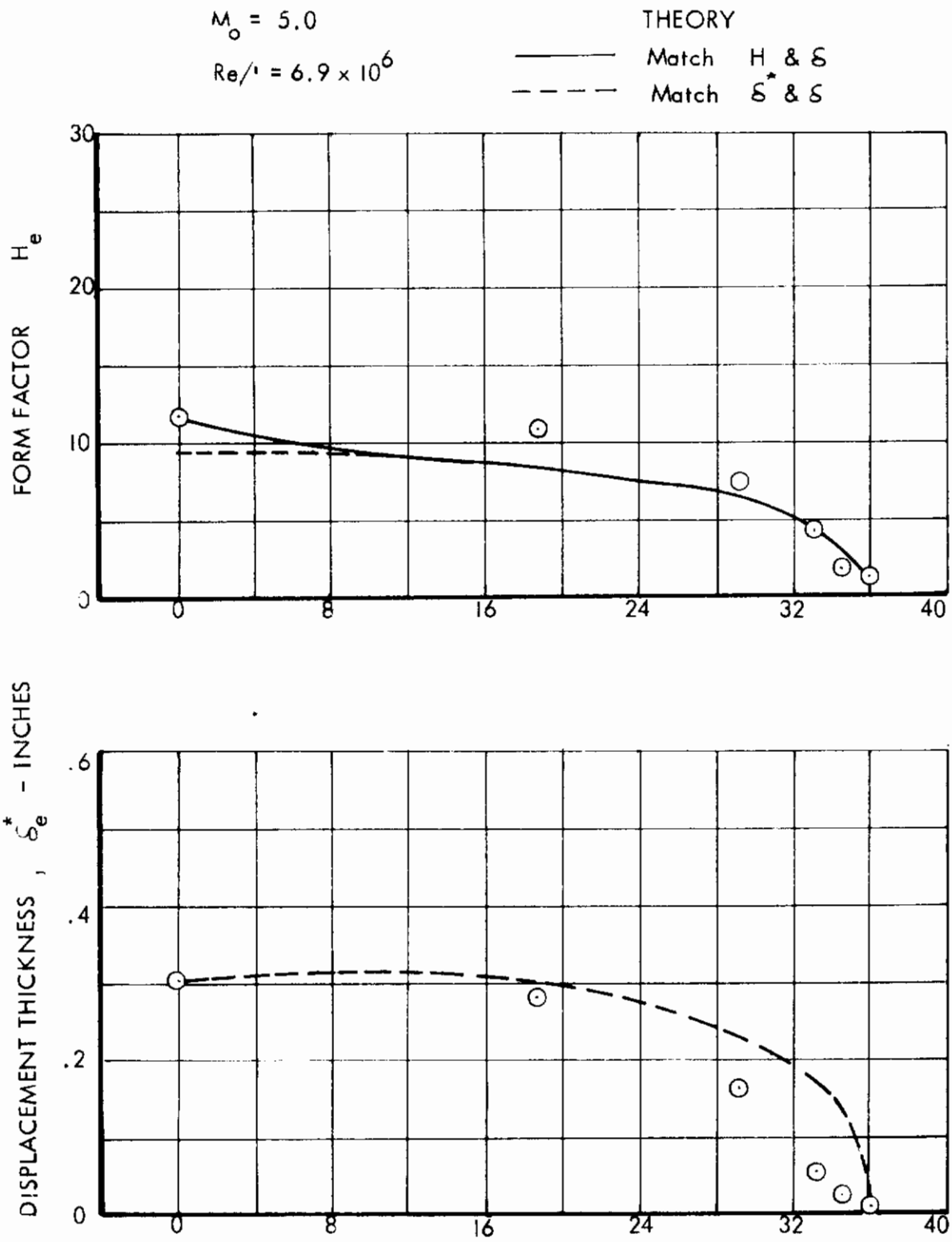

FIGURE 51 CORRELATION OF FORM FACTOR H_e AND DISPLACEMENT THICKNESS δ^*_e ON MACH 8 MODEL, T_w = 400° R

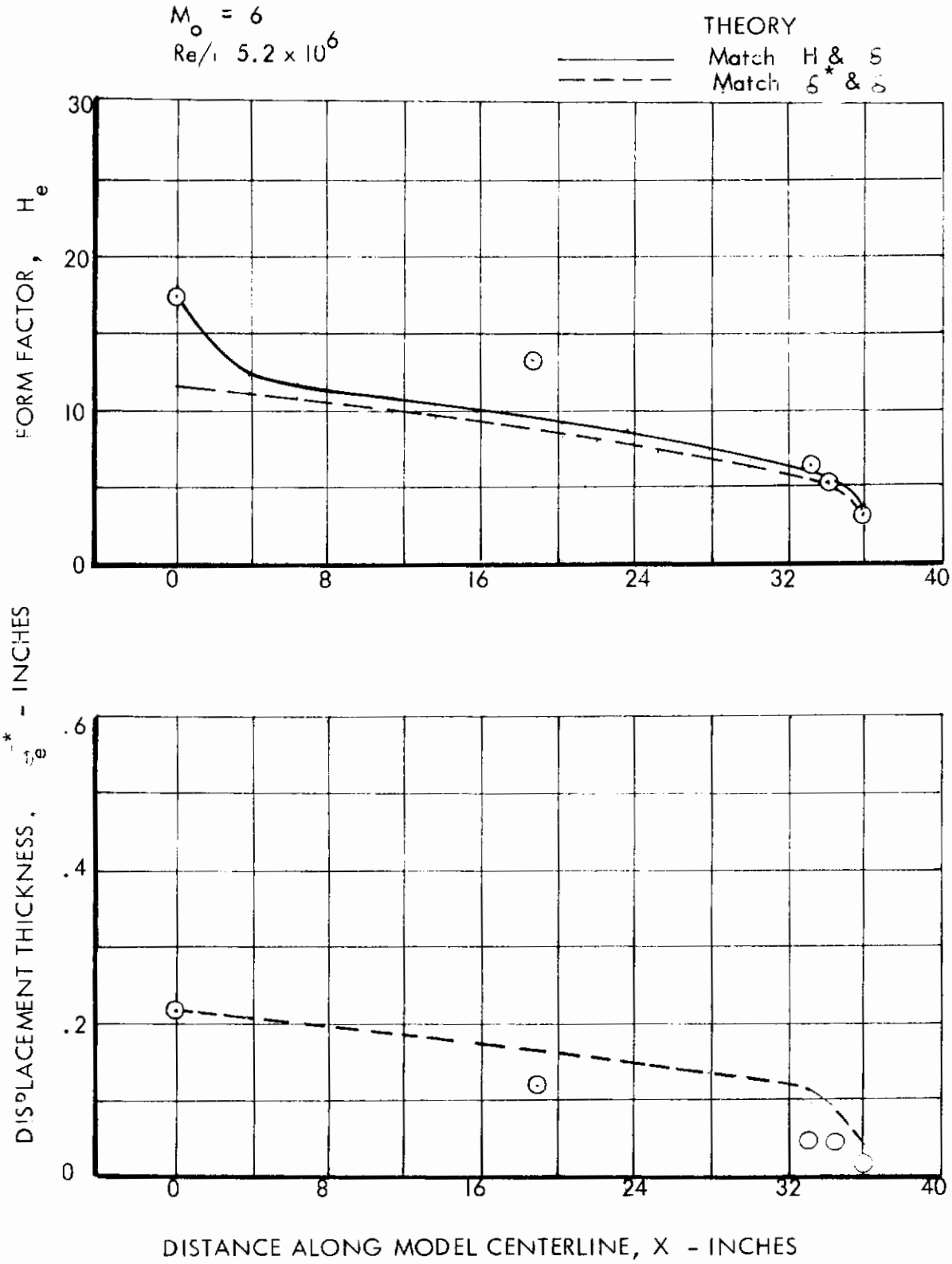

FIGURE 52 CORRELATION OF FORM FACTOR H_e AND DISPLACEMENT THICKNESS, δ_e^* ON MACH 8 MODEL, T_w = 400°R

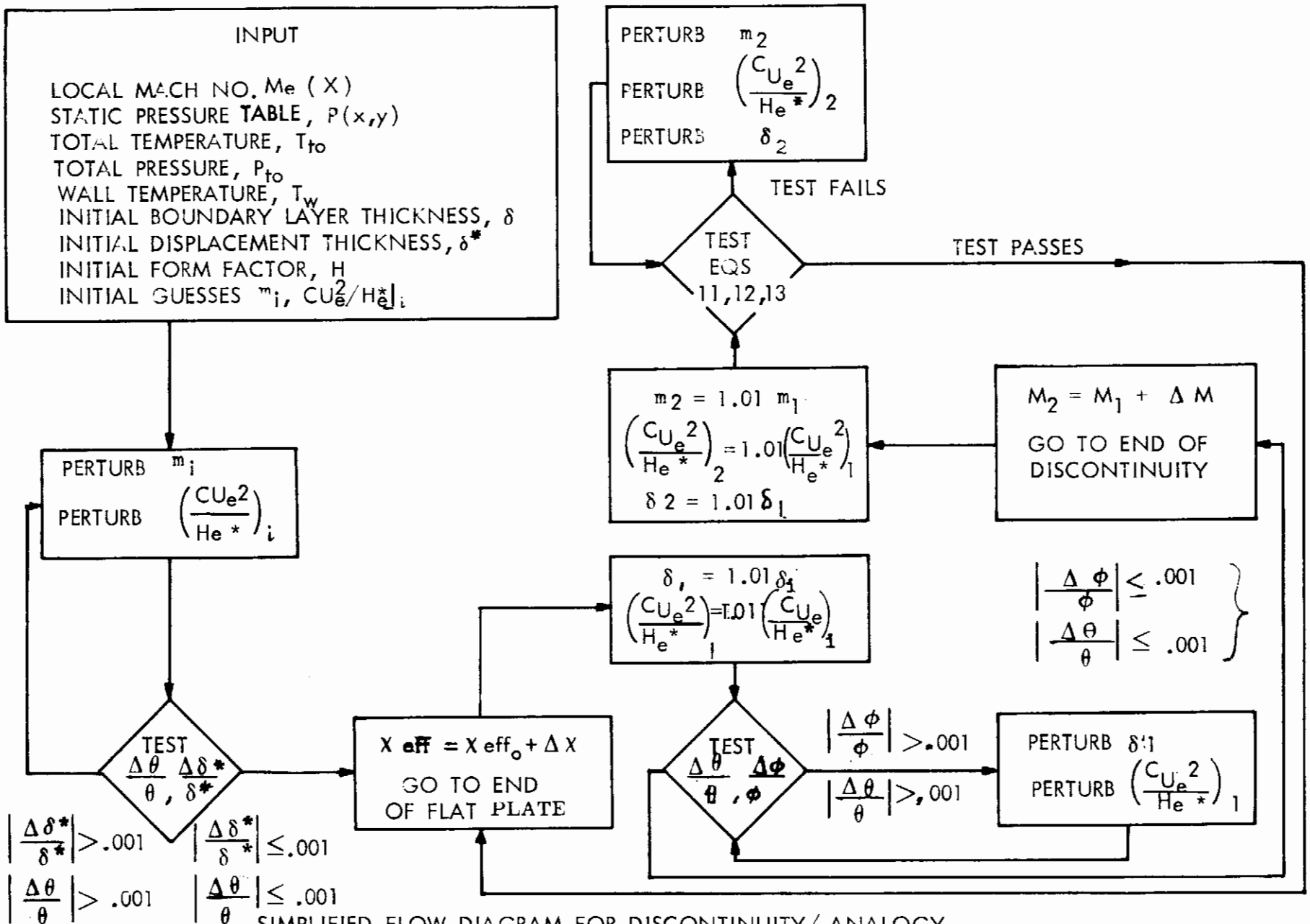

FIGURE 53 SIMPLIFIED FLOW DIAGRAM FOR DISCONTINUITY/ ANALOGY PROGRAM WITH PRESSURE GRADIENT NORMAL TO WALL

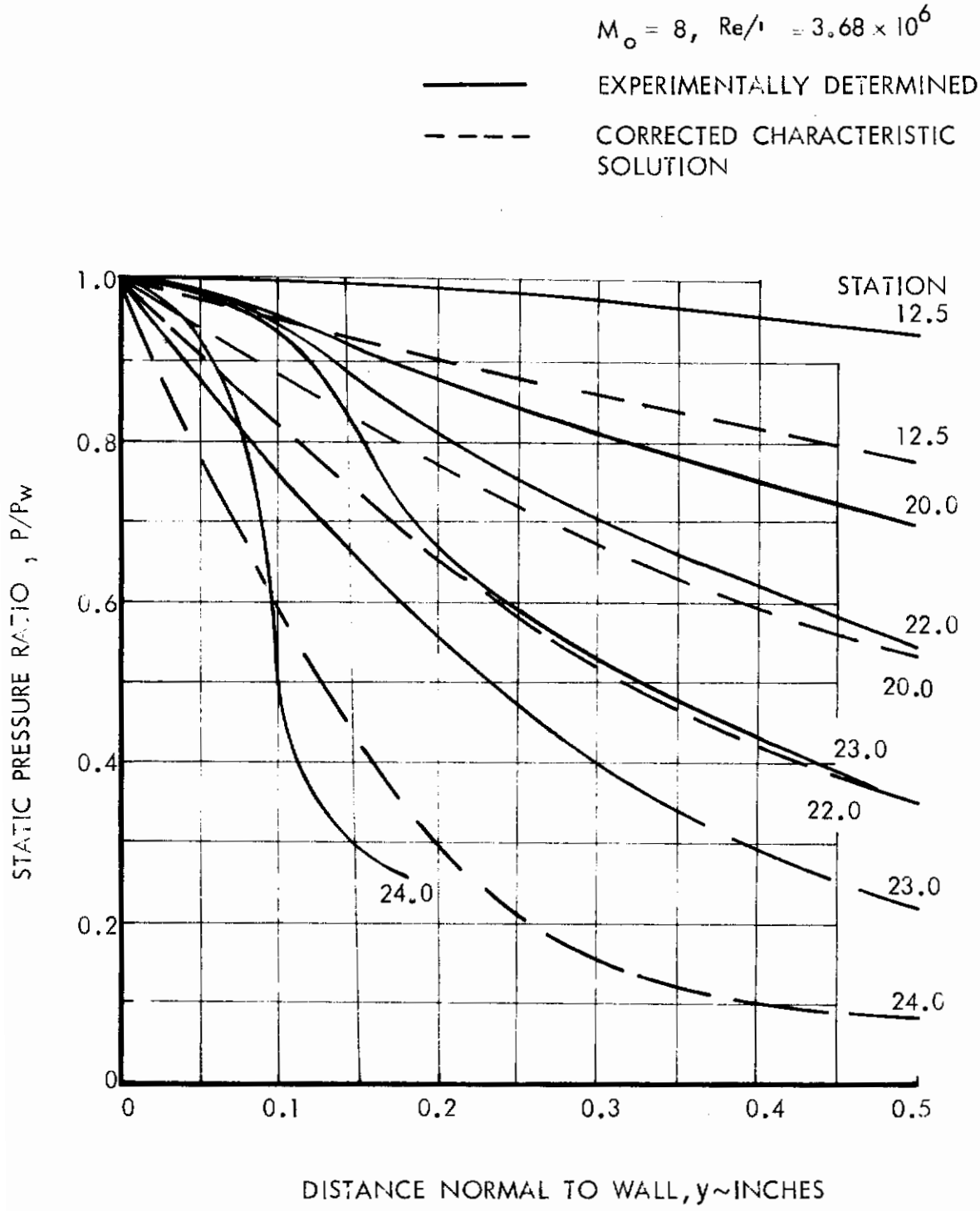

FIGURE 54 STATIC PRESSURES ON MACH 10 MODEL

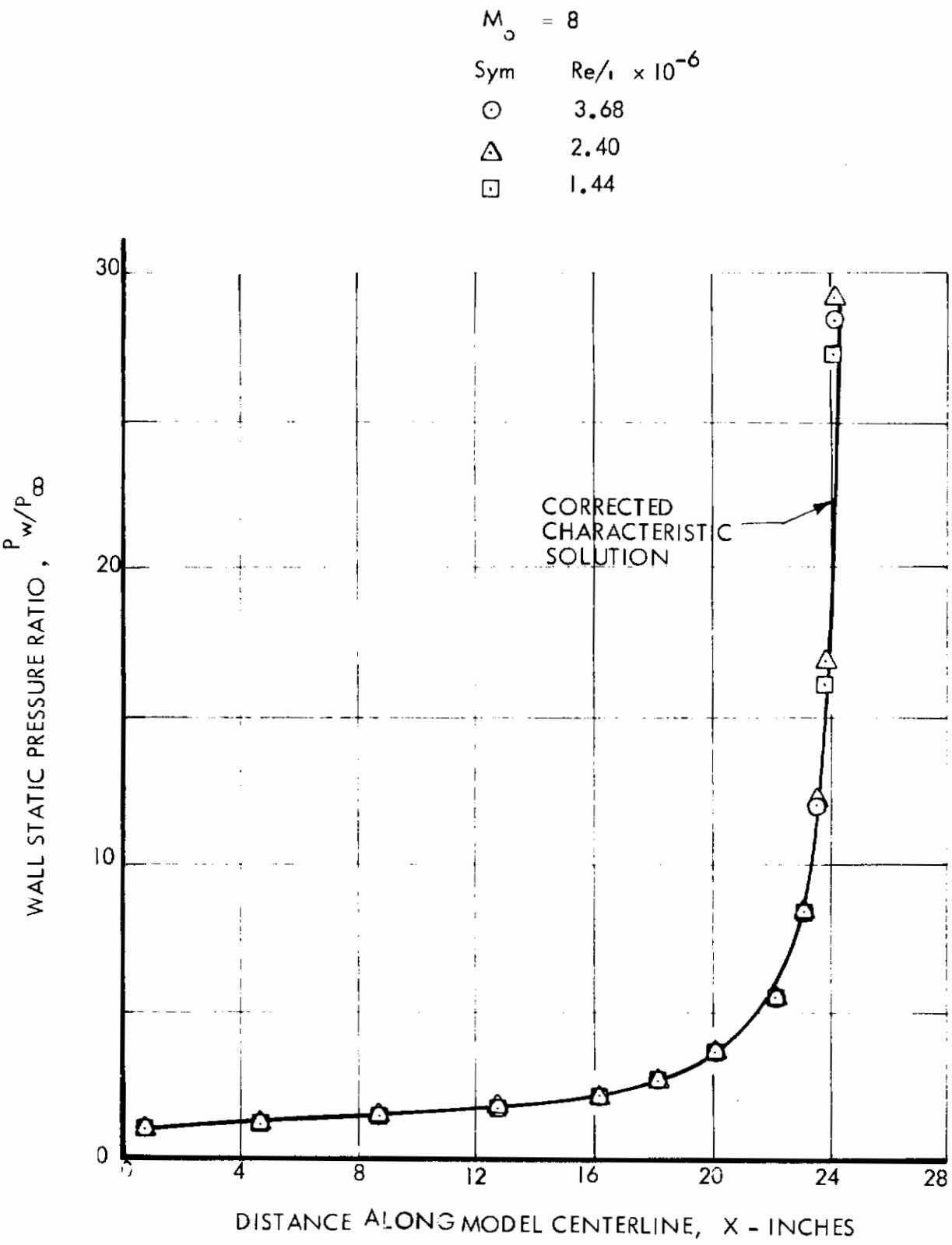

FIGURE 55 STATIC PRESSURE DISTRIBUTION - MACH 10 MODEL

APPARATUS MOUNTED VERTICAL
WATER FLOWS UPWARD

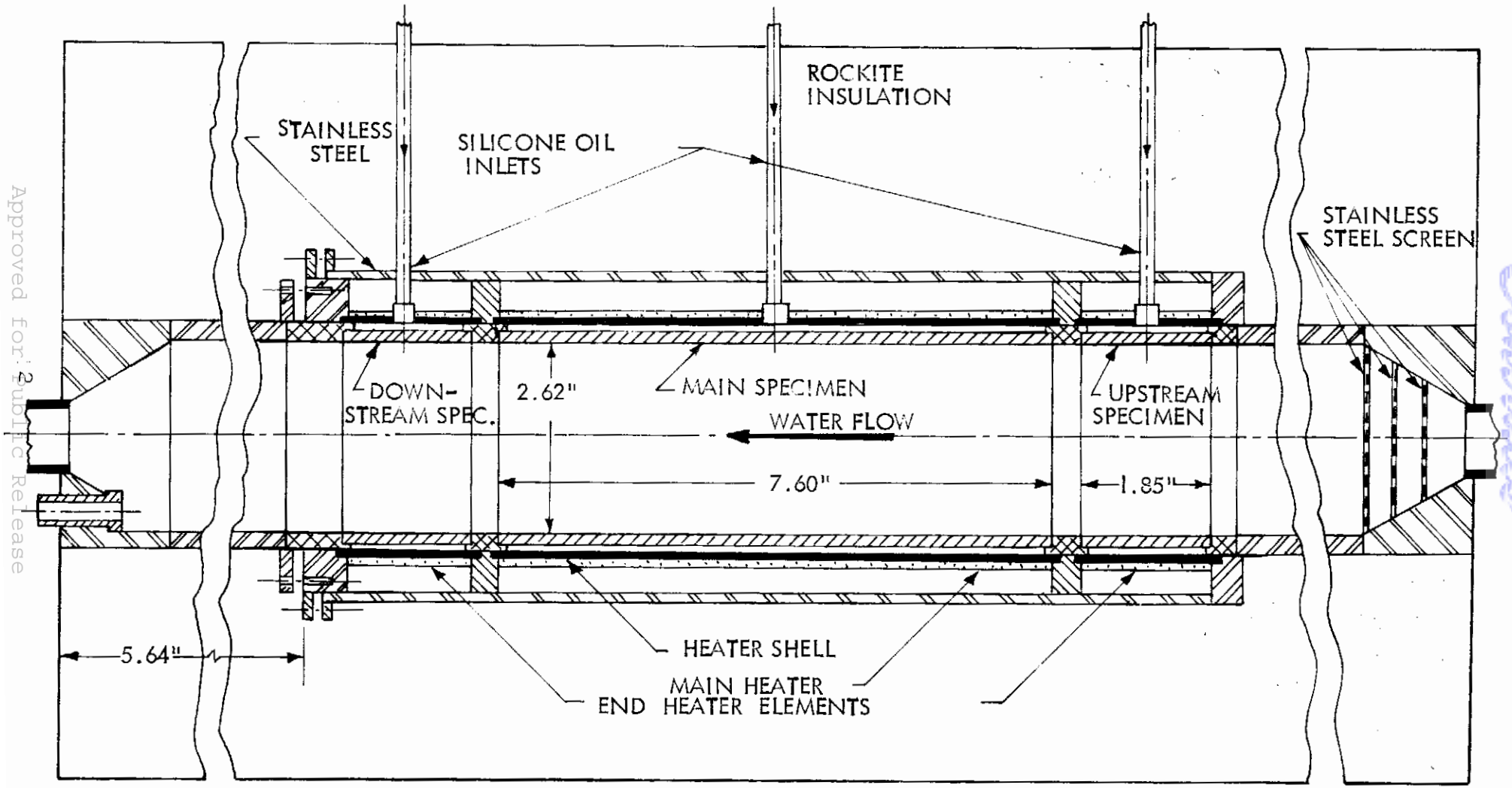

FIGURE 56 HEAT TRANSFER FURNACE

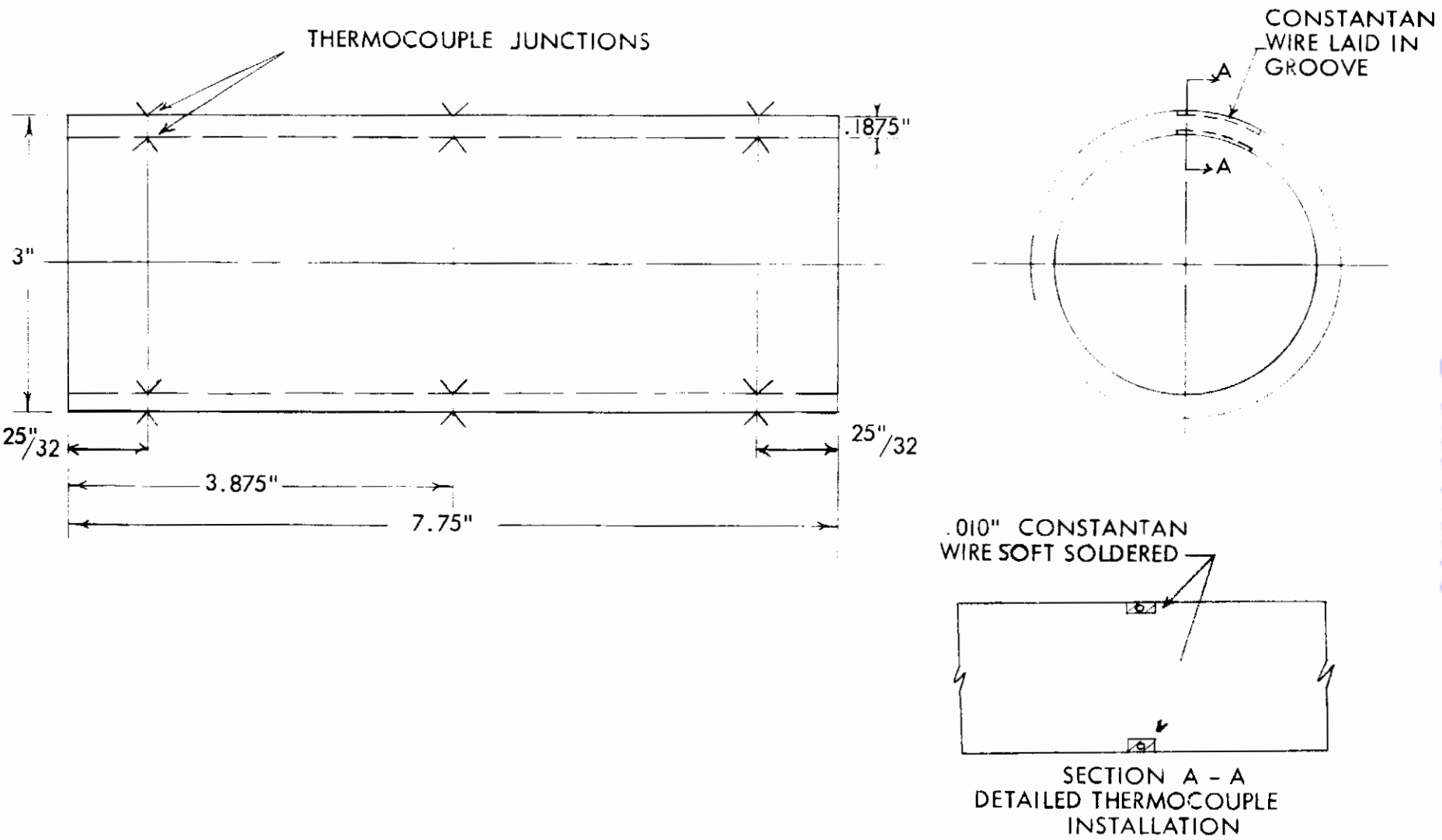

FIGURE 57 STAINLESS STEEL SPECIMEN

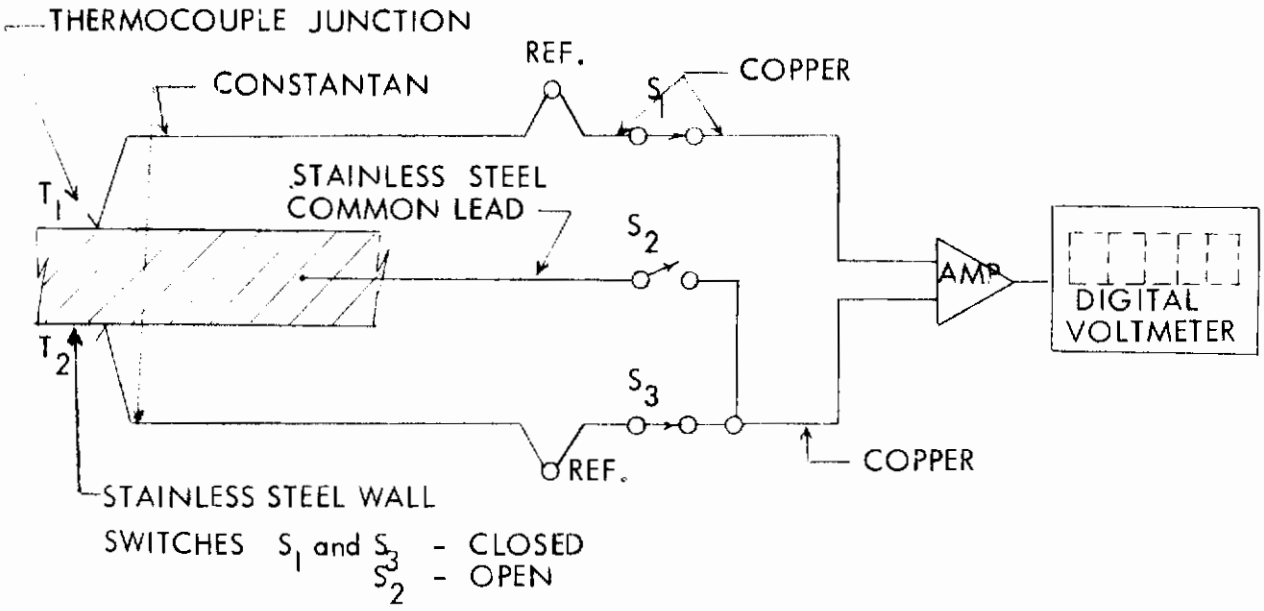

DIFFERENTIAL THERMOCOUPLE , $\Delta T_1 = T_1 - T_2$

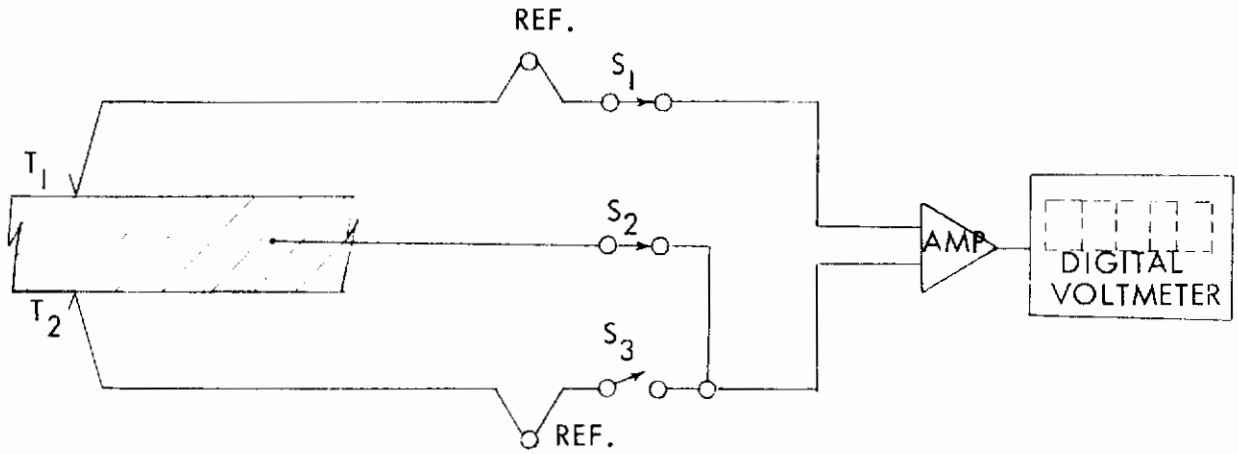

ABSOLUTE THERMOCOUPLE T_1

FIGURE 58 THERMOCOUPLE HOOK-UP

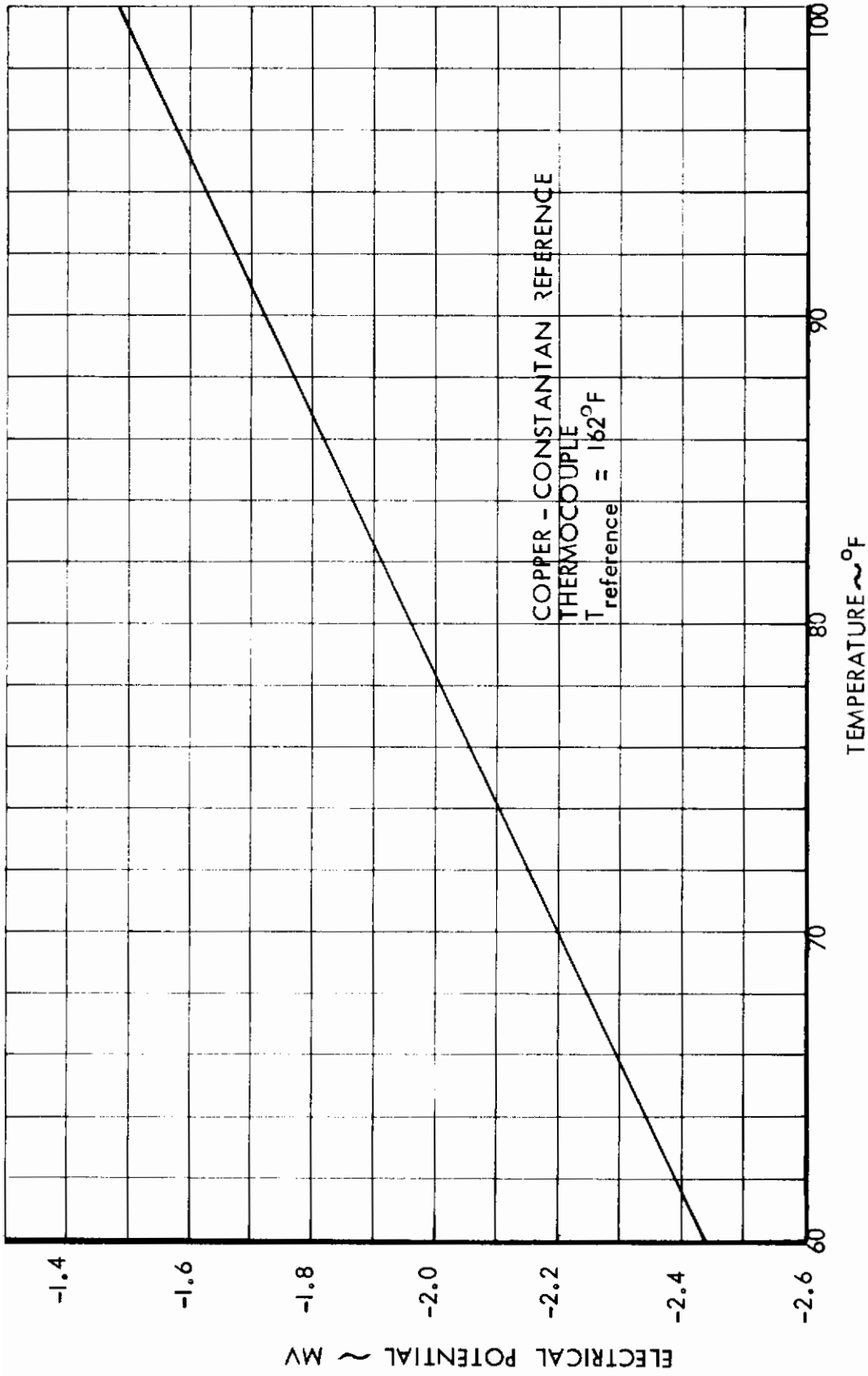

FIGURE 59 CONSTANTAN - STAINLESS STEEL (TYPE 321) THERMOCOUPLE CALIBRATION CURVE

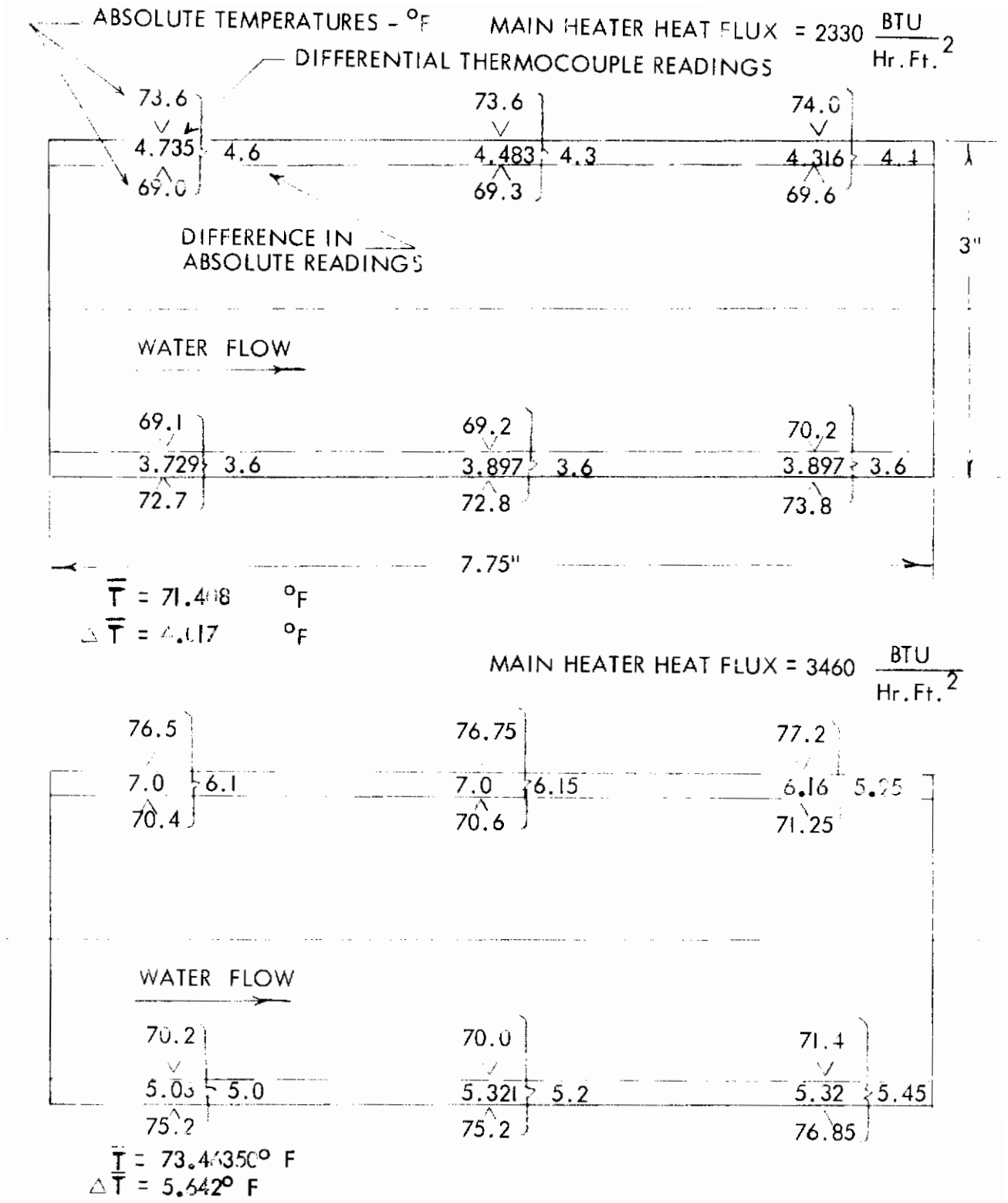

FIGURE 60 THERMOCOUPLE READINGS ON STAINLESS STEEL SPECIMEN

UNCLASSIFIED
Security Classification

DOCUMENT CONTROL DATA - R&D

(Security classification of title, body of abstract and indexing annotation must be entered when the overall report is classified)

1. ORIGINATING ACTIVITY (Corporate author)	2a. REPORT SECURITY CLASSIFICATION
Lockheed-California Company Burbank, California	UNCLASSIFIED
	2b. GROUP NONE

3. REPORT TITLE
AN EXPERIMENTAL AND ANALYTICAL INVESTIGATION OF HYPERSONIC INLET BOUNDARY LAYERS

4. DESCRIPTIVE NOTES (Type of report and inclusive dates)
Final Report, April 3, 1962 - June 21, 1965

5. AUTHOR(S) (Last name, first name, initial)
Stroud, John F. and Miller, Leonard D.

6. REPORT DATE	7a. TOTAL NO. OF PAGES	7b. NO. OF REFS
June, 1965	107	24

8a. CONTRACT OR GRANT NO.	9a. ORIGINATOR'S REPORT NUMBER(S)
b. PROJECT NO. 1366	LR 18803
c Task No. 136605	9b. OTHER REPORT NO(S) (Any other numbers that may be assigned this report) AFFDL-TR-65-123, Vol I
d	

10. AVAILABILITY/LIMITATION NOTICES
(1) Qualified requesters may obtain copies of this report from DDC.

(2) This report has been released to CFSTI.

11. SUPPLEMENTARY NOTES	12. SPONSORING MILITARY ACTIVITY
NONE	Air Force Flight Dynamics Laboratory, Research and Technology Division, Air Force Systems Command, Wright-Patterson AFB, Ohio

13. ABSTRACT

Detailed boundary layer surveys have been made on four axisymmetric compression surface models simulating typical hypersonic inlet compression surfaces at free stream Mach numbers ranging from 4 to 8. The four models were designed to provide isentropic compression at design Mach numbers of 5, 6, 8 and 10. The Mach 8 design model had provisions for wall cooling. Quantitative heat transfer measurements were made on the Mach 8 model at free stream Mach numbers of 5, 6, and 8. The tests were conducted in the Arnold Engineering Development Center (AEDC) 50-inch diameter Mach 8 Tunnel B and 40-inch supersonic Tunnel A, both of the von Karman Facility. Typical free stream Reynolds numbers for these tests were 6.56×10^6 at Mach 4 and 3.8×10^6 at Mach 8, with the Reynolds numbers based on the maximum diameter of the Mach 8 model. The tests of the boundary layer models at various free stream Mach numbers and Reynolds numbers provided a large amount of turbulent boundary layer data on compressive surfaces typical of hypersonic inlets.

Two existing turbulent boundary layer theories were modified to account for the various phenomena found to be of importance in hypersonic boundary layers. Theoretical results from these methods have been correlated with the experimental data.

A significant observation of the present program is the powerful favorable effect of centrifugal force phenomena on boundary layer development in continuous adverse pressure gradients. It was found that these effects become more pronounced with increasing Mach number and reductions in free stream Reynolds number.

DD FORM 1 JAN 64 1473

UNCLASSIFIED
Security Classification

14. KEY WORDS	LINK A		LINK B		LINK C	
	ROLE	WT	ROLE	WT	ROLE	WT
Turbulent Boundary Layer						
Hypersonic Inlet						
Hypersonic Flow						
Adverse Pressure Gradients						
Heat Transfer						

INSTRUCTIONS

1. ORIGINATING ACTIVITY: Enter the name and address of the contractor, subcontractor, grantee, Department of Defense activity or other organization *(corporate author)* issuing the report.

2a. REPORT SECURITY CLASSIFICATION: Enter the overall security classification of the report. Indicate whether "Restricted Data" is included. Marking is to be in accordance with appropriate security regulations.

2b. GROUP: Automatic downgrading is specified in DoD Directive 5200.10 and Armed Forces Industrial Manual. Enter the group number. Also, when applicable, show that optional markings have been used for Group 3 and Group 4 as authorized.

3. REPORT TITLE: Enter the complete report title in all capital letters. Titles in all cases should be unclassified. If a meaningful title cannot be selected without classification, show title classification in all capitals in parenthesis immediately following the title.

4. DESCRIPTIVE NOTES: If appropriate, enter the type of report, e.g., interim, progress, summary, annual, or final. Give the inclusive dates when a specific reporting period is covered.

5. AUTHOR(S): Enter the name(s) of author(s) as shown on or in the report. Enter last name, first name, middle initial. If military, show rank and branch of service. The name of the principal author is an absolute minimum requirement.

6. REPORT DATE: Enter the date of the report as day, month, year, or month, year. If more than one date appears on the report, use date of publication.

7a. TOTAL NUMBER OF PAGES: The total page count should follow normal pagination procedures, i.e., enter the number of pages containing information.

7b. NUMBER OF REFERENCES: Enter the total number of references cited in the report.

8a. CONTRACT OR GRANT NUMBER: If appropriate, enter the applicable number of the contract or grant under which the report was written.

8b, 8c, & 8d. PROJECT NUMBER: Enter the appropriate military department identification, such as project number, subproject number, system numbers, task number, etc.

9a. ORIGINATOR'S REPORT NUMBER(S): Enter the official report number by which the document will be identified and controlled by the originating activity. This number must be unique to this report.

9b. OTHER REPORT NUMBER(S): If the report has been assigned any other report numbers *(either by the originator or by the sponsor)*, also enter this number(s).

10. AVAILABILITY/LIMITATION NOTICES: Enter any limitations on further dissemination of the report, other than those imposed by security classification, using standard statements such as:

(1) "Qualified requesters may obtain copies of this report from DDC."

(2) "Foreign announcement and dissemination of this report by DDC is not authorized."

(3) "U. S. Government agencies may obtain copies of this report directly from DDC. Other qualified DDC users shall request through _____."

(4) "U. S. military agencies may obtain copies of this report directly from DDC. Other qualified users shall request through _____."

(5) "All distribution of this report is controlled. Qualified DDC users shall request through _____."

If the report has been furnished to the Office of Technical Services, Department of Commerce, for sale to the public, indicate this fact and enter the price, if known.

11. SUPPLEMENTARY NOTES: Use for additional explanatory notes.

12. SPONSORING MILITARY ACTIVITY: Enter the name of the departmental project office or laboratory sponsoring *(paying for)* the research and development. Include address.

13. ABSTRACT: Enter an abstract giving a brief and factual summary of the document indicative of the report, even though it may also appear elsewhere in the body of the technical report. If additional space is required, a continuation sheet shall be attached.

It is highly desirable that the abstract of classified reports be unclassified. Each paragraph of the abstract shall end with an indication of the military security classification of the information in the paragraph, represented as *(TS), (S), (C), or (U)*.

There is no limitation on the length of the abstract. However, the suggested length is from 150 to 225 words.

14. KEY WORDS: Key words are technically meaningful terms or short phrases that characterize a report and may be used as index entries for cataloging the report. Key words must be selected so that no security classification is required. Identifiers, such as equipment model designation, trade name, military project code name, geographic location, may be used as key words but will be followed by an indication of technical context. The assignment of links, rules, and weights is optional.